UNIVERSITY OF TURKU

Dimeric diarylmercury-aptamer conjugates for LA-ICP-MS imaging

Master's Thesis

University of Turku

Department of Chemistry

Master's Degree Programme in Chemistry of Drug Development

2024-2026

Md. Maruf Uz Zaman

Master's thesis

Subject: Department of Chemistry, MDP in Exact Science, Chemistry of Drug Development

Author: Md. Maruf Uz Zaman

Title: Dimeric diarylmercury-aptamer conjugates for LA-ICP-MS imaging

Supervisors: Prof. Tuomas Lönnberg

Abstract

Aptamers are synthetic single-chain DNA or RNA oligonucleotides capable of adopting stable 3D conformations and thus binding chosen targets tightly and with great specificity. Owing to the chemical tunability of their nucleic acid backbone, they can be functionalized at selected sites with small compounds, metal ions, or nanomaterial constructs for deployment in molecular imaging, diagnostics and targeted delivery applications. Aptamer based metal tagging is an emerging strategy to translate molecular recognition into spatially resolved elemental signals for mass spectrometric bioimaging. Laser ablation-inductively coupled plasma-mass spectrometry (LA-ICP-MS) is an elemental imaging technique that in a biological context enables quantitative, micrometer scale mapping of endogenous trace elements and exogenously introduced metal tagged biomarker species in two dimensions.

The goal of this study was to synthesize a stable diarylmercurial compound which would be suitable for aptamer conjugation followed by bioimaging. Initially a diarylmercury solid support with DMTr protecting group was synthesized, but it did not survive oxidative and acidic conditions.

Another, azide-linked, dimeric diarylmercury molecule was synthesized to avoid the above mentioned conditions. When separated from the analogous monoarylmercury molecule at room temperature, this compound demonstrated chemical stability. Single-stranded and double-helical oligonucleotides were utilized for conjugation, along with a recently created 76-mer DNA aptamer that is specific to GFAP. The aptamer attaches to the particular protein while bearing the metal tag when the dimeric diarylmercury-aptamer combination is administered to tissue that contains that particular protein. The presence of the protein can then be verified by using LA-ICP-MS to identify and visualize the metal tag.

Keywords: Organomercury, aptamer, diarylmercury compounds, LA-ICP-MS, tissue imaging

List of abbreviations

ACN	Acetonitrile
AAS	Atomic Absorption Spectroscopy
ASO	Antisense oligonucleotide
CPG	Controlled Pore Glass
CV-AAS	Cold Vapour Atomic Absorption Spectrometry
COSY	Correlation Spectroscopy
CT imaging	Computed tomography imaging
DMAP	4-Dimethylaminopyridine
DMF	Dimethylformamide
DNA	Deoxyribonucleic Acid
DCM	Dichloromethane
DMTr	4,4'-Dimethoxytrityl
DBCO	Dibenzocyclooctyne
DTPA	Diethylenetriaminepentaacetic acid
DIPEA	N,N-Diisopropylethylamine
DOTA	1,4,7,10-tetraazacyclododecane-1,4,7,10-tetraacetic acid
DESI-MSI	Desorption electrospray ionization–mass spectrometry imaging
ESI-TOF HRMS	Electrospray Ionization – Time-of-Flight High Resolution Mass Spectrometry
FFPE	Formalin-Fixed Paraffin-Embedded
HSQC	Heteronuclear Single Quantum Correlation
HMBC	Heteronuclear Multiple Bond Correlation
LC-MS	Liquid Chromatography Mass Spectrometry
LA-ICP-MS	Laser Ablation Inductively Coupled Plasma Mass Spectrometry
LCAA-CPG	Long-Chain Alkylamino Controlled Pore Glass
MRI	Magnetic Resonance Imaging
MALDI-MSI	Matrix-Assisted Laser Desorption/Ionization Mass Spectrometry Imaging
NMR	Nuclear Magnetic Resonance
ON	Oligonucleotide
PFA	Paraformaldehyde
PBS	Phosphate buffered saline
PCR	Polymerase Chain Reaction
PET	Positron Emission Tomography

PSMA	prostate-specific membrane antigen
PyBOP	(Benzotriazol-1-yloxy)tris(pyrrolidin-1-yl)phosphonium hexafluorophosphate
RNA	Ribonucleic acid
SELEX	Systematic Evolution of Ligands by Exponential Enrichment
SPECT	Single Photon Emission Computed Tomography
SIMS	Secondary Ion Mass Spectrometry
SPAAC	Strain-promoted alkyne-azide cycloaddition
siRNA	small interfering RNA
TBE	Tris-borate-EDTA buffer
TLC	Thin Layer Chromatography
TEA	Triethylamine
TEAA	triethylammonium acetate
UV	Ultraviolet
VEGF	Vascular Endothelial Growth Factor

Table of Contents

* This is to declare that, AI (free version) was used in this thesis writing to rectify grammatical errors and in generating one image.

1. Introduction

1.1 Aptamers

Aptamers are single-stranded DNA or RNA oligonucleotides typically containing ≤100 nucleotide units. These single-stranded DNAs or RNAs can fold into desired three-dimensional shapes (loops, bulges, G-quadruplexes, double-helical stems) to create a binding pocket. [1, 2] Moreover, aptamer domains can be placed on one strand of a duplex (e.g. as a hairpin or overhang) in more complex designs. [2]

Aptamers are typically isolated in vitro from very large random nucleic acid libraries (of the order of 10^{13}–10^{16} unique sequences) using SELEX (Systematic Evolution of Ligands by Exponential Enrichment), in which target-binding sequences are progressively enriched over successive selection cycles. In each round of SELEX, the library is incubated with the target, bound strands are separated from non-binders, and the selected pool is amplified (by PCR or transcription) to generate the input for the next cycle. Repeating this bind–partition–amplify scheme drives a Darwinian-style enrichment that yields a small set of high-affinity, target-specific aptamer sequences from the initial random pool. [3-6]

Aptamers were first reported by Tuerk and Gold for RNA ligands to bacteriophage T4 DNA polymerase and by Ellington and Szostak for organic dyes [1, 7] Subsequent work has demonstrated that both RNA and DNA aptamers can be selected against a wide variety of targets.

Aptamers can be used for different purposes (e.g. as targeting domains in diagnostics, therapeutics, and imaging probes) as they are nucleic acid ligands and available to conjugate with amines, azides, alkynes, thiols etc. [6, 8-10]

1.1.1 Aptamers as targeting ligands

Aptamers make effective targeting ligands. They are small in size with low immunogenicity and their chemical modification is easier than antibodies for desired conjugation to show high, antibody-like binding specificity. Aptamers can be prepared accordingly to show effective, specific targeting in therapeutic, delivery, and imaging settings in vivo. [11-13]

Specifically for protein targets, aptamers are attractive targeting ligands as they can be modified for affinity and selectivity towards specific protein epitopes. [14, 15] The anti-VEGF aptamer pegaptanib (2′-fluoropyrimidine RNA aptamer) is a key example which recognizes a defined isoform ($VEGF_{165}$) with high affinity and selectively inhibits pathological angiogenesis in patients with neovascular

age-related macular degeneration, demonstrating precise protein isoform targeting in the clinic. [16, 17]

Similarly, the DNA aptamer AS1411 targets the cell-surface form of nucleoli on cancer cells, binds specifically, is internalized, and has progressed to phase II trials, showing that aptamers can recognize and functionally engage protein receptors *in vivo*. [18, 19]

Numerous preclinical studies have further shown that protein-binding aptamers can be conjugated to drugs, siRNA/ASO (small interfering RNA /antisense oligonucleotide) cargo, nanoparticles, or imaging agents, using them as modular recognition domains to deliver attached payloads selectively to cells expressing the cognate protein. [13, 20-24]

1.1.2 Aptamers with metal tags for imaging

There are several studies on metal tagged aptamers which proves the suitability of aptamers to carry metal-containing moieties for several purposes.

In optical and CT (computed tomography) imaging, El-Sayed and coworkers showed the accumulation of PSMA (prostate-specific membrane antigen) -targated aptamer-gold nanoparticle conjugate on PSMA positive cancer cells. They got strong optical reflectance contrast for in vitro imaging. They also proved that an aptamer can localize a metallic core to specific cell-surface markers. [25]

Another relevant CT/fluorescence approach showed the use of aptamer-targeted gold probes in vivo to direct tumor resection. [26] Gadolinium chelate-aptamer conjugates have been used as targeted metal-based contrast agents for MRI. A DNA aptamer (ob5) selected for oligomeric amyloid-β was chemically linked to Gd-DOTA (1,4,7,10-tetraazacyclododecane-1,4,7,10-tetraacetic acid), and the resulting Gd-DOTA–ob5 probe produced stronger, more localized T1-weighted MRI signal in Alzheimer's model mouse brains than non-targeted Gd-DOTA, particularly in regions rich in oligomeric Aβ deposits. This demonstrates that an aptamer can direct a metal-based contrast agent to its protein target in vivo, effectively turning the aptamer–chelate conjugate into a site-specific MRI contrast agent without abolishing target binding. [27]

In mass-based imaging and cytometry, Chen and co-workers used a metal-labeled RNA aptamer probe, obtained by attaching a DTPA (diethylenetriaminepentaacetic acid) to a PSMA-binding aptamer, in imaging mass cytometry of FFPE (formalin-Fixed Paraffin-Embedded) prostate cancer tissue. [28]

Another study on aptamer-based single-cell mass cytometry demonstrated that metal-tagged aptamer panels have the ability to distinguish disease subtypes with high accuracy. [29] A general scheme for metal tagging with aptamers can be demonstrated as scheme 1.

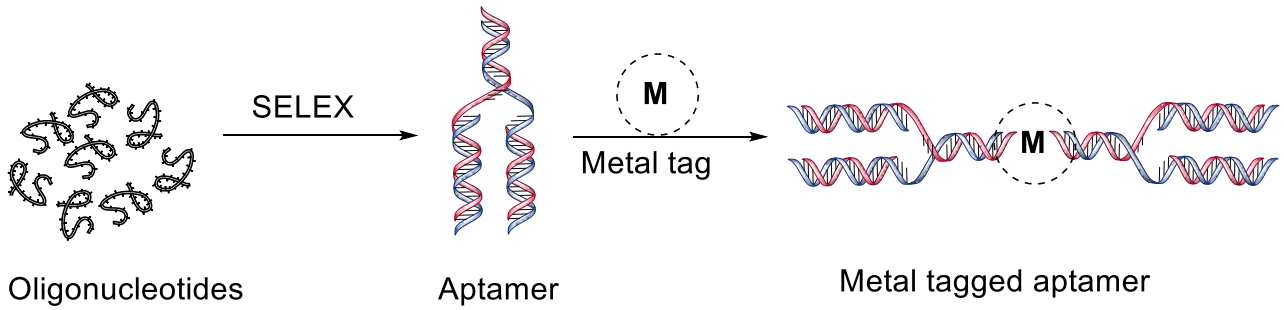

Scheme 1. Aptamer formation and metal tagging.

1.1.3 The advantages of DNA aptamers over RNA aptamers

DNA aptamers are chemically robust and easier to handle in practice than RNA aptamers. These advantages have made DNA aptamers more useful for metal tagging.

DNA aptamers are not as susceptible to nuclease degradation as RNA aptamers. In some cases, the half-life of an RNA aptamer is very short (seconds to minutes) unless heavy modification (2′-F, 2′-OMe, etc.) is carried out. Aptamers have to survive sample preparation, incubation and washing steps before LA-ICP-MS analysis. Moreover, DNA aptamers do not need extensive modification for the purpose of stability for high affinity protein binding. [30, 31]

DNA shows tolerance toward different stages of sample preparation (fixing, washing or storage) for imaging in FFPE or cryosections. On the other hand, RNA is much more sensitive. Using a DNA aptamer as the recognition element therefore reduces the risk that the metal-tagged probe will be partially degraded or structurally compromised by tissue processing before imaging. [32]

DNA aptamer synthesis is easier and more straightforward with site-specific terminal or internal functional groups (amines, thiols, azides, alkynes). Different studies prove that DNA aptamers retain high affinity for protein targets even after covalent attachment of PEG chains or nanomaterials. [6, 20, 33, 34] DNA aptamers can carry a metal chelate and still function as selective imaging ligands in MRI. [35, 36] They are also popular as carriers of radiometals or lanthanides in PET/SPECT and fluorescence imaging probes. [24, 37, 38] These stability (both chemical and biological), cheaper and easier synthesizability make DNA aptamer more favourable than RNA one.

1.2 LA-ICP-MS

Laser ablation–inductively coupled plasma–mass spectrometry (LA-ICP-MS) is a sophisticated method for spatially resolved metal analysis in biological tissues. This method provides quantitative mapping of elemental distribution in cellular length scales. Unlike optical imaging techniques, such as fluorescence, LA-ICP-MS can identify many elements at once based on their mass, avoiding problems like spectrum overlap and photobleaching. This makes LA-ICP-MS more suitable for metal-based drugs, and exogenous metal tags in complex tissues studies. [39, 40]

Previous *in vivo* studies to identify heavy-atom tags have established LA-ICP-MS as a reliable method in bio-imaging. For instance, Karst and co-workers quantified Pt and Ruthenium distribution in different organs of mice treated with cisplatin and the Ru(III) drug candidate KP1339. [41] Becker and colleagues proved once more the spatial distribution and detectability of platinum on mouse kidneys. [42] More recently, methylmercury-derived Hg quantification in rat kidneys using a similar technique was established by Iwase et al. [43-44]

Not only metals and small-molecule drugs, but also metal-conjugated antibodies and nucleic acids can be detected by LA-ICP-MS. Doble and co-workers and Becker reviewed different successful studies about metal-labeled antibodies or nanoparticles immunohistochemistry in tissues using LA-ICP-MS. All these studies motivate the development of synthetic metal tags that couple a biomarker (antibody, peptide, or aptamer) with a metal-containing moiety to be detected by LA-ICP-MS. [40]

1.2.1 Principle

LA-ICP-MS operates by generating small amounts of aerosol portable solid material from given sample using a focused pulsed laser. The material is then carried into a high-temperature plasma region where it is atomized and ionized. The resulting ions are then separated and quantified in a mass spectrometer based on their m/z.

A pulsed UV laser (commonly 193 or 213 nm) generates small particles from the sample surface of the tissue sample that is needed to be analyzed. A carrier gas (commonly He mixed Ar) carries those particles to the inductively coupled plasma region. The ablated particles are desolvated, atomized, and ionized, and the resulting ions are separated by m/z and counted. Each targeted isotope generates a time-resolved signal proportional to the amount of that element ablated at each position.

A two-dimensional image of the chosen isotope is then constructed, encoding the elemental intensity (and, after calibration, concentration) by assigning the spatially resolved ion signals to their corresponding x-y coordinates on the tissue. [39, 45, 46]

1.2.2 Instrumentation

LA-ICP-MS has three primary hardware subsystems, namely a laser ablation unit that defines the spatial resolution, a carrier gas interface to carry the ablated material to the plasma region and an ICP-MS to ionize and detect the targeted element (Figure 1).

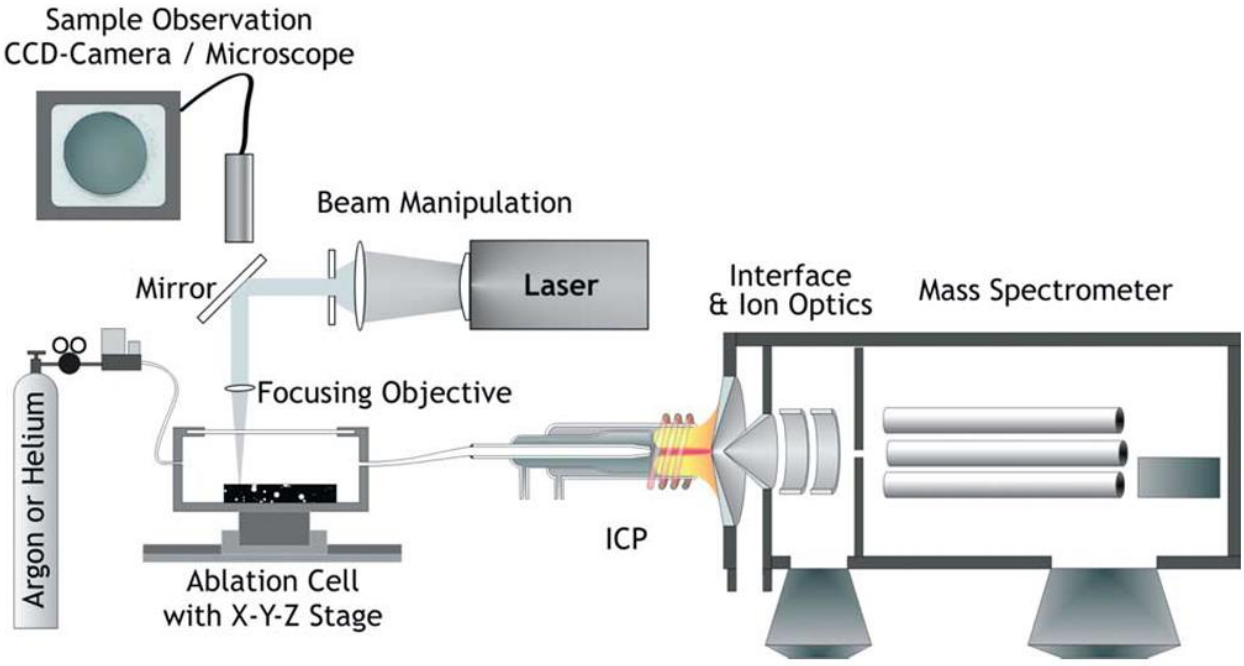

Figure 1. Schematic set-up LA-ICP-MS. [78] (permission was asked to the journal for citation)

1.2.2.1 Laser ablation unit

The laser ablation system focuses on the region of a tissue sample for detection. Conventionally 193 nm and 213 nm UV lasers are used for excimer and solid-state samples, respectively, as these short wavelengths produce fine particles from organic matrices suitable for transportation and ionization. From the defined region of tissue sample surface, each focused laser pulse removes small particles. The achievable lateral resolution is set by the laser spot size (often 5–50 µm) and the step size between ablation lines, while the ablation depth per pulse (from a few hundred nanometers to a few micrometers) determines the z-resolution. [39, 45]

1.2.2.2 Aerosol transport

The ablation cell is flushed with a carrier gas (He with Ar stream), which helps to carry the ablated small particles and vapour through transfer tubing into the ICP-MS interface. Washout times and the signal sharpness are determined by the properties of the cell and transfer lines (volume, geometry, surface properties). To achieve sufficient resolution for preserving spatial fidelity (order of tens of milliseconds) at high scan speeds, low-volume and rapidly flushed cells are necessary.

Modern bioimaging setups often use "two-volume" or rapid-washout cells specifically optimized for thin tissues, minimizing aerosol dispersion between neighbouring pixels and improving quantitative performance. In quantitative Hg imaging, Iwase et al. emphasized the importance of stable aerosol transport when using an agarose-gelatine Hg standard, with optimized gas flows and cell design, they obtained reproducible signals that allowed accurate calibration against CV-AAS (Cold Vapour Atomic Absorption Spectrometry). [39, 44, 45, 48, 49]

1.2.2.3 ICP-MS system

In the inductively coupled plasma region (typically Ar at ~6000–8000 K), aerosol carried particles get atomized, ionized and detected. After that, a mass analyzer (usually a quadrupole or time-of-flight spectrometer) is used to isolate according to m/z and quantify them. Fast dwell times and rapid mass hopping (quadrupole) or full-spectrum acquisition (TOF) are crucial for imaging purposes to record multi-element data at each pixel without decreasing spatial resolution.

Moreno-Gordaliza et al. used a quadrupole ICP-MS to quantify Pt, Cu and Zn simultaneously in 3 µm mouse kidney tissues. [42] Meanwhile, Doble and co-workers used TOF-MS to capture complete mass spectra at each voxel (i.e. each three-dimensional volume element, the 3D analogue of a pixel) in complex biological samples. [50]

1.2.3 Quantification strategies & Analytical performance

LA-ICP-MS imaging has great sensitivity, spatial resolution, linearity, and precision. These qualities obviously depend on both optimum instrumentation and calibration strategy. Quantification in LA-ICP-MS imaging is typically achieved using matrix-matched standards, so that calibration samples and tissues behave similarly during ablation and aerosol transport and the measured signals reliably reflect element concentrations. Homogenized biological material is generally spiked with known concentrations of the analyte and prepared similarly as the original sample. This provides calibration standards relating counts per second to µg g^{-1}.

Different elemental detection studies reported the range of detection as low-µg kg^{-1} (low-ppb) and lateral resolutions of 5–20 µm. For example, Reifschneider et al. successfully detected Pt in 5 µm

polymer-embedded mouse organs with a LoD of 8 µg kg^{-1}. They got good precision and reproducibility across entire organ sections. [41] Iwase et al. also demonstrated accuracy and precision (7.84 ± 0.57 µg g^{-1}) while imaging Hg on MeHg-exposed rat kidneys. [44]

Moreno-Gordaliza et al. validated their LA-ICP-MS concentration maps by comparison with microwave digestion followed by solution ICP-MS to quantify Pt, Cu and Zn in mouse kidney. [42] Reifschneider et al. introduced another strategy consisting of cold-curing polymer (Technovit 7100) blocks spiked with platinum acetylacetonate for mapping Pt in cisplatin-treated organs. [41] Iwase et al. used agarose-gelatine gels as standards for Hg imaging and got similar concentrations as by CV-AAS. [44]

So, either micro-droplet-deposited gelatine films or cell-based standards can be used but they should mimic the sample matrix and exhibit homogeneous, well-known analyte content to get reliable quantitative data. [51, 52]

1.2.4 Applications in biological tissues

LA-ICP-MS imaging is an established method to map endogenous metals, metal-based drugs and different metal tags in biological tissues.

Becker and co-workers used brain tissues of human, rat and mouses to detect different essential and toxic metals. Their experiments produced micrometer-scale images of Fe, Cu and Zn by LA-ICP-MS relating altered metal distributions to models of Parkinson's disease and stroke. [40] Hare and colleagues also stablished a detailed protocol for imaging of Fe, Cu and Zn in mouse brain at 30 µm resolution. [53] Moreno-Gordaliza et al. used 3 µm sagittal rat kidney and showed the Pt accumulation in the cortex and corticomedullary junction to correlate the mapping with nephrotoxic damage. [42] Reifschneider et al. extended this work. They used mouse liver, kidney, spleen and testis to demonstrate the retention and heterogeneous distribution of platinum-based drugs. A follow-up methodological study quantified Pt and Ru from cisplatin and KP1339 in mouse viscera, confirming that LA-ICP-MS can simultaneously track multiple metal-based drugs in complex tissues. [41]

In tumors of mice treated with cisplatin, LA-ICP-MS mapping showed heterogeneous platinum accumulation that correlated with histological features. Successful experiment on Pt and Ru mapping in CT-26 colon carcinoma tumors and surrounding tissue proved LA-ICP-MS as a tool for mechanism-of-action studies. [43] Marolt et al. demonstrated nanoparticle-derived silver tracking across trophic levels and in different organs of fish, earthworms and plants. [54]

1.2.5 Comparison with other imaging techniques

LA-ICP-MS is a microdestructive method used for elemental imaging rather than molecular imaging. Elements are detected based on their *m*/*z* to provide absolute or semi-quantitative concentration maps. On the other hand, MALDI-MSI (Matrix-Assisted Laser Desorption/Ionization Mass Spectrometry Imaging) and DESI-MSI (Desorption electrospray ionization–mass spectrometry imaging) can map intact lipids, metabolites and peptides but typically lack the elemental speciation and absolute quantitation potential of LA-ICP-MS. [55, 46]

Compared with X-ray fluorescence (micro-XRF/XFM), which is non-destructive and well suited for large-area elemental maps but often has higher detection limits for trace metals, LA-ICP-MS generally offers better sensitivity and more robust quantification when matrix-matched standards are used. [56]

Unlike MALDI-MSI and SIMS (Secondary Ion Mass Spectrometry), which excel at delivering rich molecular information (lipids, peptides, small molecules) and, in the case of SIMS/NanoSIMS, nanometer-scale spatial resolution, LA-ICP-MS does not resolve molecular identities but instead provides multiplexed elemental and isotopic data with a wide dynamic range. [57, 58]

MRI and PET further complement these mass spectrometric methods by enabling non-invasive, whole-organism or whole-organ imaging over time, but they do not directly measure elemental distributions and typically rely on contrast agents or radiotracers. [59]

1.3 Diarylmercury compounds

Diarylmercury compounds are a class of organomercury compounds where Hg(II) is covalently linked to two aryl groups. They are neutral species. The central Hg(II) is connected to two sp^2 hybridized carbon atoms of aromatic species in a linear C-Hg-C arrangement. Different studies on mercurated aryl compounds prove the bond length of C-Hg-C indicating it to be a strong metal-carbon bond. A polarized σ bond connects each Ar portion to a relatively heavier metal centre which controls the reactivity of the metal-carbon bond. [60, 61] This is because of the formation of weaker and more polarizable metal-carbon bond by heavy metal.

1.3.1 Synthetic routes for diarylmercury compounds

Diarylmercury compounds can be synthesized following either direct organomercury formation from aryl precursors or transmetalation protocols.

Electrophilic aromatic mercuration is a well-established method to synthesize diarylmercury compounds as reported by Vicente et al. and Kitching et al. [83, 84] They worked on 3,4,5

trimethoxy(N tert butylcarbamoyl)benzene to perform electrophilic aromatic mercuration with mercury(II) acetate in acidic medium. That reaction afforded the corresponding ortho mercurated arylmercury(II) acetate. Regioselective C–H activation at the 6 position of the aromatic ring was facilitated by the amide directing group and the highly electron-donating methoxy groups. After being treated with chloride, the crude arylmercury(II) acetate was converted into the arylmercury(II) chloride species, which was then turned into the symmetrical diarylmercury derivative via halide abstraction/symmetrization (scheme 2).

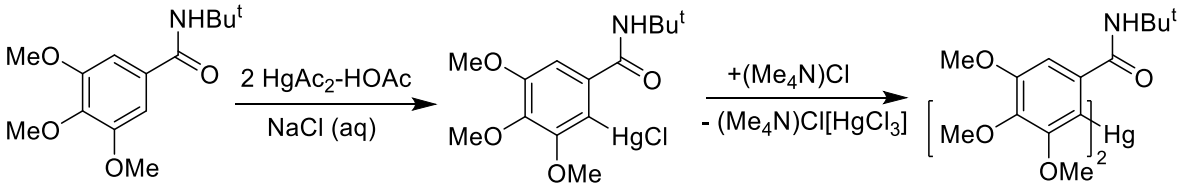

Scheme 2. Electrophilic aromatic mercuration

To stabilize and solubilize HgX_2, diethyl ether, THF or a mixture of ether-hydrocarbon solvents can be used. In practice, purification of desired Ar_2Hg from ArHgX intermediates is tricky.

Another way is transmetalation protocol. This is followed when direct synthesis is challenging or when transition-metal complexes form. Sometimes ArMgX acts as a strong base and is incompatible with sensitive functional groups. For example, in the presence of Cs_2CO_3 in ACN, the following reaction can be carried out (scheme 3).

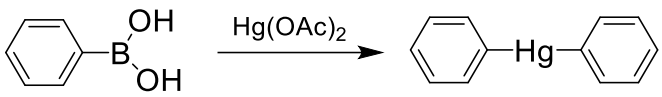

Scheme 3. Synthesis of symmetrical Ar-Hg-Ar compounds from arylboronic acids.

Arylboronic acids have an extended range of substitution patterns. Using the transmetalation method makes Ar_2Hg a versatile aryl-transfer product than what is possible using strongly basic Grignard reagents. [63]

From aryl precursors, where Hg(II) halides react with aryl Grignard reagents (Ar-X), is a well-established path for preparation of symmetrical Ar-Hg-Ar compounds. Two molar equivalents of an Ar-Mg-X reagent react with one equivalent of HgX_2 to form the Ar-Hg-Ar product (scheme 4). [62]

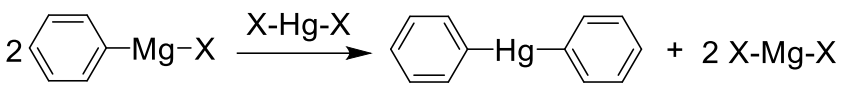

Scheme 4. Synthesis of symmetrical Ar-Hg-Ar compounds from aryl Grignard reagents.

1.3.2 Reactivity and stability of diarylmercury compounds

Organomercury compounds have low polarizable Hg-C bonds. This makes them chemically inert in water under physiological conditions. Acidic environment promotes cleavage by protonation of the carbon atom (scheme 5).

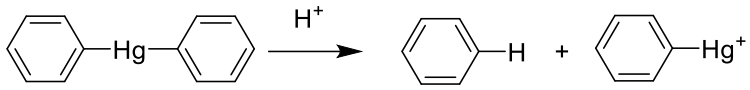

Scheme 5. Protonation of the carbon atom in Ar-Hg-Ar

Organomercury compounds also do not react considerably with dissolved oxygen or hydroxide, iodide or sulphide ions. The thermal and hydrolytical stability makes organomercury compounds useful for further synthetic transformations. [64]

In organic solvents (i.e. heptane, toluene) mercurial compounds do not undergo Hg-C cleavage over two weeks. Whenever Hg coexists in two different oxidation state (Hg^0/Hg^{2+}), cleavage may occur fast. To store these compounds, this coexistence should be avoided. [65]

Diarylmercurials react with $ArSO_2Cl$ in $CHCl_3$ to form arylmercuric arenesulfonates $RHg(O_2SR)$ (scheme 6).

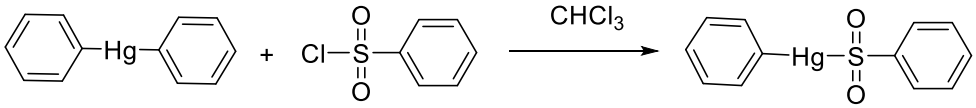

Scheme 6. Synthesis of arylmercuric arenesulfonates from diarylmercury compounds.

Diphenylmercury reacts with equimolar benzenesulfinic acid to form the same product. These reactions were performed in chloroform with an equimolar amount of acid which proves the impact of strongly acidic and nucleophilic environment to cleave the Hg-C bond. In these reactions, the sulfonyl species (e.g. benzenesulfinate derived from $ArSO_2Cl$ or benzenesulfinic acid) acts as the nucleophile. [64] At neutral pH (6-9), nucleophiles like hydroxide or sulphide cannot attack the C-Hg bond as it lacks an electrophilic site.

Whenever the C-Hg-C bond is cleaved, thiolates or sulfonates may react with the exposed Hg(II). Diarylmercury compounds have strong binding and steric shielding to slow down nucleophilic attack at neutral pH. Organomercury compounds can also survive ON conjugation at neutral pH.

Sunlight can break down organomercury compounds. Phenylmercury decomposes faster (quantum yield ~0.24) than dimethylmercury and methylmercury as the latter absorb light only weakly. But such decomposition does not take place instantly. In case of long-term storage, organomercury compounds should be protected from UV light.

1.3.3 Electronic effects on the stability of diarylmercury compounds

Electron-donating substituents on the arene rings stabilize the Hg-C bond and reduce its susceptibility to cleavage. Electron-withdrawing substituents, in turn, make the mercury centre more electron-poor and thus more susceptible to coordination and bond activation by external donors. The higher coordination number of Hg(II) makes the Hg-C bond more labile. The lability of the Hg-C bond is determined by various parameters, including the inherent Hg-C bond strength, the existence of adjacent donor ligands that can enhance the coordination number at Hg, and the stability of the demercurated aryl product. [60, 61]

Ligand environment plays an important role on Hg-C bond lability. This effect was demonstrated with two different compounds - PhSeHgMe and PhSeHgEt (Figure 2). They both feature linear coordination at Hg. But in solid state, an additional Hg…Se interaction is observed which allows Hg to reach a higher coordination number. [61] In aqueous PhSeHgEt, coordination by selenium and an increased coordination number at Hg promote protolytic cleavage of the Hg-C bond, leading to rapid ethane release. So, whenever diarylmercury compounds contain highly polarizable aryl groups (i.e. anisyl, aryloxy, larger fused aromatics etc.), their Hg-C bonds are more activated resulting in cleavage under acidic conditions. [61] So, the stability of diarylmercury compounds depends not only on coordination number of Hg, but also on electron-donating or withdrawing surrounding ligands. [68, 69]

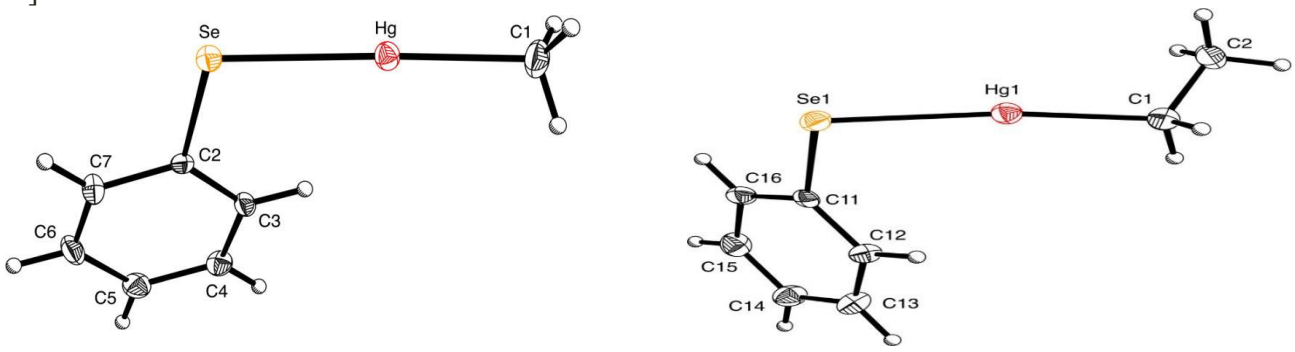

Figure 2. Crystal structures of PhSeHgMe and PhSeHgEt. [61]

Organomercury compounds undergo demercuration under oxidative or halogenating conditions, in which the Hg-C bond is cleaved and the aryl group is converted into more stable derivatives such as aryl halides (Ar-X), while mercury is eliminated from the organic structure.

1.3.4 Steric effects on the stability of diarylmercury compounds

Steric hindrance plays a crucial role to stabilize diarylmercury compounds. This effect can limit the unwanted access of external ligands or electrophiles to the Hg centre. A crowded or geometrically constrained environment around Hg suppresses the formation of higher-coordinate intermediates, which may lead to Hg–C bond cleavage.

Systematic studies on diarylmercury compounds are limited. Previous studies have demonstrated the presence of secondary Hg···E (E = S, Se) interactions in PhSeHgMe and PhSeHgEt compounds whenever there remains sufficient space for external attacks. [61]

On the other hand, steric tension can cause strain into the C–Hg–C bond. Overcrowded organomercury complexes face steric repulsion between ortho-substituents on the aryl rings and other ligands resulting in the distortion of linearity of the Hg-C bond. Potentially this non-linearity causes increasing s-character of the Hg–C bonding orbitals or forces the aryl rings into non-ideal conformations. Although there are few works available, related works on heavy main-group organometallics indicate that such distortion can lower the barrier to bond cleavage by destabilizing the ground state relative to the transition state. For instance, studies on organomercurials show that when bulky, strongly electron-donating imidazole- or selenium-based ligands bind to Hg, they raise the coordination number and introduce steric strain, which together can make the Hg–C bond cleave unusually fast. [60, 70, 71]

These studies suggest a delicate balance between steric protection and steric activation of the Hg–C bond. Moderate steric bulk around Hg that blocks external ligands generally stabilizes diarylmercury compounds, whereas very congested environments that distort linear geometry or introduce strong nonbonded repulsions can actually make Hg–C cleavage easier.

1.3.5 Suitability of diarylmercury compounds for LA-ICP-MS imaging

Mercury has unique atomic properties that produce intense, reproducible LA-ICP-MS signals at low µg g^{-1} levels in tissue, giving a wide dynamic range for imaging. A previous study on MeHg-exposed rat kidneys demonstrated almost identical Hg concentration when measured by either LA-ICP-MS (7.84 ± 0.57 µg g^{-1}) or cold-vapor AAS (7.27 ± 0.46 µg g^{-1}). [77] So, with appropriate matrix-matched standards, LA-ICP-MS can quantify Hg in situ with high accuracy, so that each Hg atom incorporated into a label contributes a reliably countable signal. In a diarylmercury compound, each Ar-Hg-Ar centre contributes one Hg atom with a high ionization efficiency in the plasma and multiple isotopes (e.g. m/z 200 and 202) available for confirmation or multi-channel detection. LA-ICP-MS studies of MeHg-exposed rat kidneys and cisplatin-treated kidneys show that metals like Hg and Pt stay in place

and remain quantifiable through typical tissue processing steps such as sectioning, fixation, and laser ablation mapping. In those experiments, metal concentrations measured by LA-ICP-MS closely matched bulk measurements by techniques like CV-AAS, indicating that the workflows do not cause major loss or redistribution of the metal labels. [76, 77]

1.3.6 Compatibility with bioconjugation

Kotammagari and co-workers demonstrated that a 5-mercuricytosine-containing oligonucleotide could be further functionalized by SPAAC (Strain-promoted alkyne-azide cycloaddition) - the 5′-azido organomercury oligonucleotide was cleanly coupled to a fluorescein-DBCO (dibenzocyclooctyne) tag in aqueous buffer, showing that the Hg-bearing nucleobase can coexist with clickable handles and that the periphery of the molecule can be modified without disturbing the Hg centre. [73, 74] By choosing appropriate aryl precursors, dimeric diarylmercury scaffolds can be designed with identical or distinct linker arms so that attachment points, spacer length and solubility, and orthogonal click handles are all tuned at the aryl periphery without altering the Hg core. [79]

Previous work on organomercury oligonucleotide-polydopamine assemblies shows that a 5-mercuricytosine residue tolerates mercuration in water. [80] Mercurated 6-phenylcarbazole oligonucleotides with 2- or 4-thiothymine complements exhibit high duplex melting temperatures, indicating that the carbazole-Hg-C link remains intact throughout aqueous duplex formation. Taken together, these observations support the view that a diarylmercury center embedded in an aromatic backbone and flanked by linkers can act as a chemically inert heavy-atom node under typical conjugation and imaging conditions.

1.4 Research objectives

Biomolecular targets' distribution within tissues is crucial to know to identify mechanisms of diseases and potential therapies. LA-ICP-MS enables quantitative mapping of metals and metal-tagged biomarkers in tissues. Biomarkers such as aptamers provide highly specific recognition of defined protein epitopes and cell-surface receptors. Combination of these two ideas motivated this study to translate molecular recognition by a metal-tagged aptamer into a robust and quantitative elemental readout in biological tissues.

As previously mentioned, a number of studies demonstrate that aptamers can be attached to a metal-bearing moiety for imaging applications. Concurrently, LA-ICP-MS has proven to be a reliable method for measuring metals including Pt, Ru, and Hg in tissue. [41-44] Despite these developments, there is still no proof of a small molecule metal tag that is chemically well defined and can be linked to DNA aptamers for bio-imaging. The majority of metal-tagged aptamers now in use rely on

polydentate chelators or nanoparticles, which can be polydisperse, sterically bulky, and less suitable for accurate stoichiometric measurements at high spatial resolution.

For Hg-based tags, the LA-ICP-MS system offers high sensitivity and selectivity, allowing the dimeric diarylmercury-aptamer signal to be read out against background with the same instrumentation used to image MeHg and cisplatin in tissue. [46]

Because the core is built in organic solvent and the final coupling to oligonucleotides uses mild, metal-free click reactions at close-to-neutral pH, the conjugation steps do not stress or break the Hg–C bonds. [75] On the other hand, the flexibility and small size of aptamers for targeting different elements have not yet been utilized in LA-ICP-MS investigations of metal-tagged aptamer based medications and metal-labeled antibodies. The creation of a novel class of heavy atom aptamer tags designed especially for LA-ICP-MS was motivated by this gap.

This thesis reports on the synthesis of a dimeric diarylmercury compound through electrophilic aromatic mercuration. This dimeric diarylmercury compound has an Hg-based core that is stable under neutral aqueous conditions, suitable for bio-conjugation and easily detected by LA-ICP-MS. The targeting element is a 76-mer DNA aptamer that has a high affinity for GFAP (Glial Fibrillary Acidic Protein). In order to combine a mercury atom with two targeting ligands and possibly increase affinity through avidity while providing a stoichiometric heavy atom node for quantitative imaging, one mercury unit joins two aryl rings, each of which has a linker to a DNA aptamer. If the Hg core remains intact during tissue sample preparation (conjugate treatment, washing, fixing and incubation), LA-ICP-MS would be able to locate Hg distribution as a direct proxy for aptamer localization. A single binding event brings a single Hg atom to the target, but the same idea could later be implemented as scaffolds with more Hg centers for stronger signal.

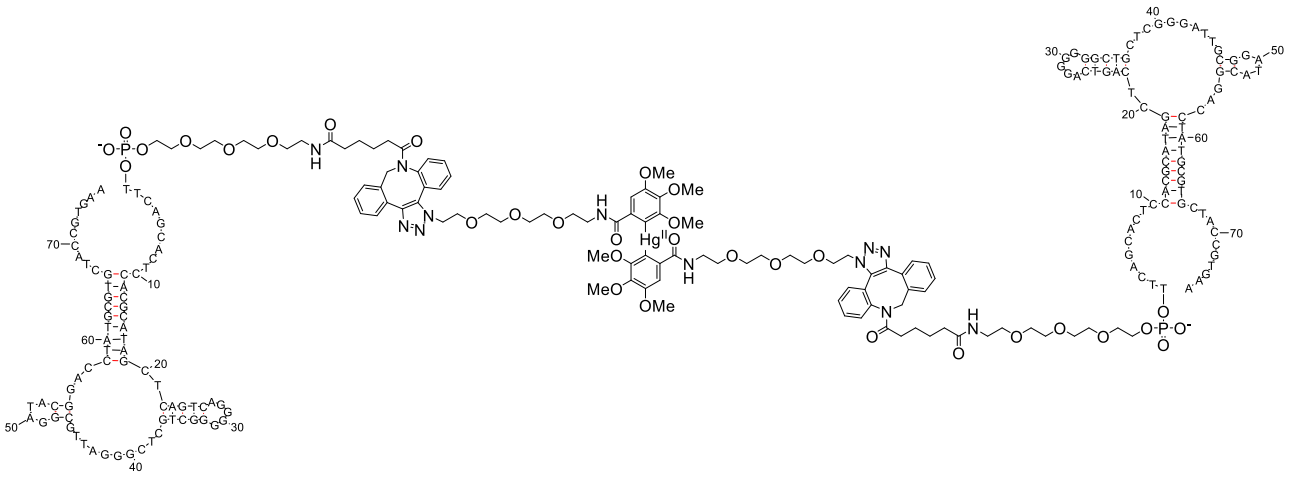

Figure 3. Dimeric diarylmercury-aptamer conjugate.

The main objective of this study was to synthesize a dimeric diarylmercury-aptamer conjugate (Figure 3) and assess its potential as a chemically defined metal tag for LA-ICP-MS imaging in biological tissues (Figure 4). Following goals are targeted to attain in this study-

1. To synthesize and characterize a dimeric diarylmercury scaffold that is stable under neutral aqueous conditions.

2. To synthesize and characterize a 76-mer GFAP-binding DNA aptamer bearing a cyclooctyne group for conjugation.

3. To conjugate the dimeric diarylmercury core to different oligonucleotides and verify the chemical integrity of the resulting bivalent conjugates.

4. To assess the LA-ICP-MS response and targeting performance of the dimeric diarylmercury-aptamer conjugate in suitable tissue sections.

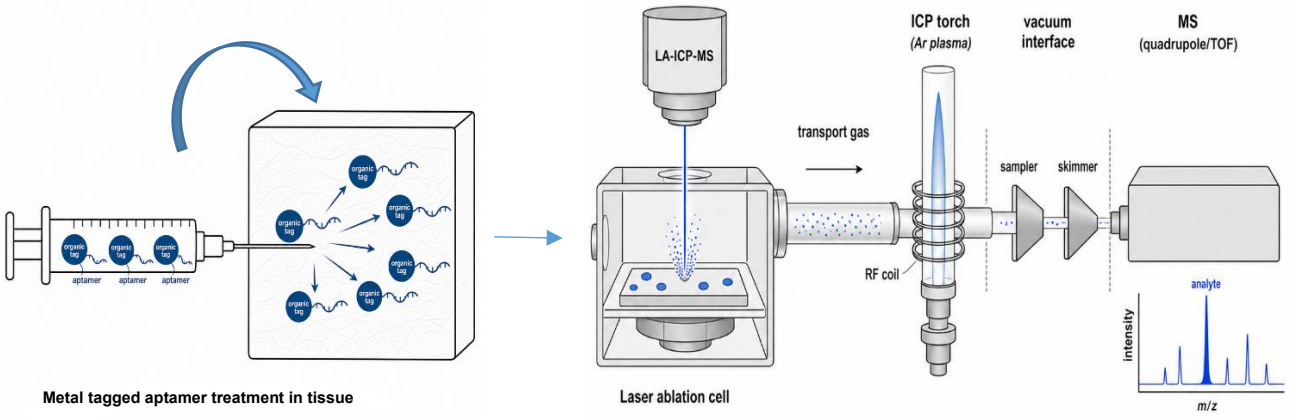

Figure 4. A general overview on bio-imaging of metal tagged aptamer conjugate by LA-ICP-MS (AI generated).

2. Result and Discussion

2.1 Preparation of the diarylmercury solid support

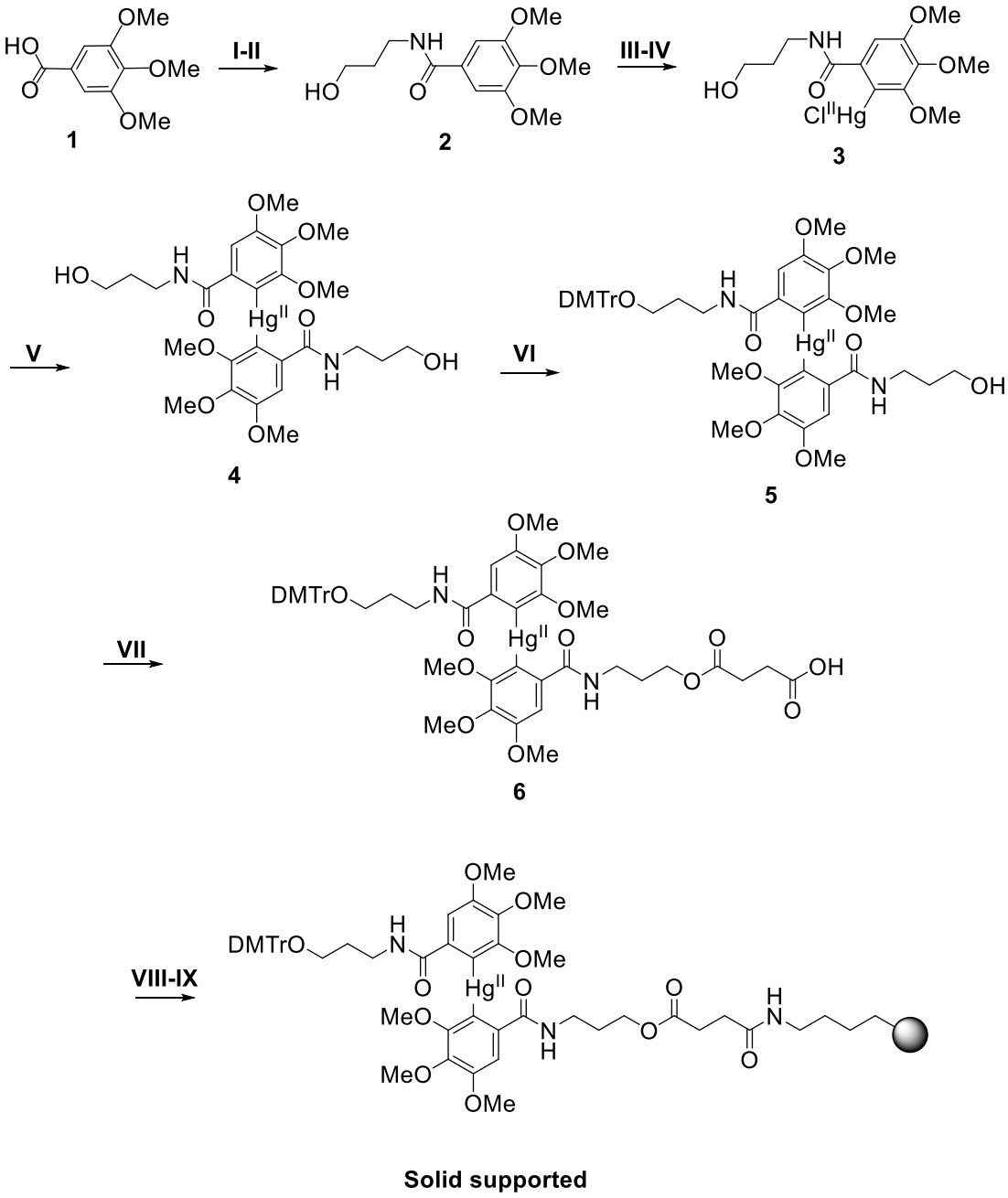

Scheme 7. Synthesis of a diarylmercury solid support. Reagents and conditions: **I**. thionyl chloride, reflux, 3 h, **II**. 3-amino-1-propanol, DCM, DMAP, 80 ˚C, overnight, **III**. mercury(II)acetate, acetic acid, ethanol, reflux, 5 h, **IV.** potassium chloride, water, **V**. tetramethylammonium chloride, acetone, rt, 3 d, **VI.** 4,4´-dimethoxytrityl chloride, triethylamine, DCM, rt, overnight, **VII**. triethylamine, succinic anhydride, DCM, DMAP, rt, overnight, **VIII**. PyBOP, DIPEA, LCAA-CPG, *N*,*N*-

dimethylformamide, rt, overnight, **IX.** Capping A (acetonitrile:*N*-methylimidazole, 80:20, v/v), B1 (40% acetic anhydride in acetonitrile), B2 (60% 2,6-lutidine in acetonitrile), rt, overnight.

First, diarylmercury compound **6** was synthesized and immobilized on a solid support (Scheme 7). Unfortunately the solid supported compound did not function as intended. To investigate the reason behind this failure, acidic and oxidative stability tests mimicking the conditions of the dimethoxytrityl removal and phosphite triester oxidation steps of the oligonucleotide synthesis were conducted on compound **4**.

Diarylmercurials are generally susceptible to acidic and oxidative reaction environments. Compound **4** did not survive the oxidative test where I_2 acted as an oxidant. Equivalent molar I_2 reacted with compound **4** within very short time (2 min), most likely through ligand exchange on Hg(II) to form HgI_2 and an aryl iodide. A general overview of these type of reactions can be shown as scheme 8.

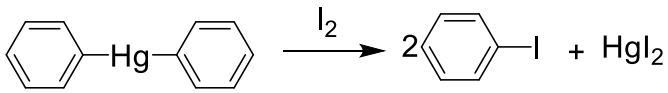

Scheme 8. Ligand exchange of Hg(II) to form HgI_2

In a separate experiment, dichloroacetic acid made the reaction environment acidic. This caused protolytic Hg-C bond cleavage of compound **4**. These acidic and oxidative tests clarified the reasons behind the failure of the oligonucleotide synthesis on the diarylmercury solid support and, unfortunately, ruled out this strategy for preparation of the aptamer conjugate.

2.2 Synthesis of the azide-functionalized diarylmercury compound

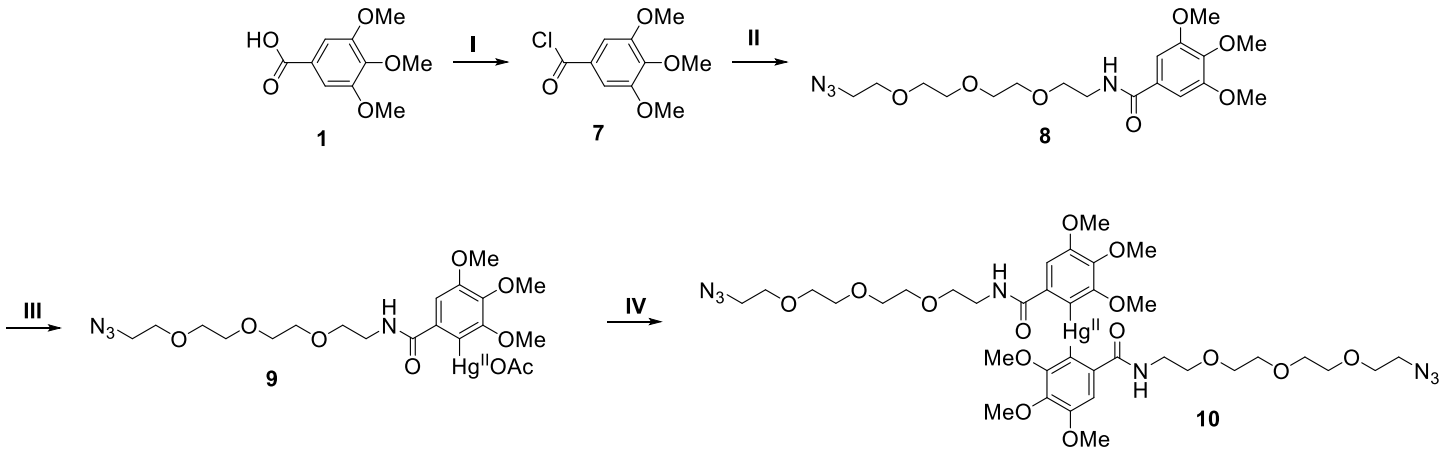

Scheme 9. Synthesis of dimeric diarylmercury compound. Reagents and conditions: **I**. thionyl chloride, reflux, 3 h, **II**. 11-Azido-3,6,9-trioxaundecan-1-amine, DMF, DMAP, Et_3N, rt, 5 d, **III**. $(CH_3COO)_2Hg$, MeOD, 55 ˚C, overnight, **IV**. $(Me_4N)Cl$, MeOD, rt, overnight.

To overcome previous failure (scheme 7), the strategy was changed so that was performed where an amino-PEG3-azide linker was attached to the benzoic acid starting material prior to mercuration (Scheme 9). The azide end remained free to undergo a strain-promoted click reaction with a DBCO group to attach the desired aptamer after oligonucleotide synthesis. Moreover, scheme 9 worked because- when the diarylmercury compound is conjugated to a pre-synthesized oligonucleotide, it does not have to withstand the oligonucleotide synthesis conditions.

Thionyl chloride and 3,4,5-trimethoxybenzoic acid were refluxed to get the crude benzoyl chloride **7**. The crude product was co-evaporated from toluene to get rid of residual $SOCl_2$. Of the resulting 3,4,5-trimethoxybenzoyl chloride **7**, one third was used to synthesize compound **8**.

Peptide coupling of 11-azido-3,6,9-trioxanundecan-1-amine with benzoyl chloride **7** was carried out in DMF with DMAP as a nucleophilic catalyst and TEA as a base. After overnight reaction, NMR data showed 50% completion at that stage. Plausible explanation could be that the reaction had already reached equilibrium in 24 h. After 2 more days, the reaction did not progress at all. Then similar amounts of benzoyl chloride and TEA were added and stirring was continued for one more day. Desired product was observed by NMR and MS. Then the reaction mixture was analyzed by TLC which showed 5 distinct spots. Each spot was analyzed by LCMS. The top one corresponded to benzoic acid. Then came a bis-benzoylated side product and even lower the desired product **8**. Multiple rounds of purification by silica gel chromatography were performed to isolate the desired product **8** from the impurities.

Compound **8** and mercuric acetate were dissolved at 1:2 molar ratio in MeOD to allow monitoring of the reaction by NMR. The comparison between the initial state and after overnight incubation showed substantial conversion to desired product. However, LCMS revealed the presence of both the expected monomer **9** and the dimer **10**. As the monomer seemed more difficult to purify than the dimer, the reaction was pushed towards dimerization by adding 10 equivalents of $(Me_4N)Cl$. NMR showed almost 50 % completion of dimerization after 2 h. After keeping the reaction mixture overnight at rt, additional 5 equivalents of $(Me_4N)Cl$ was added. After another 24 h, the reaction was completed. After purification by RP-HPLC, monomer **9** and dimer **10** were obtained.

2.3 Synthesis of the DNA aptamer

In this study, different DNA oligonucleotides (Table 1) were used to conjugate with the diarylmercury compound **10**. Among them, the 76-mer DNA aptamer **ON1** was synthesised during the project and the others (**ON2** and **ON3**) were either synthesised previously or obtained from commercial sources.

During the 1st attempt of 76-mer oligonucleotide synthesis, 500 Å CPG solid support was used. A DBCO-TEG phosphoramidite was incorporated at the 5′-terminus to enable conjugation with the diarylmercury compound **10** via strain-promoted azide-alkyne cycloaddition (SPAAC). After chain assembly, the support-bound oligonucleotide was treated with concentrated aqueous NH_3 at high temperature (55 ˚C) to cleave the solid support from the **ON** and deprotect the base and phosphate moieties. During UPLC-HRMS analysis of the crude product, different truncated ONs were observed, probably due to the insufficient pore size of the CPG.

In contrast, repeating the synthesis on a 1000 Å CPG solid support afforded a good yield of the desired product **ON1** (Figure 5), which was isolated by RP-HPLC.

Table 1. Different DNA oligonucleotides with their sequence.

ON1	TTC AGC ACT CCA CGC ATA GCT CAG TCA GGG GGG CTG CTC GGG ATT GCG GAT ACG GAC CTA TGC GTG CTA CCG TGA A
ON2	BCN-CGA GCA CTG GC
ON3	GCC AGT GCT CG

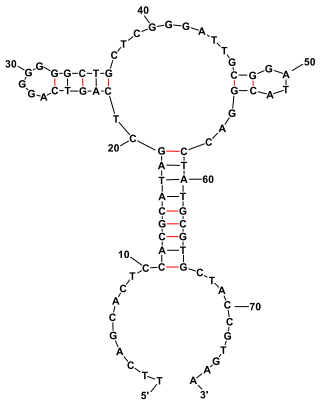

Figure 5. Predicted secondary structure of the 76-mer DNA aptamer.

2.4 Diarylmercury conjugation with different oligonucleotides

Conjugation with the diarylmercury compound **10** was tested with three different DNA oligonucleotides (single-stranded, double-stranded and the 76-mer aptamer) and different chemical conditions (uncontrolled and neutral pH). Each time, the reaction mixtures were incubated at rt and monitored by UPLC-HRMS.

Initially, 0.5, 1.0 and 3.0 molar equivalents of single stranded **ON2** were reacted with the diarylmercury compound **10** to find out favourable conditions with minimum degradation. The

reaction mixture containing 0.5 equivalents of **ON2** gave a predominant signal for the intact dimeric diarylmercury-**ON2** conjugate (Figure 6). A few minor peaks indicating side products, for instance, ketone (from acid-catalyzed alkyne hydrolysis) and demercurated conjugates (with and without Hg) were also seen.

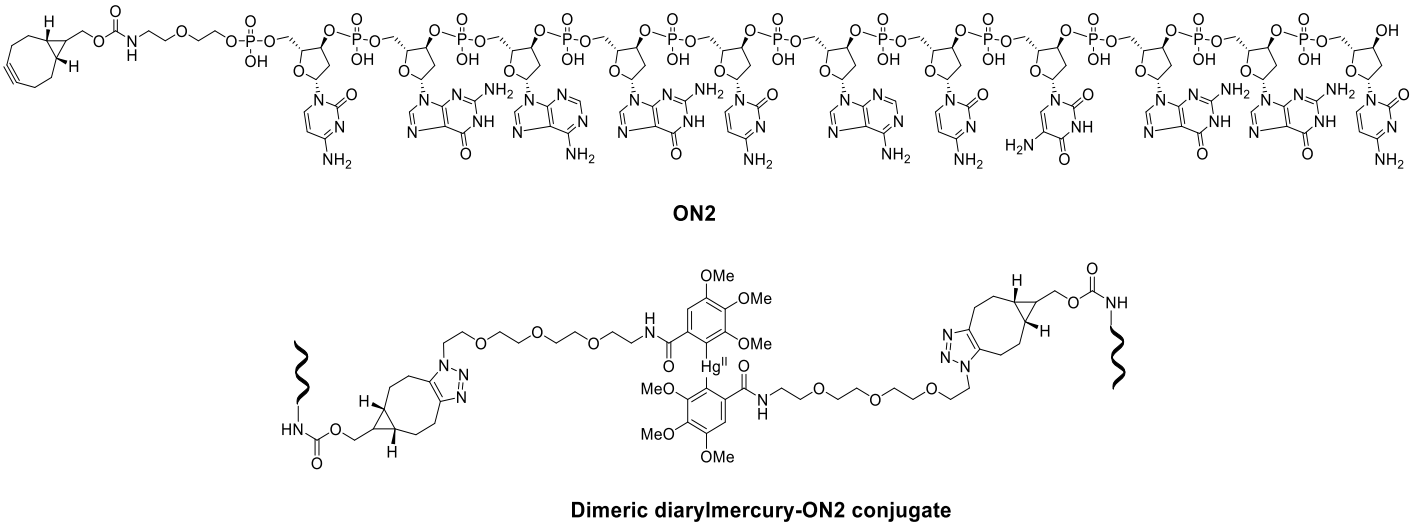

Figure 6. ON2 and Dimeric diarylmercury-**ON2** conjugation

Over time, the peaks of these side products increased significantly as the desired conjugate degraded. The products from the reaction mixtures containing 1.0 and 3.0 equivalents of **ON2** tended to degrade more rapidly. These results indicate the 0.5 equivalent reaction mixture as an optimum for further studies on a double-helical oligonucleotide **ON2•ON3** and the 76-mer aptamer **ON1**.

The above reaction mixture tended to be slightly acidic (approximately 6.7-7.0) due to the residual acidic acid from the elution buffer (after lyophilisation) which might cause ketone formation. Therefore, mixtures of **ON2** (0.5 and 3.0 equivalents) and the diarylmercury compound **10** were prepared again and neutralized by addition of aqueous TEAA (triethylammonium acetate). UPLC-HRMS after 3 h showed an intense signal for the expected conjugate. Though a weak signal for the ketone product and another one nearly 400 mass units lower than the expected conjugate were detected, this result was promising.

Compound **10** also successfully formed conjugates under the above reaction conditions with the double helix **ON2•ON3** and the 76-mer aptamer **ON1**.

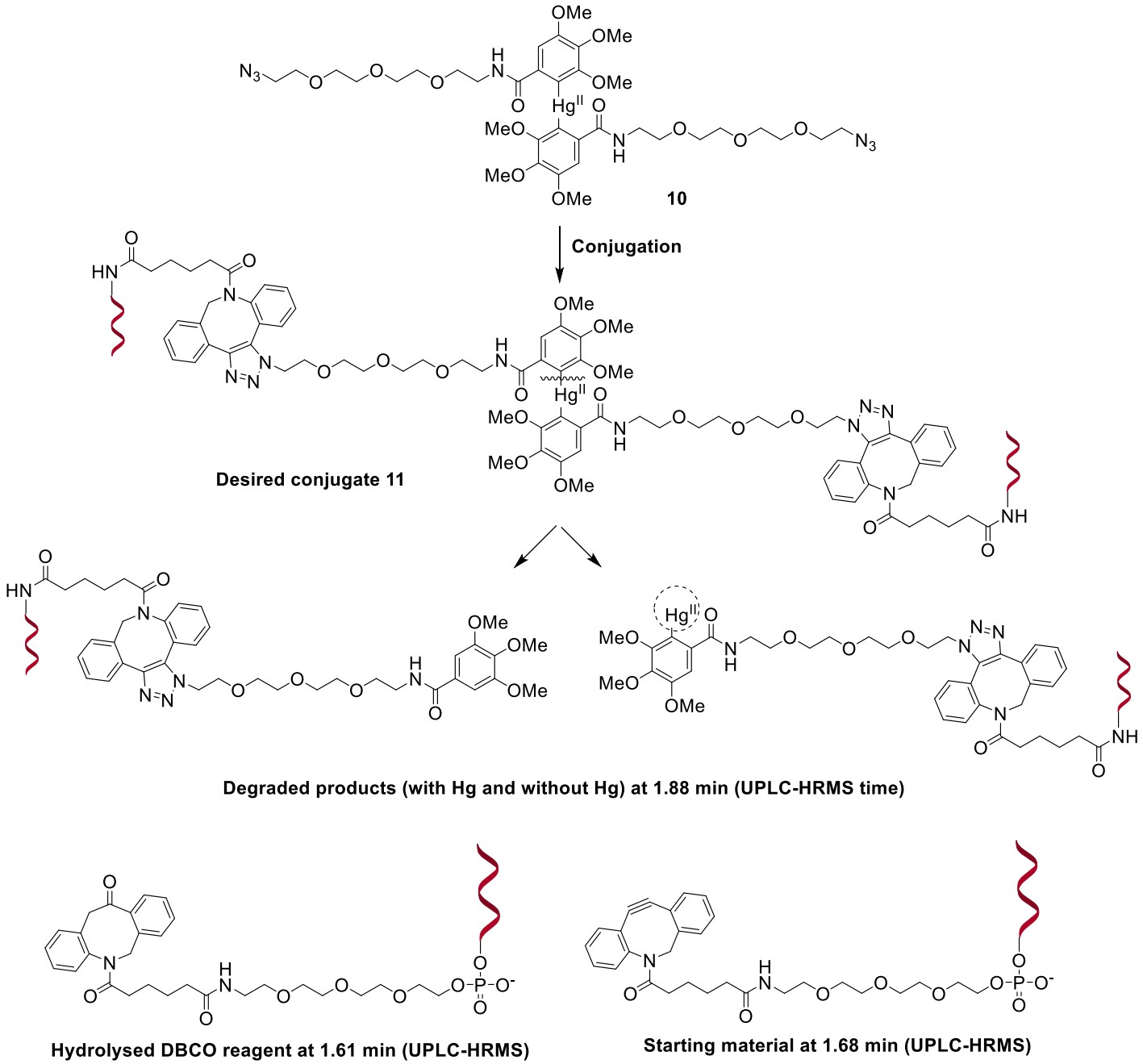

Scheme 10. Dimeric diarylmercury-**ON1** conjugation and its degradation.

The dimeric diarylmercury-**ON1** conjugate **11** (at 2.69 min in UPLC-HRMS) also degraded (Scheme 10) but not as fast as the single-stranded conjugate. Hydrolysed and unreacted starting martial **ON1** eluted at 1.61 and 1.68 min, respectively, in UPLC-HRMS. After that, two different degraded products (with and without Hg) eluted at 1.88 min. The demercuration can take place at either of the Hg-C bonds, resulting in equimolar amounts of mercurated and unmercurated conjugates. When compound **10** is conjugated with single-stranded **ON2** (figure 6), more heteroatoms of nucleobases

(especially G and T) are available for coordination to Hg(II), leading to higher-coordinate intermediates and, eventually, Hg-C bond cleavage. [81, 82]

In the case of the double helix **ON2•ON3**, the heteroatoms most likely to coordinate Hg(II) are engaged in base pairing.

2.5 Kinetic studies on the decomposition of the dimeric diarylmercury-oligonucleotide conjugates

The kinetic stability of the dimeric diarylmercury-**ON** conjugates was determined based on their time-dependent decomposition (Figure 7). Conjugates were incubated at rt and pH = 7.0 and samples were analyzed at appropriate time intervals by UPLC-HRMS.

The conjugate containing single-stranded **ON2** degraded rapidly, with a half-life of 33 h. On the other hand, the conjugate with the double helix **ON2•ON3** was remarkably stable, with a half-life of 3 w. Interestingly, 76-mer DNA aptamer **ON1** containing conjugate **11** showed stability with a a half-life of 1 w. In other words, the decomposition (Scheme 10) was slower than with the single-stranded conjugate **ON2** but faster than with the double helix **ON2•ON3** conjugate. This kinetic stability is sufficient to make it usable as a metal tagged nucleic acid recognition for further tissue imaging experiments by LA-ICP-MS.

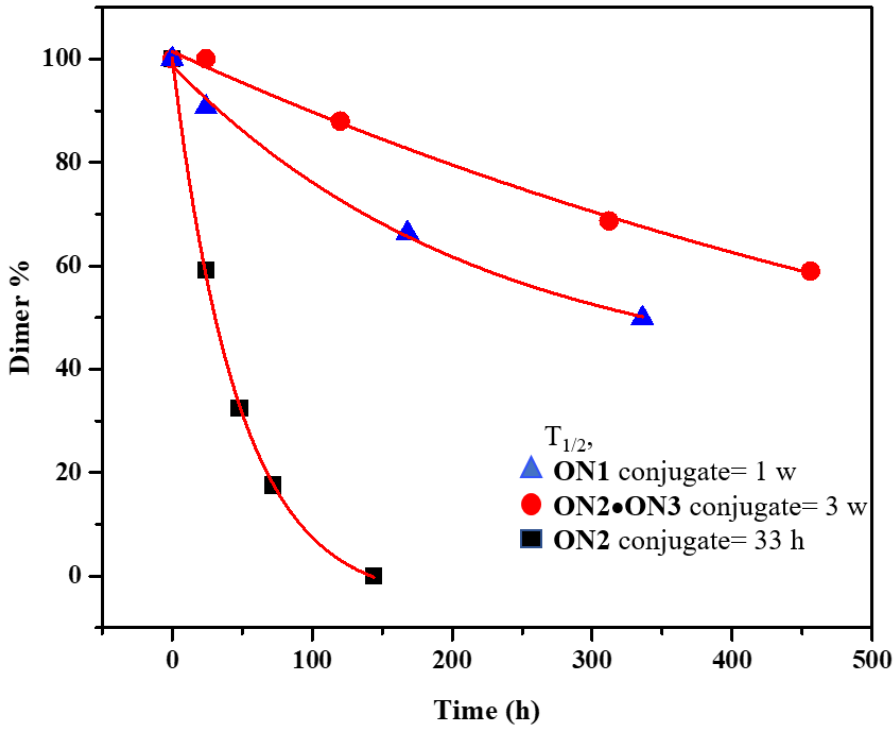

Figure 7. Time profiles for decomposition of the oligonucleotide conjugates at rt (pH = 7.0).

2.6 UV melting profile of **ON1**

To ensure the correct tertiary structure and thermal stability of the aptamer **ON1**, its UV melting profile was determined (Figure 8).

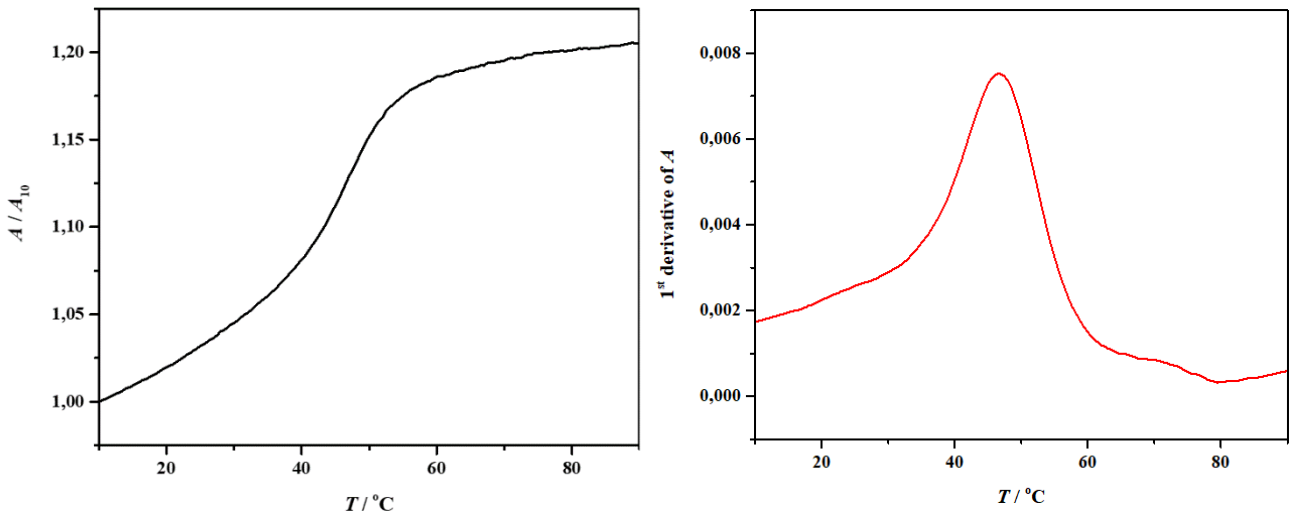

Figure 8. UV melting profile of **ON1.** The average of three cycles (heating and cooling) and first derivative of the absorbance as a function of temperature is indicated by black and red line, respectively. The single melting temperature was approximately 46.5 °C.

UV melting profile (Figure 8) showed a single, sigmoidal transition with a distinct first derivative maximum, suggesting a cooperative, two-state unfolding mechanism. The melting temperature determined from the derivative curve was nearly 46.5 °C, which indicated the stability of the folded structure at rt but gradual unfolding at higher temperatures. For the kinetic and binding measurements carried out at 25-37 °C, **ON1** is anticipated to maintain its native conformation.

2.7 LA-ICP-MS imaging

Two different strategies were tried for sample preparation to detect Hg from the dimeric diarylmercury-**ON1** conjugate by LA-ICP-MS imaging. In the *in vivo* technique, the conjugate was injected into the spinal cord of a live mouse, and the brain tissue was collected. In the other technique, an untreated mouse brain slice was incubated with the conjugate (20 nM) following standard protocol.

Unfortunately, no Hg signal above background was observed from either sample. Possible reasons could be:

1. Insufficient concentration of the conjugate
2. Limited penetration of the conjugate into the tissue

3. Instrument malfunction

During the sample preparation, after treating with dimeric diarylmercury-aptamer conjugate, the tissue slices were incubated a short period (30 min at 4˚ C). This short incubation time might cause limited penetration of the conjugate in tissues. So, longer fixing and incubation time with different conjugate concentration might be explored in the next set of experiment when the instrument is back online.

3. Experimental section

Organomercury compounds can cause serious systemic toxicity. They are lipophilic and some can cross the blood–brain barrier. Human and animal studies of organomercurials show neurological damages.

Confirmation of the structures of the products was obtained by ^{1}H and ^{13}C NMR spectroscopy (Bruker Biospin 500 and 600 MHz) in $CDCl_3$ or DMSO-d_6. Analytical thin-layer chromatography was performed to check purity of all compounds on commercial aluminium plates with a 0.25 mm thickness silica gel layer. Silica gel column chromatography was carried out using silica gel (0.25 mm). Synthesized products were identified by mass spectrometry (Waters RDa Accurate Mass). Capping solution A refers to a mixture of acetonitrile and *N*-methylimidazole (80:20, v/v), capping solution B1 to a mixture of acetonitrile and acetic anhydride (60:40, v/v) and capping solution B2 to a mixture of acetonitrile and 2,6-lutidine (40:60, v/v). When applicable, reagent grade organic solvents were dried over activated 3 Å molecular sieves.

3.1 Preparation of the diarylmercury solid support

3.1.1 *N*-(3-hydroxypropyl)-3,4,5-trimethoxybenzamide (**2**)

3,4,5-trimethoxybenzoic acid (13.506 mmol, 2.8661 g) and thionyl chloride (90 ml) were refluxed for 3 h, after which the thionyl chloride was evaporated. The residue was coevaporated twice from toluene (50 ml) to ensure the removal of any remaining thionyl chloride. The crude benzoyl chloride was dissolved in dry dichloromethane (DCM) (135 ml). 3-Amino-1-propanol (134 mmol, 10.33 ml) was dissolved in dry *N*,*N*-dimethylformamide (270 ml) and DMAP (92.6 mg) was added. To this solution the benzoyl chloride dissolved in dry dichloromethane (135 ml) was added and the resulting mixture heated at approximately 80 °C with stirring overnight. Afterwards the solvent was evaporated *in vacuo*. The residue was dissolved in DCM (50 ml) and washed with H_2O (50 ml). The organic layer was dried over sodium sulphate and evaporated to dryness. The residue was purified by silica gel column chromatography with a 6% MeOH and 94% DCM solvent system. 3.4669 g of the pure

amide **2** (95.29 % yield) was recovered. ^{1}H NMR (500 MHz, DMSO-d_6) δ 7.03 (s, 2H, CH), 6.59 (s, 1H, NH), 3.93 (s, 6H, OCH_3), 3.91 (s, 3H, OCH_3), 3.76 (t, J = 5.5 Hz, 2H, OCH_2), 3.66 (q, J = 6.1 Hz, 2H, NCH_2), 1.83 (m, 2H, CCH_2C). HRMS (ESI$^+$-TOF): m/z calcd for [$C_{13}H_{19}NNaO_5$]: 292.11554; found: 292.11609 [M+Na]$^+$.

3.1.2 (6-((3-hydroxypropyl)carbamoyl)-2,3,4-trimethoxyphenyl)mercury(II) chloride (**3**)

Amide **2** (3.4669 g, 12.87 mmol), $Hg(OAc)_2$ (4.1438 g, 13.0 mmol), and HOAc (3.19 ml) were dissolved in EtOH (17.80 ml) and refluxed for 5 h. After the mixture was cooled, it was stirred overnight at rt and then poured into a solution of KCl (3.8959 g, 52.26 mmol) in water (100 ml) to afford a copious white precipitate. After the reaction mixture was stirred for 10 min, the precipitate was isolated by filtration, washed with water, and dried at 55-60 °C, affording 3.4203 g of the desired product **3** (52.70% yield). ^{1}H NMR (500 MHz, $CDCl_3$) δ 7.19 (br, 1H, NH), 7.00 (s, 1H, CH), 3.91 (s, 3H, OCH_3), 3.90 (s, 3H, OCH_3), 3.88 (s, 3H, OCH_3), 3.80 (t, J = 5.4 Hz, 2H, OCH_2), 3.63 (m, 2H, NCH_2), 1.85 (p, J = 5.8 Hz, 2H, CCH_2C). ^{13}C NMR (126 MHz, $CDCl_3$) δ 168.62 (C=O), 155.89 ($\underline{C}OCH_3$), 154.17 ($\underline{C}OCH_3$), 145.28 ($\underline{C}OCH_3$), 132.69 ($\underline{C}C$=O), 106.18 (CH), 104.36 (CHg), 61.14 (OCH_3, OCH_2), 60.85 (OCH_3), 56.48 (OCH_3), 38.77 (NCH_2), 31.37 ($C\underline{C}H_2C$). HRMS (ESI$^+$-TOF): m/z calcd for [$C_{13}H_{18}HgNO_5$]: 470.08859; found: 470.08912 [M-Cl]$^+$.

3.1.3 Bis(6-((3-hydroxypropyl)carbamoyl)-2,3,4-trimethoxyphenyl)mercury (**4**)

Compound **3** (3.4203 g, 6.782 mmol) was dissolved in acetone (300 ml) and $(Me_4N)Cl$ (0.8378 g, 7.64 mmol) was added. This reaction mixture was stirred at rt for three days. After that, the mixture was filtered through $MgSO_4$ to produce a colourless solution and a grey sticky deposit. The filtrate was evaporated in vacuo. The residue weighed 2.4339 g. NMR analysis of this sample indicated that the majority of the starting material had not reacted.

The residue was dissolved in acetone (50 ml), $(Me_4N)Cl$ (0.4263 g, 3.89 mmol) was added and the mixture was stirred at rt for two days, before being filtered through $MgSO_4$. Following evaporation of the filtrate, a 2.1337 g residue was obtained.

The crude product was purified by silica gel column chromatography, the solvent system being 92% DCM and 8% MeOH. 0.9658 g (1.3102 mmol) of pure compound **4** (38.64% yield) was obtained. ^{1}H NMR (500 MHz, $CDCl_3$) δ 7.21 (t, J = 5.8 Hz, 1H, NH), 7.14 (s, 1H, Ar-$\underline{C}H$), 3.93 (s, 6H, Ar-O$\underline{C}H_3$), 3.89 (s, 3H, Ar-O$\underline{C}H_3$), 3.67 (t, J = 5.5 Hz, 2H, Ar-O$\underline{C}H_2$), 3.53 (q, J = 6.0 Hz, 2H, N$\underline{C}H_2$), 1.74 (m, 2H, C$\underline{C}H_2$C). ^{13}C NMR (126 MHz, $CDCl_3$) δ 171.76 (C=O), 157.83 ($\underline{C}OCH_3$), 153.15 ($\underline{C}OCH_3$), 152.21 (CHg), 145.21 ($\underline{C}OCH_3$), 136.35 ($\underline{C}C$=O), 107.83 (CH), 61.10 (OCH_3), 60.76 (OCH_3), 59.97

(OCH_2), 56.37 (OCH_3), 37.67 (NCH_2), 31.92 (CCH_2C). HRMS (ESI^+-TOF): *m/z* calcd for [$C_{26}H_{37}HgN_2O_{10}$]: 739.21546; found: 739.21490 $[M+H]^+$.

3.1.4 (6-((3-(4,4′-Dimethoxytrityloxy)propyl)carbamoyl)-2,3,4-trimethoxyphenyl)(6-((3-hydroxypropyl)carbamoyl)-2,3,4-trimethoxyphenyl)mercury (**5**)

Compound **4** (0.9658 g, 1.3102 mmol) was coevaporated from toluene (3 × 10 ml), after which the flask was sealed immediately and the ambient atmosphere replaced by nitrogen. Then dry Et_3N (2.62 mmol) and 4,4′-dimethoxytrityl chloride (0.4492 g, 1.326 mmol) dissolved in DCM (1.5 ml) were injected into the flask and kept overnight under vacuum condition. After that, the reaction mixture was diluted with DCM (50 ml) and washed with 5% aqueous $NaHCO_3$ (50 ml). pH was checked to ensure that the solution was basic. Then the organic phase was evaporated to dryness, followed by purification using silica gel column chromatography with 1% Et_3N, 5% MeOH and 94% DCM solvent system. 0.4707 g (0.4528 mmol) of the desired product **5** (34.56% yield) was recovered. ^1H NMR (500 MHz, $CDCl_3$) δ 7.41 (br, *J* = 3.2 Hz, 2H, NH), 7.30 (m, 4H, Ar-CH), 7.26 (m, 5H, Ar-CH), 6.94 (t, *J* = 5.2 Hz, 1H, Ar-CH), 6.87 (s, 1H, Ar-CH), 6.80 (d, *J* = 9.0 Hz, 4H, Ar-CH), 3.94 (m, 15H, OCH_3), 3.79 (s, 6H, OCH_3), 3.60 (m, 4H, NCH_2), 3.53 (s, 3H, OCH_3), 3.28 (t, *J* = 5.6 Hz, 2H, OCH_2), 1.91 (m, 2H, OCH_2), 1.70 (m, 3H, CCH_2C). ^{13}C NMR (126 MHz, $CDCl_3$) δ 171.48 (C=O), 158.08 ($COCH_3$), 153.02 ($COCH_3$), 151.15 ($COCH_3$), 145.01 ($COCH_3$), 137.23 (CHg), 136.04 (CH), 129.96 (CH), 127.50 (CH), 113.18 (CH), 108.61 (CH), 107.50 (CH), 86.57 (OCH_3), 62.75 (OCH_2), 60.94 (OCH_3), 59.41 (OCH_2), 56.17 (OCH_3), 55.21 (OCH_3), 39.26 (NCH_2), 37.08 (NCH_2), 32.23 (CCH_2C), 29.34 (CCH_2C). HRMS (ESI^+-TOF): *m/z* calcd for [$C_{47}H_{54}HgN_2O_{12}Na$]: 1063.32809; found: 1063.34181 $[M+ Na]^+$.

3.1.5 (6-((3-(bis(4,4′-Dimethoxytrityloxy)propyl)carbamoyl)-2,3,4-trimethoxyphenyl)(6-((3-(succinoyloxy)propyl)carbamoyl)-2,3,4-trimethoxyphenyl)mercury (**6**)

Compound **5** (0.4707 g, 0.4528 mmol) was dissolved in dry CH_2Cl_2 (3 mL) after being repeatedly coevaporated from dry toluene (3 × 10 ml). Succinic anhydride (55.4 mg, 0.554 mmol), Et_3N (75.8 µL, 0.546 mmol), and DMAP (5.7 mg, 0.047 mmol) were added. The mixture was then stirred overnight at room temperature and quantitative conversion was verified by LCMS. After that, silica gel column chromatography with 1% Et_3N, 5% MeOH, and 94% DCM was used to purify the product mixture. 0.2309 g (0.2026 mmol) of the desired product **6** was obtained (44.74% yield). ^1H NMR (500 MHz, $CDCl_3$) δ 8.01 (t, *J* = 5.9 Hz, 1H, NH), 7.38 (m, 2H, NCH_2), 7.26 (m, 7H, Ar-CH), 7.18 (br, *J* = 7.2 Hz, 1H, Ar-CH), 6.99 (s, 2H, Ar-CH), 6.78 (m, 4H, Ar-CH), 4.22 (t, *J* = 5.9 Hz, 2H,

COO-$\underline{CH_2}$), 3.95 (s, 3H, Ar-O$\underline{CH_3}$), 3.92 (s, 3H, Ar-O$\underline{CH_3}$), 3.90 (t, *J* = 2.0 Hz, 9H, Ar-O$\underline{CH_3}$), 3.76 (s, 6H, Ar-O$\underline{CH_3}$), 3.63 (s, 3H, Ar-O$\underline{CH_3}$), 3.53 (q, *J* = 6.2 Hz, 2H, CO$\underline{CH_2}$), 3.44 (m, 2H, N$\underline{CH_2}$), 3.18 (t, *J* = 5.8 Hz, 2H, O$\underline{CH_2}$), 2.54 (m, 4H, CO$\underline{CH_2}$), 1.88 (m, 4H, C$\underline{CH_2}$C). ^{13}C NMR (126 MHz, $CDCl_3$) δ 178.53 (C=O), 174.33 (C=O), 170.82 (C=O), 158.11 (C=O), 154.57 (C$\underline{O}CH_3$), 152.43 (C$\underline{O}CH_3$), 148.31 (C$\underline{O}CH_3$), 144.81 (C$\underline{O}CH_3$), 137.33 (CHg), 136.40 (CH), 129.96 (CH), 128.08 (CH), 127.81 (CH), 126.76 (CH), 113.08 (CH), 108.20 (CH), 106.54 (CH), 62.19 (OCH_3), 61.04 (OCH_3), 60.70 (OCH_3), 60.55 (OCH_3), 56.39 (OCH_3), 56.10 (OCH_3), 55.17 (OCH_3), 39.13 (NCH_2), 38.73 (NCH_2), 36.04 (C$\underline{C}H_2$C), 32.19 (C$\underline{C}H_2$C), 31.17 (C$\underline{C}H_2$C), 29.61 (C$\underline{C}H_2$C), 27.48 (C$\underline{C}H_2$C).

3.1.6 Immobilization of the diarylmercury compound **6** on solid support

LCAA-CPG solid support (153.2 mg) was washed with 20 ml of TEA/MeOH (1:9, *v*/*v*) and dried under vacuum. The dry solid support was suspended in dry DMF containing compound **6** (35.8 mg, 31.4 µmol). PyBOP (18.3 mg, 35.14 µmol) and DIPEA (10.6 µl, 61.0 µmol) were added. The suspension was shaken overnight, filtered and rinsed with DMF (15 ml) and DCM (15 ml). Then it was dried using compressed air. The support was filtered and treated with a mixture of capping solution B1 (2.5 ml), capping solution B2 (2.5 ml) and capping solution A (5 ml). After that, the support was filtered, washed with THF and DCM, and dried under vacuum. DMTr-cation assay was measured by UV-vis spectroscopy (SHIMADZU UV 1900). To determine loading of the solid support by DMTr cation assay, 3.0 mg of the support was weighed in a centrifuge tube and 10 ml of 3 % dichloroacetic acid in toluene was added. Absorption of this solution at 503 nm was measured and the loading was obtained by following calculation.

$$Loading = \frac{A503\ x\ V}{76} \times \left(\frac{1000}{m}\right)$$

$$= \frac{1.0121x\ 10\ x\ 1000}{76\ x\ 3}$$

$$= 44.4\ \mu mol/g$$

Where

V = the volume of the sample in ml

A503 = absorbance at 503 nm

m = the weight of the solid support in mg

3.1.7 Acidic and Oxidative Stability of compound **4**

A sample of compound **4** (0.0202 g, 0.0274 mmol) was dissolved in a mixture of pyridine-d_5 (450 µl) and D_2O (50 µl) in an NMR tube, and the initial spectrum was recorded. 6.35 mg I_2 (0.05 M) was then added, and a second spectrum was acquired immediately to monitor oxidative transformation of the dimer. After adding I_2, compound **4** was consumed which was evidenced by the change of the aromatic region and appearance of new signals in ^{1}H NMR.

In a separate experiment, a solution of compound **4** (0.0203 g, 0.0275 mmol) in $CDCl_3$ (500 µl) was prepared and an initial spectrum was recorded. After that, 15 µl of dichloroacetic acid was added. A second spectrum was recorded within 2 min after acid addition to assess the stability of the dimer under acidic conditions. Addition of dichloroacetic acid also led to decomposition of compound **4**, giving signals of a new compound in ^{1}H NMR.

3.2 Synthesis of the azide-functionalized diarylmercury compound

3.2.1 3,4,5-trimethoxybenzoyl chloride (**7**)

3,4,5-trimethoxybenzoic acid **1** (6.01 g, 28.32 mmol) and thionyl chloride (80 ml) were refluxed for 3 h. Then the mixer was evaporated to dryness. The residue was evaporated again from toluene to get benzoyl chloride **7** (6.645 g, 28.81 mmol) with approximately 100% yield.

3.2.2 *N*-(2-(2-(2-(2-azidoethoxy)ethoxy)ethoxy)ethyl)-3,4,5-trimethoxybenzamide (**8**)

Compound **7** (0.9590 g, 4.157 mmol) was dissolved in DMF (10 ml). As a catalyst, few mg DMAP was added. Then, 11-azido-3,6,9-trioxanundecan-1-amine (0.6032 g, 2.76 mmol) and triethylamine (1 ml) were added and the reaction mixture was stirred at rt for 3 d. The reaction was followed by TLC and approximately 50 % completion was observed after 3 d. Additional benzoyl chloride **7** (0.9572 g, 4.150 mmol) and triethylamine (1.0 ml) were added and the stirring continued overnight at rt. The crude product was purified by five passes through a silica gel column. Different solvent systems of MeOH (4-6 %) in DCM were used during the purification.

The final yield of product **8** was 0.3686 g (0.8937 mmol), corresponding to a 32.14% yield. ^{1}H NMR (500 MHz, $CDCl_3$) δ 7.08 (br, J = 5.0 Hz, 1H, NH), 7.06 (s, 2H, Ar-CHa, Ar-CHe), 3.86 (s, 6H, Ar-OCH_3b, Ar-OCH_3d), 3.85 (s, 3H, Ar-OCH_3c), 3.61 (m, J = 5.0 Hz, 14H, 7 × CH_2f), 3.31 (t, J = 5.1 Hz, 2H, N_3-CH_2g). ^{13}C NMR (126 MHz, $CDCl_3$) δ 167.01 (C-9), 152.82 (C-16, C-18), 140.48 (C-17), 129.80 (C-10), 104.35 (C-11, C-15), 70.38 (C-3), 70.29 (C-4), 69.98 (C-5), 69.75 (C-6), 69.56 (C-7), 60.60 (C-17), 56.02 (C-16, C-18), 50.37 (C-1, C-8), 39.73 (C-2). HRMS (ESI$^+$-TOF): *m/z* calcd for [$C_{18}H_{29}N_4O_7$]: 413.20362; found: 413.20889 [M+H]$^+$.

3.2.3 Bis(6-((2-(2-(2-(2-azidoethoxy)ethoxy)ethoxy)ethyl)carbamoyl)-2,3,4-trimethoxyphenyl)mercury (**10**)

Compound **8** (0.104 g, 0.253 mmol) and mercuric acetate (0.161 g, 0.505 mmol) were dissolved in MeOD (2 ml) in an NMR tube and heated at 55 °C overnight. ^{1}H NMR analysis indicated complete consumption of compound **8**, whereas ESI-MS showed that the product mixture contained both the monomercurated compound **9** and the corresponding diarylmercury compound **10**. The reaction mixture was transferred to a microcentrifuge tube, treated with $(Me_4N)Cl$ (0.263 g, 2.40 mmol) to promote dimerization, and kept overnight at rt.

After 24 h, ^{1}H NMR data indicated that conversion toward the dimeric product was still incomplete, and a second portion of $(Me_4N)Cl$ (0.263 g, 1.20 mmol) was added. NMR spectra recorded 2 h after this addition showed approximately 50% formation of the dimercurated dimer **10** and a corresponding decrease in the monomercurated intermediate **9**. The mixture was further kept overnight at rt, after which ^{1}H NMR confirmed near-complete conversion to the dimer. Solvents were evaporated and the residue was purified by RP-HPLC on a Hypersil ODS C18 column (250 × 4.6 mm, 5 µm), eluting with a linear gradient (10 to 40% over 40 min, flow rate 0.6 ml min^{-1}) of ACN in 50 mM aqueous triethylammonium acetate (pH = 7.0). UV absorbance at λ = 260 nm was used to detect the peaks. 0.0148 g (0.0145 mmol) of the diarylmercury product **10** (11.45 % yield) was obtained. ^{1}H NMR (500 MHz, $CDCl_3$) δ 7.14 (s, 2H, Ar-CHa, Ar-CHh), 6.95 (d, J = 5.1 Hz, 2H, NH), 3.94 (s, J = 5.2 Hz, 12H, Ar-CH_2c-f), 3.93 (s, 6H, Ar-OCH_3b, Ar-OCH_3g), 3.64 (m, 28H, 7 × CH_2k, 7 × CH_2i), 3.37 (t, J = 5.0 Hz, 4H, N_3-CH_2l, N_3-CH_2j). ^{13}C NMR (126 MHz, $CDCl_3$) δ 170.83 (C- 9, 28), 158.00 (C- 16, 20), 152.93 (C- 13, 24), 152.61 (C- 18, 19), 145.22 (C- 14, 22), 136.72 (C- 1, 27), 107.88 (C- 11, 26), 70.68- 69.90 (C- 2-7, 30-35), 61.06 (C- 17, 21), 60.76 (C- 15, 23), 56.51 (C- 13, 25), 50.66 (C- 1, 36), 44.86 (s, 1C), 40.10 (C-8,29). HRMS (ESI$^+$-TOF): *m/z* calcd for $[C_{36}H_{55}HgN_8O_{14}]$: 1025.35442; found: 1025.36332 $[M+H]^+$.

The monomeric arylmercury compound **9** (0.0049 g, 0.0073 mmol) was also obtained from the RP-HPLC purification (2.9 % yield). ^{1}H NMR (600 MHz, $CDCl_3$) δ 7.06 (s, 1H, Ar-CHa), 6.76 (s, 1H, NH), 3.93 (s, 6H, Ar-OCH_3c, Ar-OCH_3d), 3.90 (s, 3H, Ar-OCH_3b), 3.67 (m, J = 3.5 Hz, 14H, 7x CH_2g), 3.36 (t, J = 5.0 Hz, 2H, NH_3-CH_2h).

3.2.4 Oligonucleotide synthesis

The oligonucleotides were prepared on an automated ÄKTA Oligopilot plus DNA/RNA synthesizer. **ON1** was first synthesized in a 1 µmol scale using a dT-CPG solid support (500 Å, 42 µmol g^{-1}). Solutions (0.10 M) of nucleoside phosphoramidites A (2.55 ml), C (3.60 ml), G (4.05 ml) and T (2.85 ml) were prepared in anhydrous acetonitrile. For incorporation of the 5′-DBCO–TEG, 42.53 mg of

the respective phosphoramidite building block was dissolved in 600 µl of dry acetonitrile to afford a 0.10 M solution. This solution was used for a single coupling step at the end of the sequence.

The trityl response for the 500 Å CPG solid support showed coupling efficiency and started declining after about 60 coupling cycles. After completion of the synthesis, the solid support was washed with acetonitrile and 1 ml of aqueous ammonia (35%, v/v) was added into it. The suspension was incubated at 55 °C overnight to cleave and deprotect the oligonucleotide. Then the supernatant was removed from the solid support and lyophilized overnight. According to UPLC-HRMS, the crude product did not contain the expected full-length oligonucleotide. Instead, a distribution of shorter oligonucleotides was observed.

The synthesis was repeated using a dT-CPG solid support with a larger pore size (1000 Å, 32 µmol g^{-1}), more suitable for the relatively long aptamer sequence. For the repeat synthesis, slightly larger volumes of the solutions (0.10 M) of nucleoside phosphoramidites A (3.00 ml), C (3.90 ml), G (4.35 ml) and T (3.15 ml) were prepared. Trityl responses were observed declining after around 100 coupling cycles. According to HRMS, the crude product contained the target oligonucleotide as the major component with only minor impurities. The crude product was purified by RP-HPLC. A BioZenTM oligo 00F-4790-E0-column (150 x 4.6 mm, 2.6 µm) was used in RP-HPLC, eluting with a linear gradient (10 to 40% over 35 min, flow rate 0.6 ml min^{-1}) of ACN in 50 mM aq triethylammonium acetate (pH = 7.0). UV absorbance at λ = 290 nm was used to distinguish the peaks.

The main fraction, containing the desired product, eluted at 11.99 min. Hexylamine was added to the oligonucleotide solutions (50 µl / 10 ml) prior to lyophilisation. HRMS confirmed the presence of the desired oligonucleotide in the evaporated fraction. The concentration of the oligonucleotide stock solution was determined as 114 µM by UV absorbance at λ = 260 nm (0.1828) and ε = 798722.

3.2.5 Conjugation of oligonucleotides with the diarylmercury compound **10**

Aptamer **ON1**, single-stranded **ON2** and double helix **ON2•ON3** conjugates were mixed in microcentrifuge tubes with different ratios (0.5-3.0) of the diarylmercury compound **10** to the oligonucleotides. The concentrations of **ON1**, **ON2** and **ON3** were 0.114 mM, 0.7 mM and 0.3 mM, respectively. The pH of the solutions was adjusted to 7.0 with TEAA (0.18 M). The reaction mixtures were checked by UPLC-HRMS to confirm the maximum conjugate formation. After 2 h, maximum concentrations of the desired product were observed, with some impurities. The mixtures were purified using RP-HPLC. A BioZenTM oligo 00F-4790-E0-column (150 x 4.6 mm, 2.6 µm) was used

in RP-HPLC, eluting with a linear gradient (10 to 60% over 40 min, flow rate 0.6 ml min^{-1}) of ACN in 50 mM aqueous triethylammonium acetate (pH = 7.0). UV absorbance at λ = 260 nm was used to distinguish the peaks. UPLC-HRMS data confirmed the purity of the products.

3.2.6 UV melting profile of the cyclooctyne functionalized aptamer

To determine the UV melting profile of **ON1**, PerkinElmer Lambda 35 spectrophotometer equipped with a Peltier temperature control unit was used. Sample of **ON1** (1.0 mM) was prepared with sodium cacodylate buffer (20 mM, pH 7.4) and $NaClO_4$ (80 mM) in Milli-Q water to a final volume of 400 µl. A buffer sample lacking the aptamer was used as a reference. Samples were prepared in 1.0 cm path length quartz cuvettes, and UV melting profiles were recorded by monitoring the absorbance at 260 nm while ramping the temperature at 0.5 °C min^{-1} over three consecutive heating and cooling cycles. The melting temperature (T_m) was obtained from the maximum of the first derivative of the A_{260} versus temperature curve.

4. Conclusion

The synthesis of organomercurial compounds, particularly the mercuration steps, was a challenge in this study. These steps necessitated meticulous optimization to separate the dimeric species from monomeric intermediates and side products. However, once separated from its monomer counterpart **9**, the dimeric diarylmercury compound **10** is chemically stable and can be stored for a long time as long as it is kept below 0 °C. Compound **10** functions as a stable precursor for conjugation to ONs using DBCO-bearing linkers. Double-stranded conjugates are significantly more robust than single-stranded ones. Since double helix DNA is more densely packed and strong, the dimeric diarylmercury scaffold is physically better protected and undergoes less bending and strain. Besides, in a double-helical DNA, the donor atoms most likely to coordinate Hg(II) are engaged in base pairing.

There is an obvious conceptual benefit to the bivalent conjugate construction. For each dimeric diarylmercury-aptamer conjugate, one Hg signal can be detected using LA-ICP-MS. When both aptamer arms bind their targeted epitopes, this bivalent design can theoretically bind up to two GFAP proteins. The same approach may theoretically be applied to aptamers that identify proteins linked to cancer, allowing for stoichiometric elemental readout of target burden in tissue. This will allow more patient-specific drug dosing to reduce off-target harm.

To sum up, this study shows that it is possible to incorporate a diarylmercury scaffold into a DNA aptamer while maintaining sufficient chemical stability. Hg detectability for LA-ICP-MS imaging of a specific protein target in brain tissue is also possible. However, it also draws attention to practical

issues that need to be resolved before such tags can be widely used, such as the stability of the conjugates and the synthetic work needed to access and purify organomercurial compounds.

Future studies are needed to focus on systematic optimization of conjugate concentration and incubation conditions for tissue labelling. Refinement of LA-ICP-MS acquisition parameters for quantitative Hg imaging at required cellular length scales, and exploration of alternative aryl frameworks or linker designs that further stabilize the Hg–C core without compromising aptamer binding are also needed. These efforts will clarify the ultimate potential of dimeric diarylmercury-aptamer conjugates as a general platform for heavy-atom tagging in quantitative elemental bio-imaging.

5. Reference

1. Ellington, A. D., & Szostak, J. W. (1990). In vitro selection of RNA molecules that bind specific ligands. *Nature*, *346*(6287), 818–822.
2. Xiao, X., Li, H., Zhao, L., Zhang, Y., & Liu, Z. (2021). Oligonucleotide aptamers: Recent advances in their screening, molecular conformation and therapeutic applications. *Biomedicine & Pharmacotherapy*, *143*, 112232.
3. Ozer, A., Pagano, J. M., & Lis, J. T. (2014). New Technologies Provide Quantum Changes in the Scale, Speed, and Success of SELEX Methods and Aptamer Characterization. *Molecular therapy. Nucleic acids*, *3*(8), e183.
4. Spill, F., Weinstein, Z. B., Irani Shemirani, A., Ho, N., Desai, D., & Zaman, M. H. (2016). Controlling uncertainty in aptamer selection. *Proceedings of the National Academy of Sciences*, *113*(43), 12076-12081.
5. Bognár, Z., & Gyurcsányi, R. E. (2020). Aptamers against Immunoglobulins: Design, Selection and Bioanalytical Applications. *International journal of molecular sciences*, *21*(16), 5748.
6. Zhuo, Z., Yu, Y., Wang, M., Li, J., Zhang, Z., Liu, J., & Zhang, B. (2017). Recent advances in SELEX technology and aptamer applications in biomedicine. *International journal of molecular sciences*, *18*(10), 2142.
7. Tuerk, C., & Gold, L. (1990). Systematic evolution of ligands by exponential enrichment: RNA ligands to bacteriophage T4 DNA polymerase. *Science*, *249*(4968), 505-510.

8. Chandola, C., Kalme, S., Casteleijn, M. G., Urtti, A., & Neerathilingam, M. (2016). Application of aptamers in diagnostics, drug-delivery and imaging. *Journal of biosciences*, *41*(3), 535-561.
9. Odeh, F., Nsairat, H., Alshaer, W., Ismail, M. A., Esawi, E., Qaqish, B., Bawab, A. A., & Ismail, S. I. (2019). Aptamers Chemistry: Chemical Modifications and Conjugation Strategies. *Molecules (Basel, Switzerland)*, *25*(1), 3.
10. Keefe, A. D., Pai, S., & Ellington, A. (2010). Aptamers as therapeutics. *Nature reviews. Drug discovery*, *9*(7), 537–550.
11. Trujillo, C. A., Nery, A. A., Alves, J. M., Martins, A. H., & Ulrich, H. (2007). Development of the anti-VEGF aptamer to a therapeutic agent for clinical ophthalmology. *Clinical ophthalmology (Auckland, N.Z.)*, *1*(4), 393–402.
12. Catuogno, S., Esposito, C. L., & de Franciscis, V. (2016). Aptamer-Mediated Targeted Delivery of Therapeutics: An Update. *Pharmaceuticals (Basel, Switzerland)*, *9*(4), 69.
13. Xie, S., Sun, W., Fu, T., Liu, X., Chen, P., Qiu, L., ... & Tan, W. (2023). Aptamer-based targeted delivery of functional nucleic acids. *Journal of the American Chemical Society*, *145*(14), 7677-7691.
14. Shraim, A. S., Abdel Majeed, B. A., Al-Binni, M. A., & Hunaiti, A. (2022). Therapeutic Potential of Aptamer-Protein Interactions. *ACS pharmacology & translational science*, *5*(12), 1211–1227.
15. Walter, J.-G., Stahl, F. and Scheper, T. (2012), Aptamers as affinity ligands for downstream processing. Eng. Life Sci., 12: 496-506.
16. Gragoudas, E. S., Adamis, A. P., Cunningham Jr, E. T., Feinsod, M., & Guyer, D. R. (2004). Pegaptanib for neovascular age-related macular degeneration. *New england journal of medicine*, *351*(27), 2805-2816.
17. Shukla, D., Namperumalsamy, P., Goldbaum, M., & Cunningham Jr, E. T. (2007). Pegaptanib sodium for ocular vascular disease. *Indian journal of ophthalmology*, *55*(6), 427-430.
18. Van den Avont, A., & Sharma-Walia, N. (2023). Anti-nucleolin aptamer AS1411: an advancing therapeutic. *Frontiers in molecular biosciences*, *10*, 1217769.
19. Rosenberg, J. E., Bambury, R. M., Van Allen, E. M., Drabkin, H. A., Lara, P. N., Jr, Harzstark, A. L., Wagle, N., Figlin, R. A., Smith, G. W., Garraway, L. A., Choueiri, T., Erlandsson, F., & Laber, D. A. (2014). A phase II trial of AS1411 (a novel nucleolin-targeted DNA aptamer) in metastatic renal cell carcinoma. *Investigational new drugs*, *32*(1), 178–187.

20. Huang, Y. F., Shangguan, D., Liu, H., Phillips, J. A., Zhang, X., Chen, Y., & Tan, W. (2009). Molecular assembly of an aptamer-drug conjugate for targeted drug delivery to tumor cells. *Chembiochem : a European journal of chemical biology*, *10*(5), 862–868.
21. Su, M., Liu, Y., Lin, H. *et al.* An aptamer-drug conjugate for promising cancer therapy with comprehensive evaluation from rodents to non-human primates. *Sig Transduct Target Ther* 10, 316 (2025).
22. Sivakumar P, Kim S, Kang HC, Shim MS. Targeted siRNA delivery using aptamer-siRNA chimeras and aptamer-conjugated nanoparticles. WIREs Nanomed Nanobiotechnol. 2019;11:e1543.
23. McNamara, J. O., Andrechek, E. R., Wang, Y., Viles, K. D., Rempel, R. E., Gilboa, E., ... & Giangrande, P. H. (2006). Cell type–specific delivery of siRNAs with aptamer-siRNA chimeras. *Nature biotechnology*, *24*(8), 1005-1015.
24. Li, Y., Shao, T., Kuang, J., Yi, H., Zhu, L., & Wang, X. Q. (2025). Aptamers as a New Frontier in Molecular Cancer Imaging Technologies. *Chemical & biomedical imaging*, *3*(5), 267–279.
25. Li, C. H., Kuo, T. R., Su, H. J., Lai, W. Y., Yang, P. C., Chen, J. S., ... & Chen, C. C. (2015). Fluorescence-guided probes of aptamer-targeted gold nanoparticles with computed tomography imaging accesses for in vivo tumor resection. *Scientific reports*, *5*(1), 15675.
26. Javier, D. J., Nitin, N., Levy, M., Ellington, A., & Richards-Kortum, R. (2008). Aptamer-targeted gold nanoparticles as molecular-specific contrast agents for reflectance imaging. *Bioconjugate chemistry*, *19*(6), 1309-1312.
27. Kim, S. T., Kim, H. G., Kim, Y. M., Han, H. S., Cho, J. H., Lim, S. C., Lee, T., & Jahng, G. H. (2023). An aptamer-based magnetic resonance imaging contrast agent for detecting oligomeric amyloid-β in the brain of an Alzheimer's disease mouse model. *NMR in biomedicine*, *36*(3), e4862.
28. Yu, Y., Dang, J., Liu, X., Wang, L., Li, S., Zhang, T., & Ding, X. (2020). Metal-labeled aptamers as novel nanoprobes for imaging mass cytometry analysis. *Analytical chemistry*, *92*(9), 6312-6320.
29. Xu, L., Feng, Y., Wang, T., Li, S., Xu, K., Sun, Y., ... & Tan, W. (2024). Aptamer-Based Cell-Surface Profiling with Single-Cell Resolution Enables Precise Cancer Characterization. *ccs Chemistry*, *6*(1), 196-207.
30. Base Pair Biotechnologies. DNA Aptamers or RNA Aptamers? https://basepairbio.com/dna-aptamers-rna-aptamers/ (accessed July 20, 2026).
31. Maradani, B.S., Parameswaran, S. & Subramanian, K. Development and characterization of DNA aptamer against Retinoblastoma by Cell-SELEX. *Sci Rep* **12**, 16178 (2022).

32. Colburn, M. E., Delaney, M. A., Anchor, G. C., & Terio, K. A. (2024). Effect of formalin-fixation and paraffin-embedded tissue storage times on RNAscope in situ hybridization signal amplification. *Journal of veterinary diagnostic investigation : official publication of the American Association of Veterinary Laboratory Diagnosticians, Inc*, *36*(4), 498–505.
33. Zhu, G., Niu, G., & Chen, X. (2015). Aptamer-Drug Conjugates. *Bioconjugate chemistry*, *26*(11), 2186–2197.
34. Wang, R., Zhu, G., Mei, L., Xie, Y., Ma, H., Ye, M., ... & Tan, W. (2014). Automated modular synthesis of aptamer–drug conjugates for targeted drug delivery. *Journal of the American Chemical Society*, *136*(7), 2731-2734.
35. Kim, S. T., Kim, H. G., Kim, Y. M., Han, H. S., Cho, J. H., Lim, S. C., Lee, T., & Jahng, G. H. (2023). An aptamer-based magnetic resonance imaging contrast agent for detecting oligomeric amyloid-β in the brain of an Alzheimer's disease mouse model. *NMR in biomedicine*, *36*(3), e4862.
36. Park, J. W., Tian, Y., Kim, S. T., Park, C., Kim, Y. M., Chung, H. K., Kim, K. M., & Jahng, G. H. (2024). Oligomeric amyloid-β targeted contrast agent for MRI evaluation of Alzheimer's disease mouse models. *Frontiers in pharmacology*, *15*, 1392729.
37. N.Ullah, T. A.Bruce-Tagoe, G. A.Asamoah, S.Soleimani, and M. K.Danquah, "Radiolabeled Aptamers for Bioimaging Applications in Oncology and Infectious Diseases," Journal of Labelled Compounds and Radiopharmaceuticals68, no. 14 (2025): e70001.
38. Fu, Z., & Xiang, J. (2020). Aptamer-Functionalized Nanoparticles in Targeted Delivery and Cancer Therapy. *International journal of molecular sciences*, *21*(23), 9123.
39. Doble, P. A., de Vega, R. G., Bishop, D. P., Hare, D. J., & Clases, D. (2021). Laser ablation–inductively coupled plasma–mass spectrometry imaging in biology. *Chemical reviews*, *121*(19), 11769-11822.
40. Becker, J. S., Zoriy, M., Matusch, A., Wu, B., Salber, D., Palm, C., & Becker, J. S. (2010). Bioimaging of metals by laser ablation inductively coupled plasma mass spectrometry (LA-ICP-MS). *Mass spectrometry reviews*, *29*(1), 156–175.
41. Reifschneider, O., Wehe, C. A., Raj, I., Ehmcke, J., Ciarimboli, G., Sperling, M., & Karst, U. (2013). Quantitative bioimaging of platinum in polymer embedded mouse organs using laser ablation ICP-MS. *Metallomics*, *5*(10), 1440-1447.
42. Moreno-Gordaliza, E., Giesen, C., Lázaro, A., Esteban-Fernández, D., Humanes, B., Cañas, B., & Gómez-Gómez, M. M. (2011). Elemental bioimaging in kidney by LA–ICP–MS as a tool to study nephrotoxicity and renal protective strategies in cisplatin therapies. *Analytical chemistry*, *83*(20), 7933-7940.

43. Theiner, S., Kornauth, C., Varbanov, H. P., Galanski, M., Van Schoonhoven, S., Heffeter, P., Berger, W., Egger, A. E., & Keppler, B. K. (2015). Tumor microenvironment in focus: LA-ICP-MS bioimaging of a preclinical tumor model upon treatment with platinum(IV)-based anticancer agents. *Metallomics : integrated biometal science*, *7*(8), 1256–1264.
44. Iwase, M., Tanaka, Y. K., Suzuki, N., & Ogra, Y. (2021). Determination of spatial mercury concentration by laser ablation-inductively coupled plasma mass spectrometry. *The Journal of toxicological sciences*, *46*(5), 193–198.
45. Wang, H. A., Grolimund, D., Giesen, C., Borca, C. N., Shaw-Stewart, J. R., Bodenmiller, B., & Günther, D. (2013). Fast chemical imaging at high spatial resolution by laser ablation inductively coupled plasma mass spectrometry. *Analytical chemistry*, *85*(21), 10107-10116.
46. Sabine Becker J. (2013). Imaging of metals in biological tissue by laser ablation inductively coupled plasma mass spectrometry (LA-ICP-MS): state of the art and future developments. *Journal of mass spectrometry: JMS*, *48*(2), 255–268.
47. Sabine Becker, J., Matusch, A., Palm, C., Salber, D., Morton, K. A., & Susanne Becker, J. (2010). Bioimaging of metals in brain tissue by laser ablation inductively coupled plasma mass spectrometry (LA-ICP-MS) and metallomics. *Metallomics*, *2*(2), 104-111.
48. Sabine Becker J. (2013). Imaging of metals in biological tissue by laser ablation inductively coupled plasma mass spectrometry (LA-ICP-MS): state of the art and future developments. *Journal of mass spectrometry: JMS*, *48*(2), 255–268.
49. Kutscher, D., Asogan, D., Mudway, I., Brekke, P., Beales, C., Wang, X., & Stewart, T. J. (2020). Imaging of trace elements using laser ablation–inductively coupled plasma–mass spectrometry: emerging new applications. *Spectroscopy*, *35*(S4), 16-26.
50. Burger, M., Gundlach-Graham, A., Allner, S., Schwarz, G., Wang, H. A., Gyr, L., & Günther, D. (2015). High-speed, high-resolution, multielemental LA-ICP-TOFMS imaging: Part II. Critical evaluation of quantitative three-dimensional imaging of major, minor, and trace elements in geological samples. *Analytical chemistry*, *87*(16), 8259-8267.
51. Schweikert, A., Theiner, S., Wernitznig, D., Schoeberl, A., Schaier, M., Neumayer, S., Keppler, B. K., & Koellensperger, G. (2022). Micro-droplet-based calibration for quantitative elemental bioimaging by LA-ICPMS. *Analytical and bioanalytical chemistry*, *414*(1), 485–495.
52. Boger, V., Pirkwieser, P., Orth, N., Koehler, M., & Somoza, V. (2025). AFM-optimized single-cell level LA-ICP-MS imaging for quantitative mapping of intracellular zinc concentration in immobilized human parietal cells using gelatin droplet-based calibration. *Analytica chimica acta*, *1355*, 343999.

53. Hare, D. J., Kysenius, K., Paul, B., Knauer, B., Hutchinson, R. W., O'Connor, C., Fryer, F., Hennessey, T. P., Bush, A. I., Crouch, P. J., & Doble, P. A. (2017). Imaging Metals in Brain Tissue by Laser Ablation - Inductively Coupled Plasma - Mass Spectrometry (LA-ICP-MS). *Journal of visualized experiments: JoVE*, (119), 55042.
54. Marolt, G., Novak, S., Kokalj, A. J., Talaber, I., Kononenko, V., Loureiro, S., ... & Drobne, D. (2023). High throughput laser ablation ICP-MS bioimaging of silver distribution in animal organisms and plant tissue after exposure to silver sulfide nanoparticles. *Journal of Analytical Atomic Spectrometry*, *38*(11), 2396-2404.
55. Castellanos-Garcia, L. J., Sikora, K. N., Doungchawee, J., & Vachet, R. W. (2021). LA-ICP-MS and MALDI-MS image registration for correlating nanomaterial biodistributions and their biochemical effects. *Analyst*, *146*(24), 7720-7729.
56. Hu, Y., Hu, Z., & Zhang, W. (2025). New Numerical Inversion Method to Improve the Spatial Accuracy of Elemental Imaging for LA-ICP-MS. *Analytical Chemistry*, *97*(4), 2486-2493.
57. Chaurand, P., Schwartz, S. A., & Caprioli, R. M. (2002). Imaging mass spectrometry: a new tool to investigate the spatial organization of peptides and proteins in mammalian tissue sections. *Current opinion in chemical biology*, *6*(5), 676-681.
58. Weber, P. K., Debliqui, M., Defouilloy, C., Mayali, X., Liu, M. C., Hestrin, R., ... & Thomen, A. (2024). The nanosims-hr: The next generation of high spatial resolution dynamic SIMS. *Analytical Chemistry*, *96*(49), 19321-19329.
59. Gutschmayer, S., Yu, J., Geist, B.K. *et al.* Whole-Body [^{18}F]FDG-PET/CT Imaging of Healthy Controls: Test/Retest Data for Systemic, Multi-Organ Analysis. *Sci Data* **12**, 1707 (2025).
60. Melnick, J. G., Yurkerwich, K., & Parkin, G. (2009). Synthesis, structure, and reactivity of two-coordinate mercury alkyl compounds with sulfur ligands: relevance to mercury detoxification. *Inorganic chemistry*, *48*(14), 6763–6772.
61. Yurkerwich, K., Quinlivan, P. J., Rong, Y., & Parkin, G. (2016). Phenylselenolate Mercury Alkyl Compounds, PhSeHgMe and PhSeHgEt: Molecular Structures, Protolytic Hg-C Bond Cleavage and Phenylselenolate Exchange. *Polyhedron*, *103*(Pt B), 307–314.
62. BenchChem. (2025). *Synthesis of organomercury compounds using Grignard reagents* [Technical guide]. BenchChem. Retrieved June 6, 2026, from https://www.benchchem.com/pdf/Synthesis_of_organomercury_compounds_using_Grignard_reagents.pdf
63. Barron, A. R. 5.04: Organomercury Compounds. In Chemistry of the Main Group Elements; LibreTexts. https://chem.libretexts.org/... (accessed July 20, 2026).

64. Deacon, G. B., & Felder, P. W. (1970). Organomercury compounds. X. Reactions of diarylmercurials with arenesulphinic and-sulphonic acids. *Australian Journal of Chemistry*, *23*(6), 1275-1278.
65. Snell, J., Qian, J., Johansson, M., & Smit, K. (1998). Stability and reactions of mercury species in organic solution. *Analyst*, *123*(5), 905-909.
66. Song, Y., Jiang, T., Liem-Nguyen, V., Sparrman, T., Björn, E., & Skyllberg, U. (2018). Thermodynamics of Hg(II) Bonding to Thiol Groups in Suwannee River Natural Organic Matter Resolved by Competitive Ligand Exchange, Hg L_{III}-Edge EXAFS and ^{1}H NMR Spectroscopy. *Environmental science & technology*, *52*(15), 8292–8301.
67. Ngu-Schwemlein, M., Merle, J. K., Healy, P., Schwemlein, S., & Rhodes, S. (2009). Thermodynamics of the complexation of Hg (II) by cysteinyl peptide ligands using isothermal titration calorimetry. *Thermochimica acta*, *496*(1-2), 129-135.
68. Seyferth, D., & Spohn, R. J. (1972). *U.S. Patent No. 3,692,652*.
69. Seyferth, D., & Spohn, R. J. (1969). A convenient high yield dicobalt octacarbonyl catalyzed synthesis of diaryl ketones from diarylmercury compounds and carbon monoxide. *Journal of the American Chemical Society*, *91*(22), 6192-6193.
70. Banerjee, M., & Roy, G. (2017). Cleavage of Hg–C Bonds of Organomercurials Induced by ImOHSe via Two Distinct Pathways. *Inorganic Chemistry*, *56*(21), 12739-12750.
71. Karri, R., Chalana, A., Kumar, B., Jayadev, S. K., & Roy, G. (2019). Exploiting the κ2-Fashioned Coordination of [Se2]-Donor Ligand L3Se for Facile Hg− C Bond Cleavage of Mercury Alkyls and Cytoprotection against Methylmercury-Induced Toxicity. *Chemistry–A European Journal*, *25*(55), 12810-12819.
72. Partyka, D. V., & Gray, T. G. (2009). Facile syntheses of homoleptic diarylmercurials via arylboronic acids. *Journal of Organometallic Chemistry*, *694*(2), 213-218.
73. Kotammagari, T. K., Al-Waeel, M., Lukkari, J., & Lönnberg, T. (2024). Organomercury oligonucleotide–polydopamine nanoparticle assemblies discriminate between target sequences by Hg (ii)-mediated base pairing. *RSC advances*, *14*(51), 38279-38284.
74. Aro-Heinila, A., Lonnberg, T., & Virta, P. (2019). 3-fluoro-2-mercuri-6-methylaniline nucleotide as a high-affinity nucleobase-specific hybridization probe. *Bioconjugate Chemistry*, *30*(8), 2183-2190.
75. Wilhelm, M., Saak, W., & Strasdeit, H. (2000). Phenylmercury chloride: Its single-crystal X-ray structure and some aspects of its biological chemistry. *Zeitschrift für Naturforschung B*, *55*(1), 35-38.

76. Van Acker, T., Van Malderen, S. J., Van Heerden, M., McDuffie, J. E., Cuyckens, F., & Vanhaecke, F. (2016). High-resolution laser ablation-inductively coupled plasma-mass spectrometry imaging of cisplatin-induced nephrotoxic side effects. *Analytica chimica acta*, *945*, 23–30.
77. Iwase, M., Tanaka, Y. K., Suzuki, N., & Ogra, Y. (2021). Determination of spatial mercury concentration by laser ablation-inductively coupled plasma mass spectrometry. *The Journal of toxicological sciences*, *46*(5), 193–198.
78. Günther, D., & Hattendorf, B. (2005). Solid sample analysis using laser ablation inductively coupled plasma mass spectrometry. *TrAC Trends in Analytical Chemistry*, *24*(3), 255-265.
79. Gilpin, I. M. F., Ullrich, M., Wünsche, T., Zarschler, K., Lebeda, O., Pietzsch, J., Pietzsch, H. J., & Walther, M. (2021). Radiolabelled Cyclic Bisarylmercury: High Chemical and in vivo Stability for Theranostics. *ChemMedChem*, *16*(17), 2645–2649.
80. Dale, R. M. K., Martin, E., Livingston, D. C., & Ward, D. C. (1975). Direct covalent mercuration of nucleotides and polynucleotides. *Biochemistry*, *14*(11), 2447-2457.
81. Nehzati, S., Summers, A. O., Dolgova, N. V., Zhu, J., Sokaras, D., Kroll, T., & George, G. N. (2021). Hg (II) binding to thymine bases in DNA. *Inorganic Chemistry*, *60*(10), 7442-7452.
82. Kuklenyik, Z., & Marzilli, L. G. (1996). Mercury (II) site-selective binding to a DNA hairpin. Relationship of sequence-dependent intra-and interstrand cross-linking to the hairpin− duplex conformational transition. *Inorganic chemistry*, *35*(19), 5654-5662.
83. Vicente, J., Abad, J. A., Shaw, K. F., Gil-Rubio, J., Ramírez de Arellano, M. C., & Jones, P. G. (1997). Palladium-Assisted Formation of Carbon− Carbon Bonds. 7.1 Reactions of (2, 3, 4-Trimethoxy-6-X-phenyl) palladium Complexes with Alkynes (X= C (O) NHBut) and Isocyanides (X= C (O) NHBut, C (O) Me, CHO): Crystal and Molecular Structures of [Pd {C6H {C (O) NHBut}-6-(OMe) 3-2, 3, 4}(bpy)](CF3SO3),[Pd {C (CO2Me) C (CO2Me) C6H {C (O) NHBut}-6-(OMe) 3-2, 3, 4)}-Cl (PPh3)],[Pd {C (NXy) C6H {C (O) NHBut}-6-(OMe) 3-2, 3, 4}-(bpy)](CF3SO3), and the Ketenimine 2-(2, 6-Dimethylphenyl)-1-(((2, 6-dimethylphenyl) imino .... *Organometallics*, *16*(21), 4557-4566.
84. Kitching, W., & Glenn, M. (2004). Organometallic Complexes of Mercury. *ChemInform*, *35*(47), no-no.

6. Appendix

Appendix 1.1

^{1}H NMR spectrum of compound 2

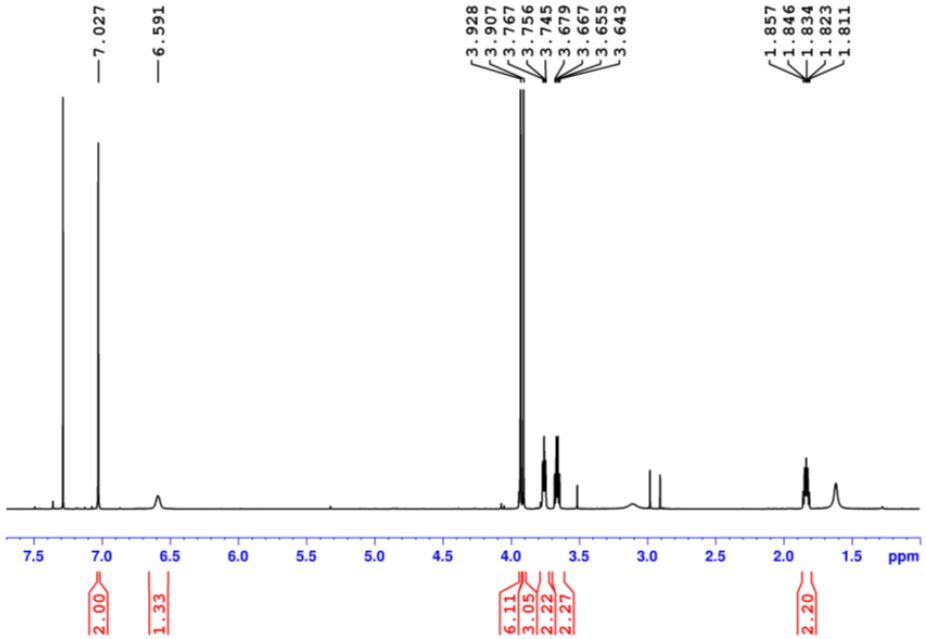

Appendix 2.1

^{1}H NMR spectrum of compound 3

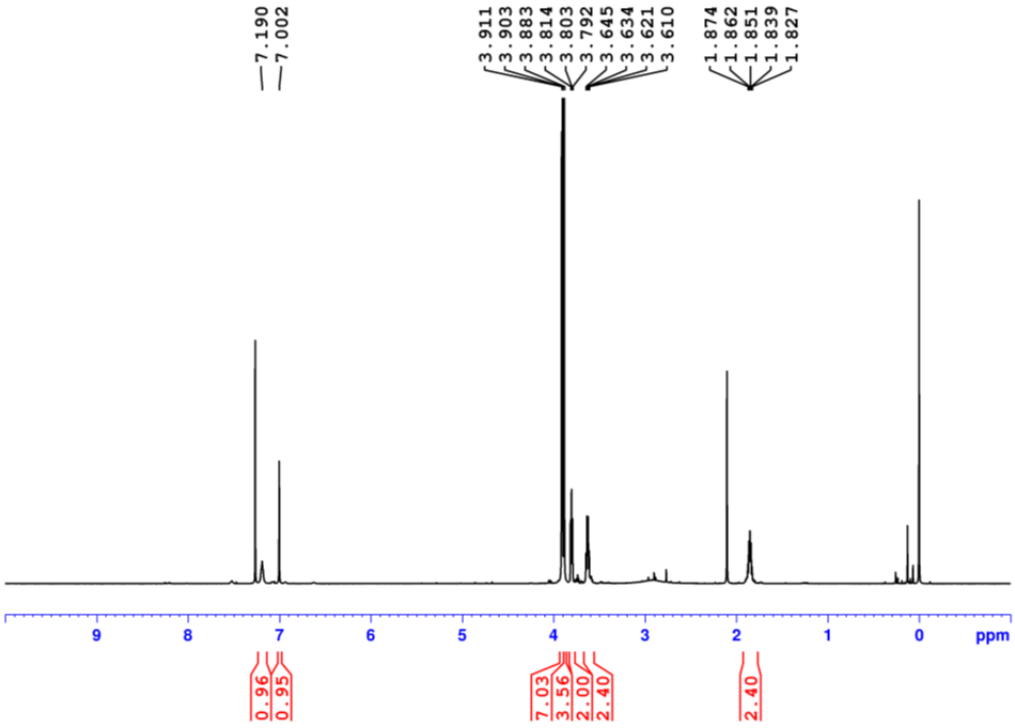

Appendix 2.2

^{1}H NMR spectrum of compound 3

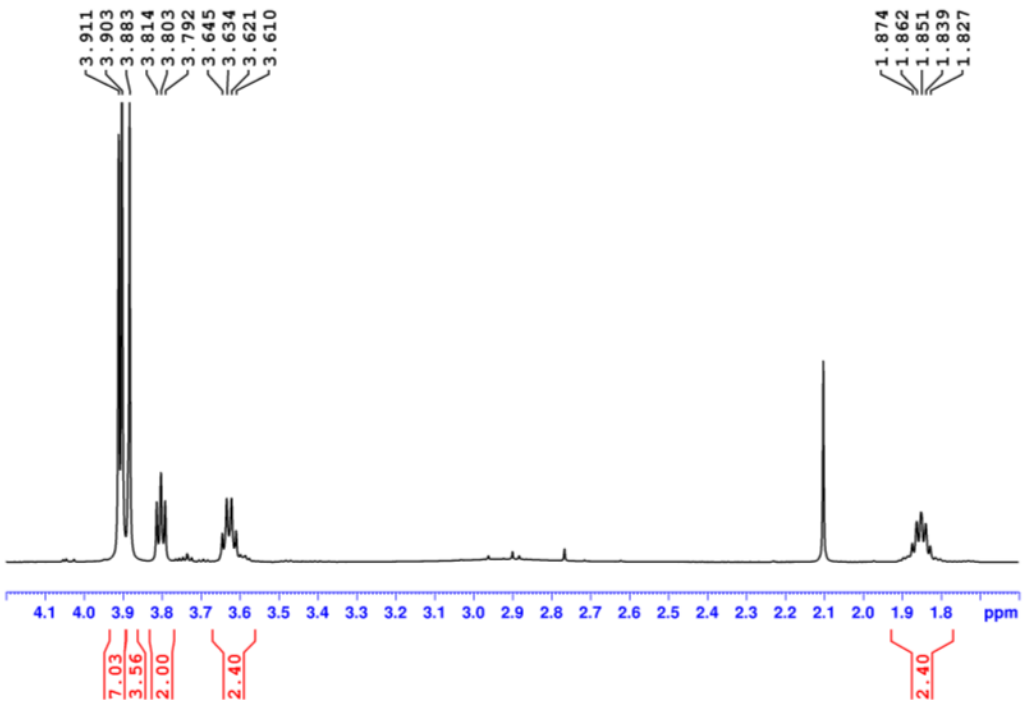

Appendix 2.3

^{13}C NMR spectrum of compound 3

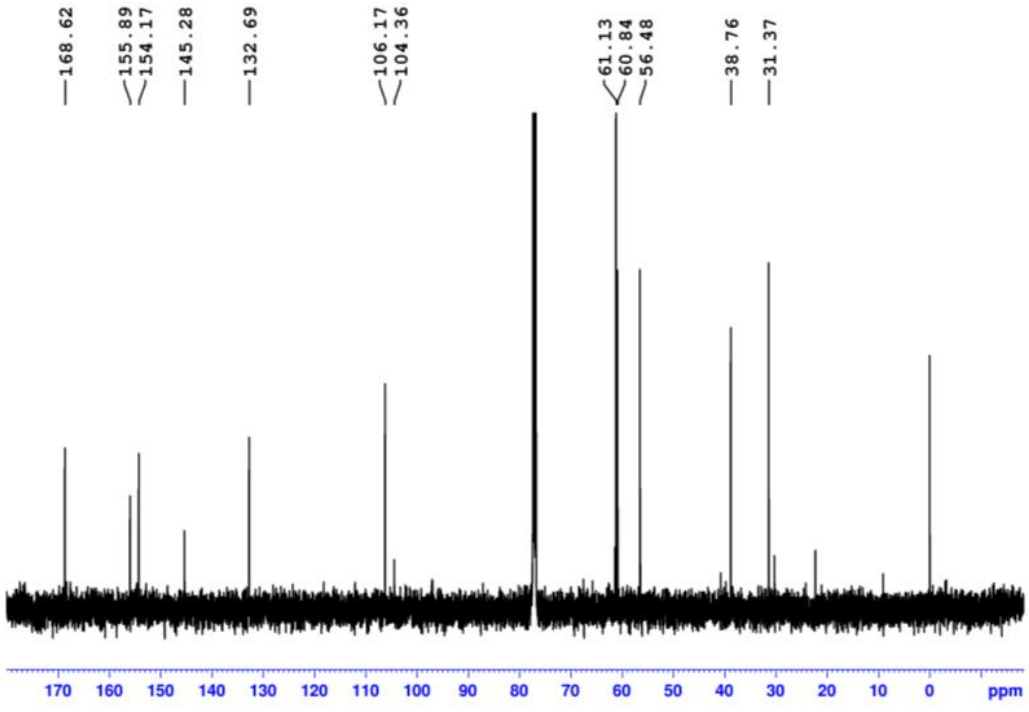

Appendix 3.1

^{1}H NMR spectrum of compound 4

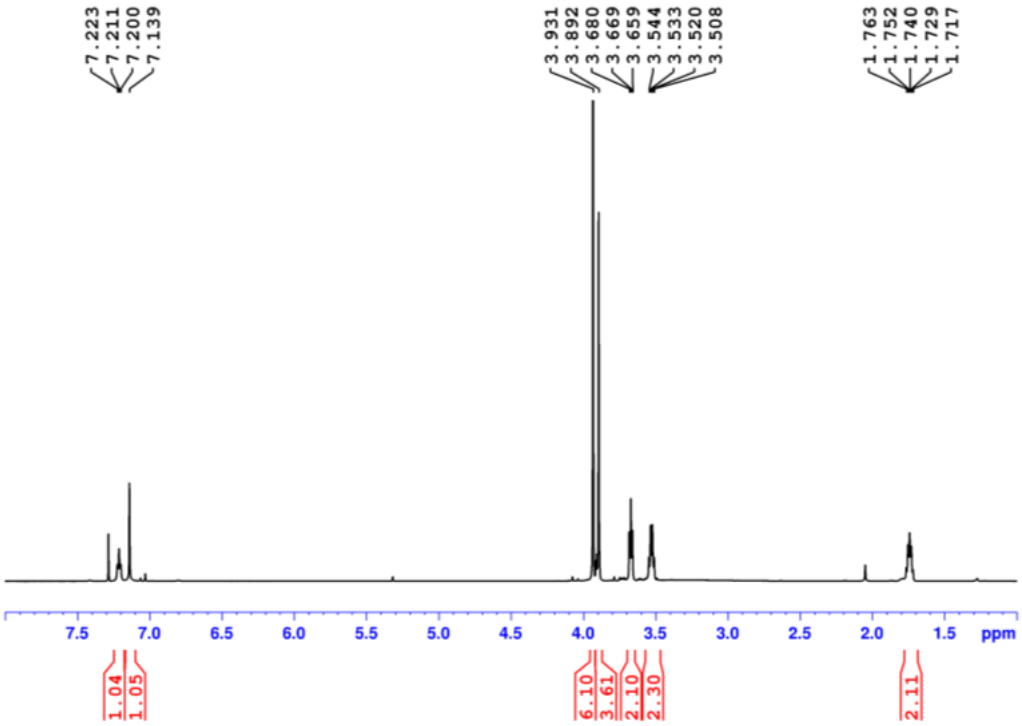

Appendix 3.2

^{13}C NMR spectrum of compound 4

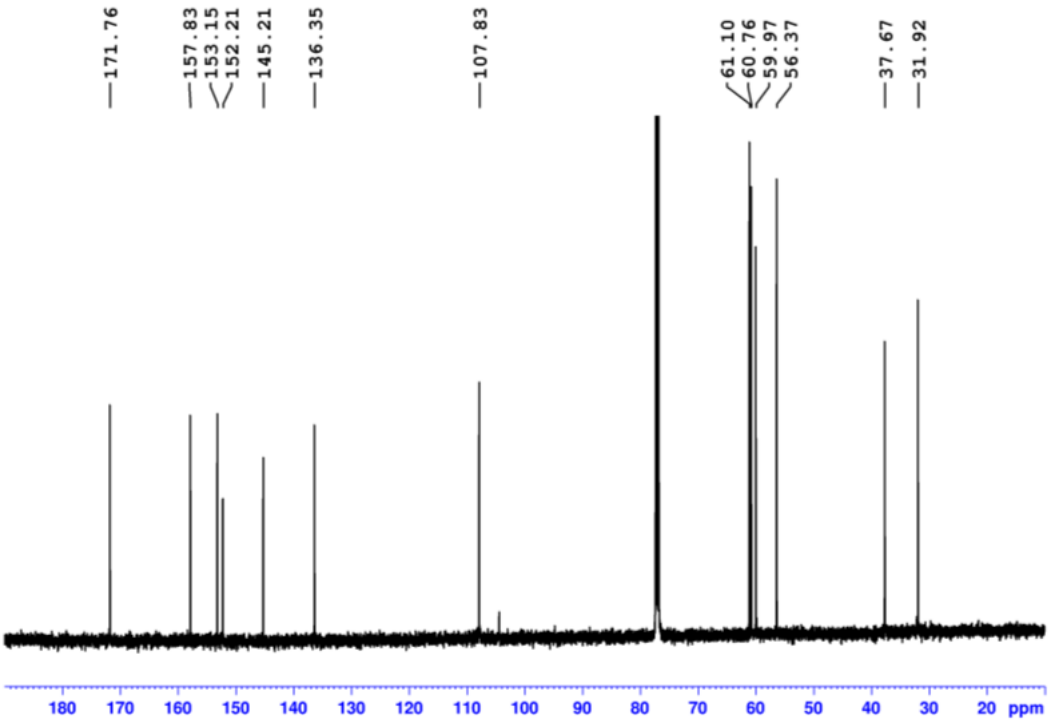

Appendix 4.1

^{1}H NMR spectrum of compound 5

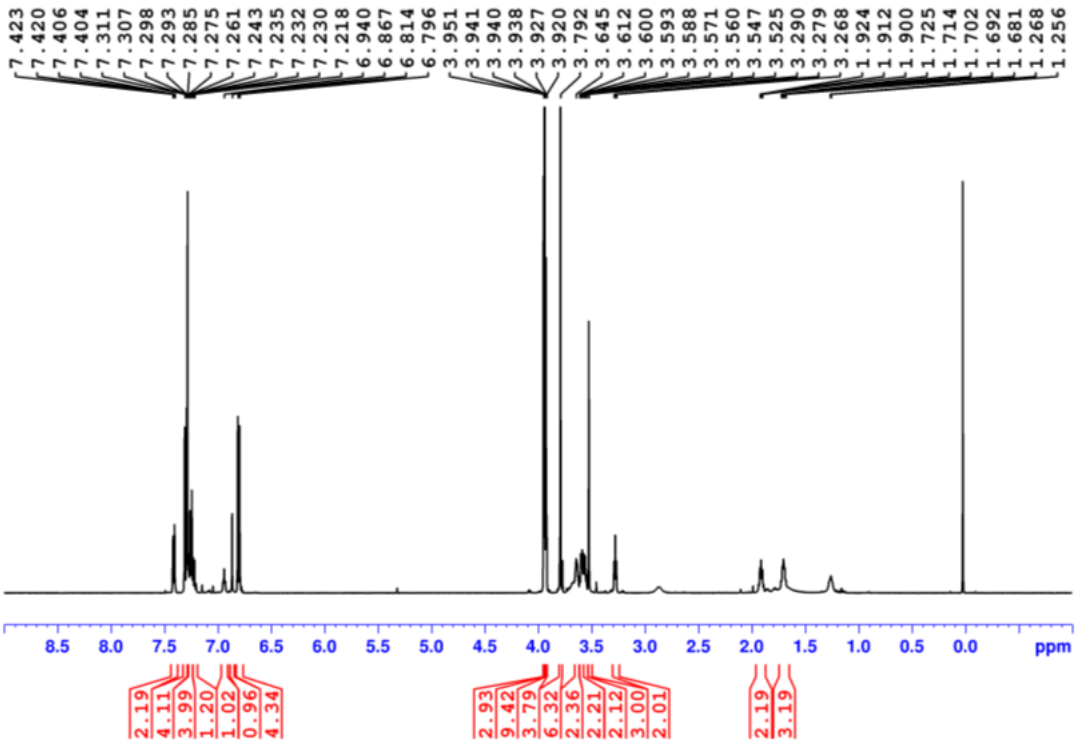

Appendix 4.2

^{1}H NMR spectrum of compound 5

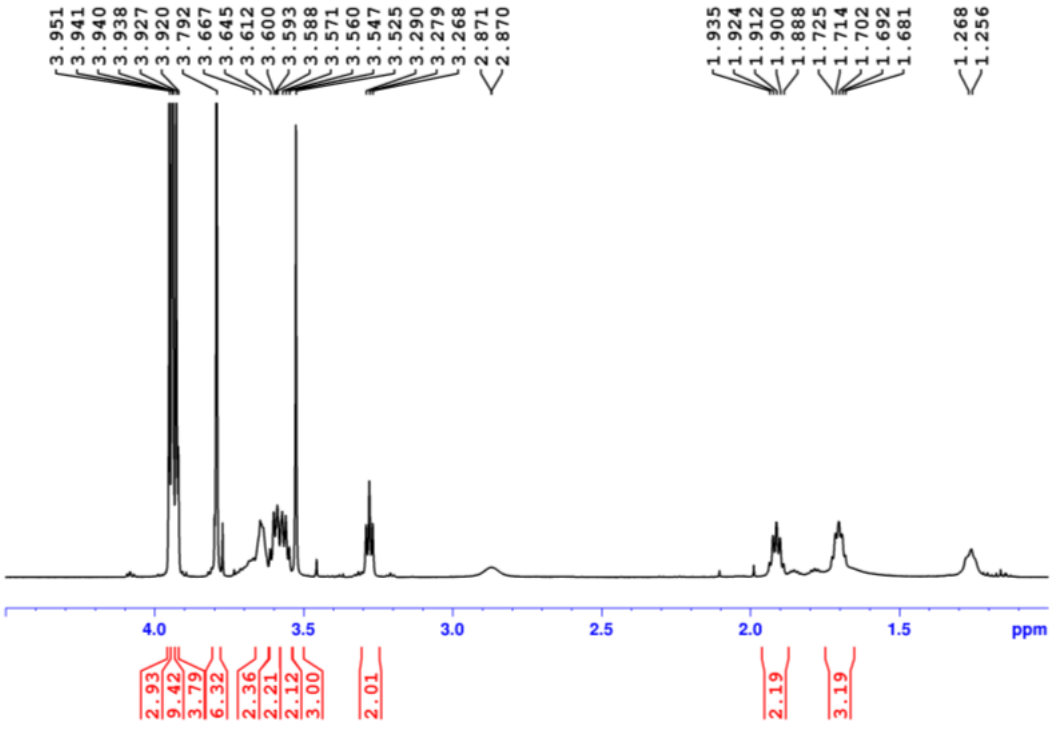

Appendix 4.3

^{1}H NMR spectrum of compound 5

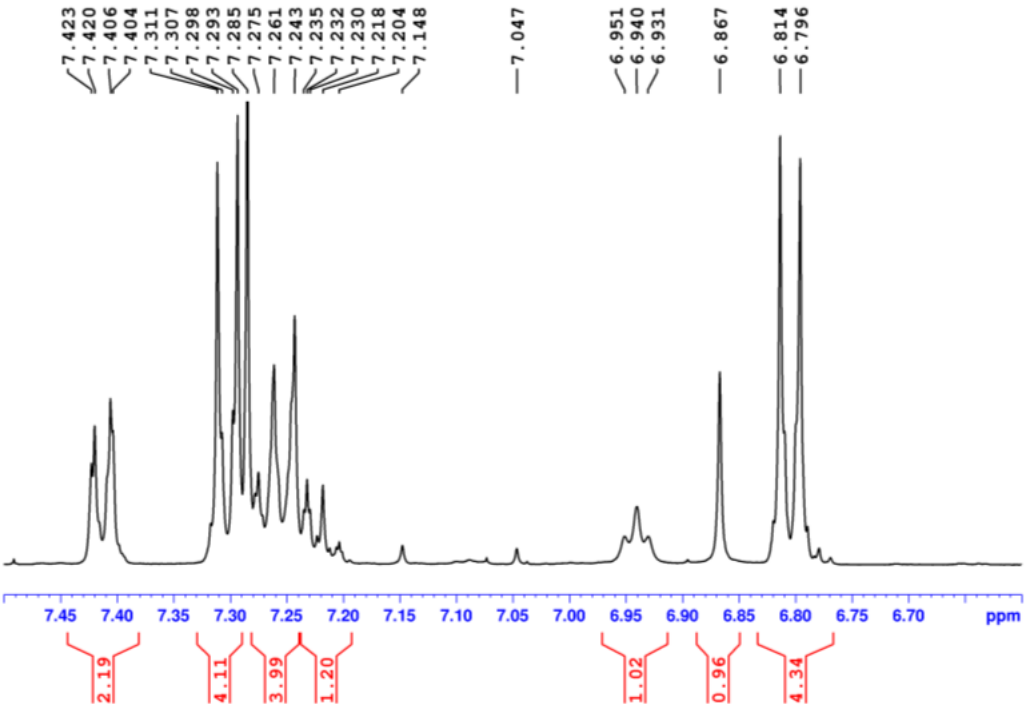

Appendix 4.4

^{13}C NMR spectrum of compound 5

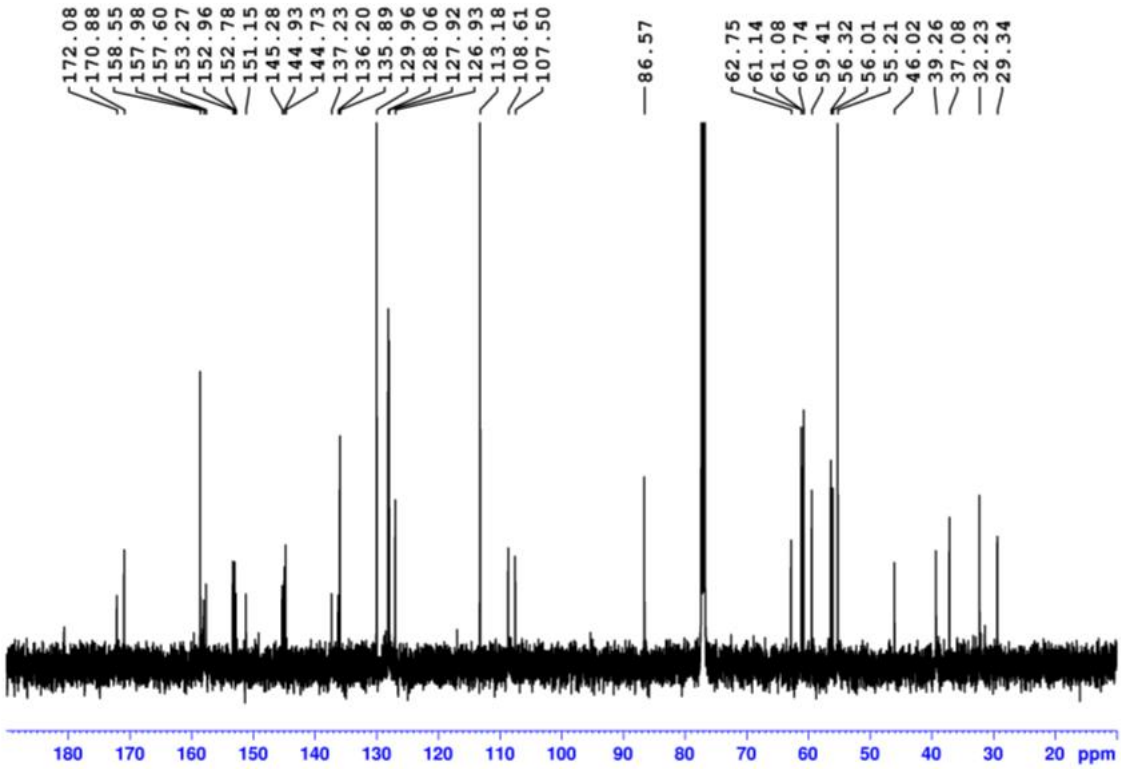

Appendix 5.1

^{1}H NMR spectrum of compound 6

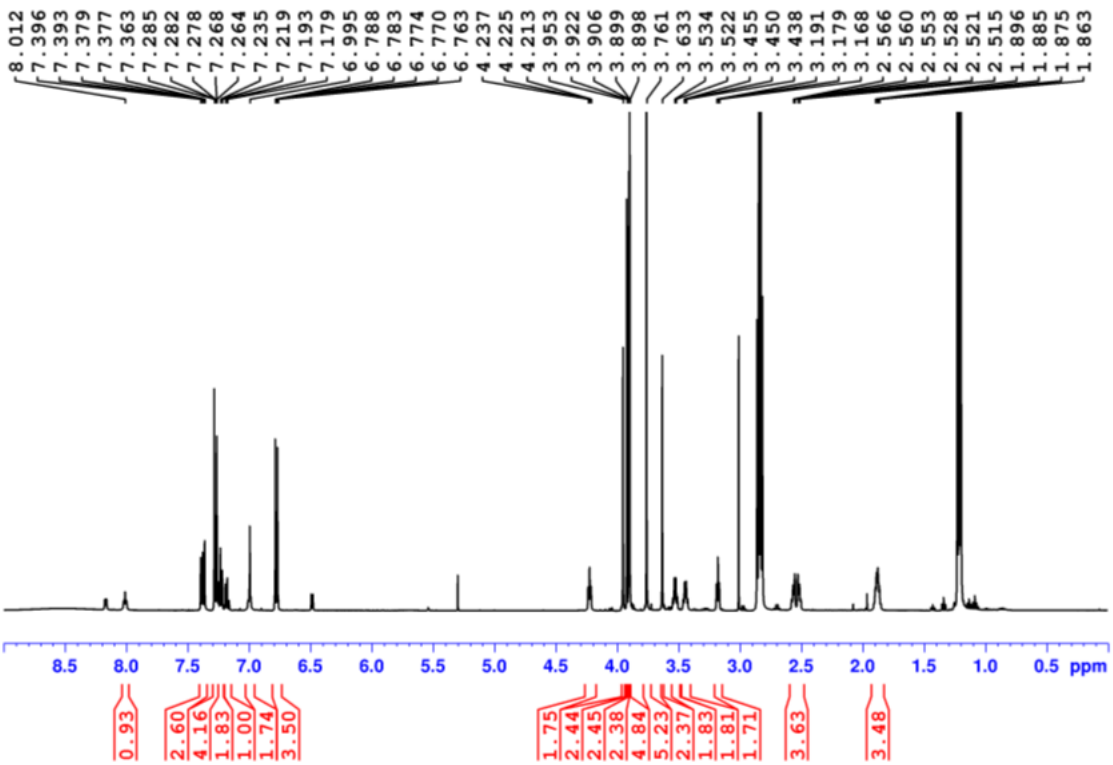

Appendix 5.2

^{1}H NMR spectrum of compound 6

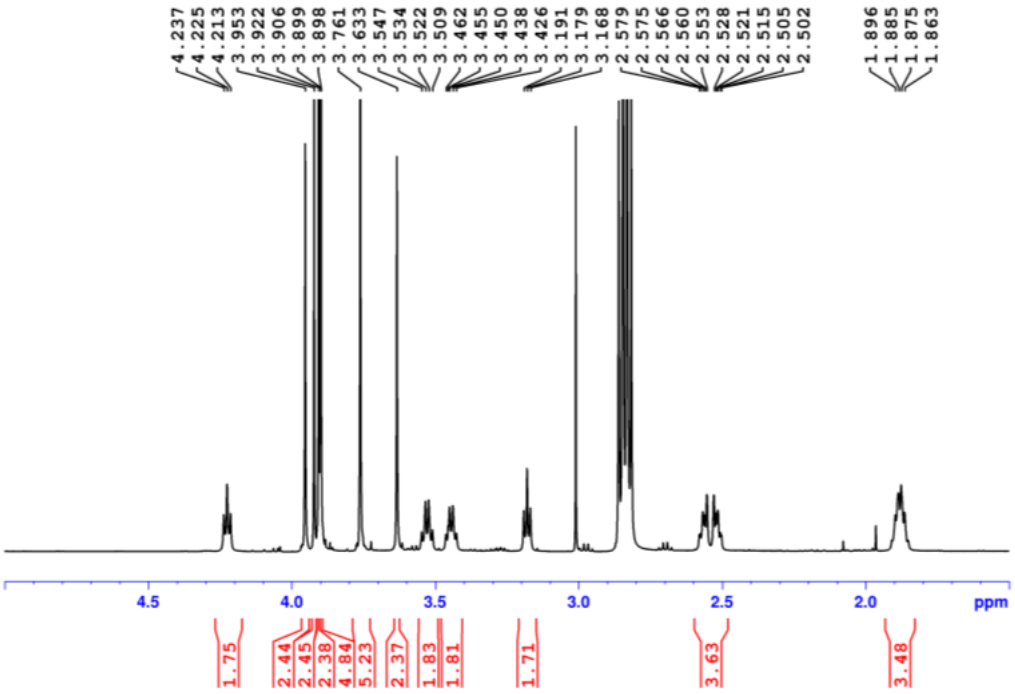

Appendix 5.3

^{1}H NMR spectrum of compound 6

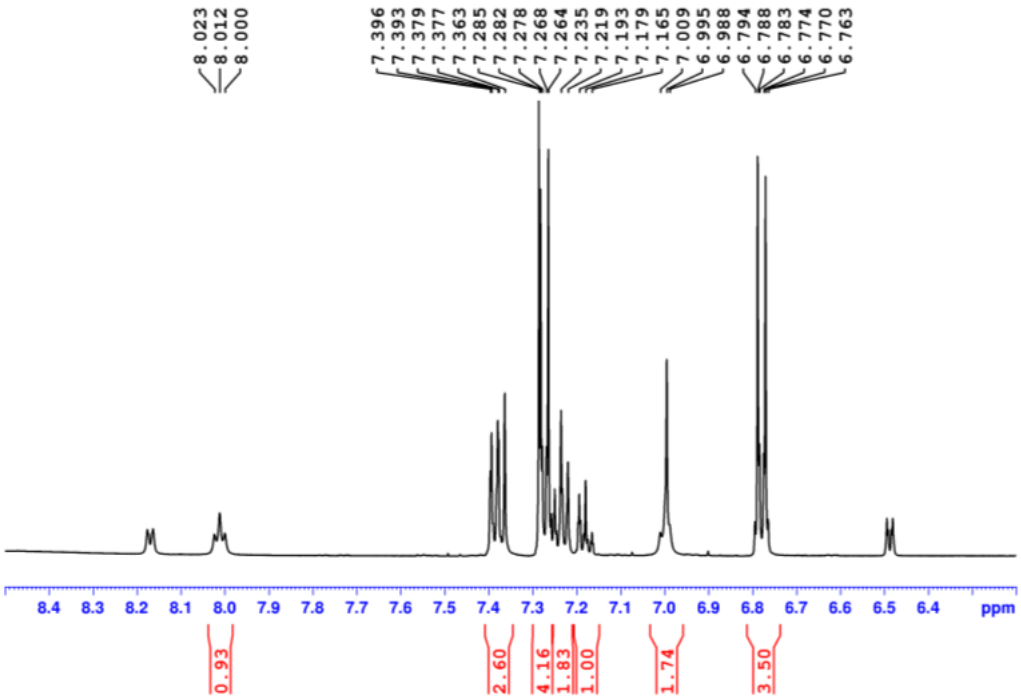

Appendix 5.4

^{13}C NMR spectrum of compound 6

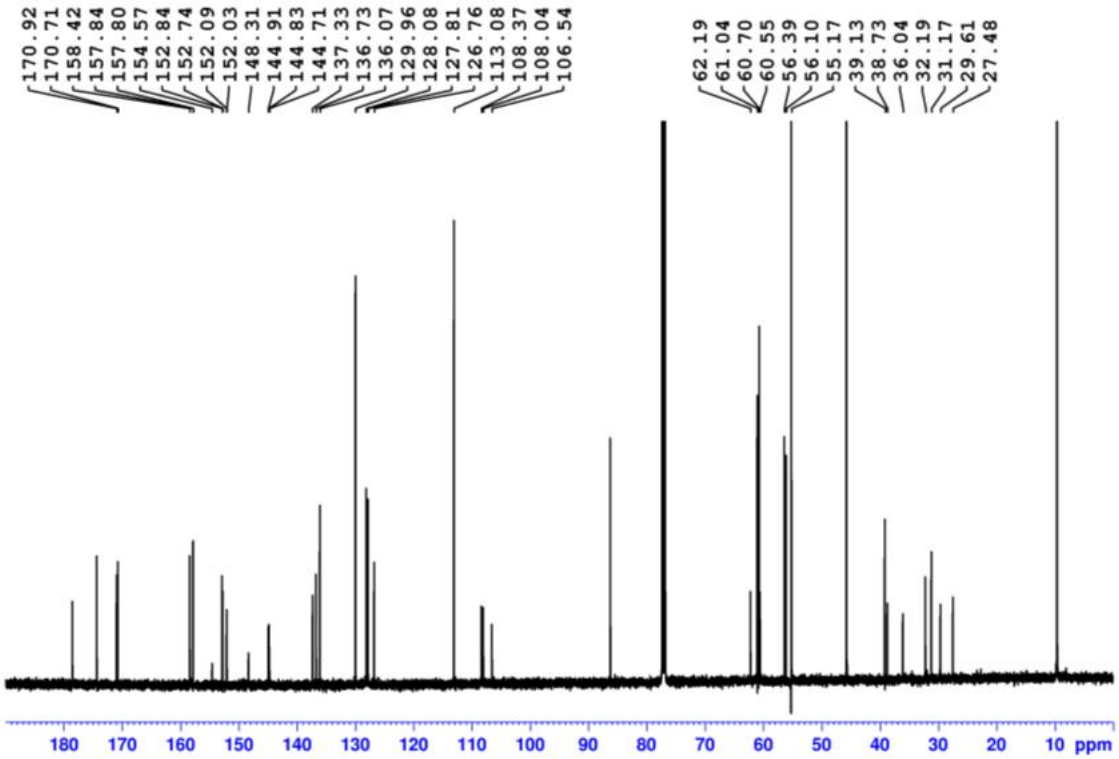

Appendix 6.1

^{1}H NMR spectrum of oxidative test of compound 4 before adding I_2

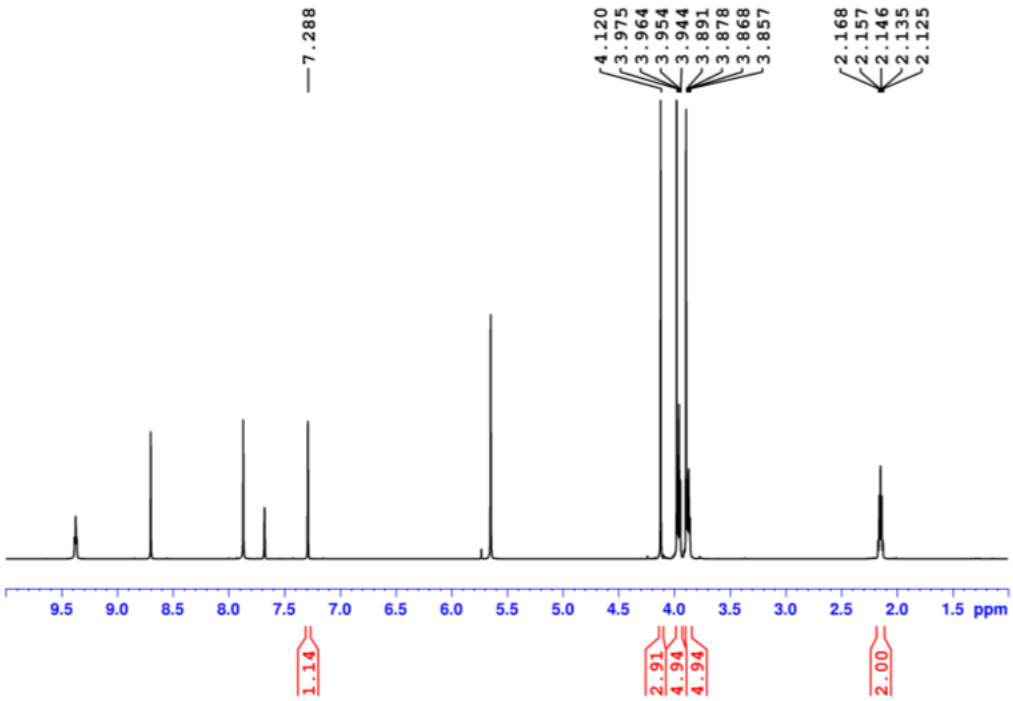

Appendix 6.2

^{1}H NMR spectrum of oxidative test of compound 4 after adding I_2

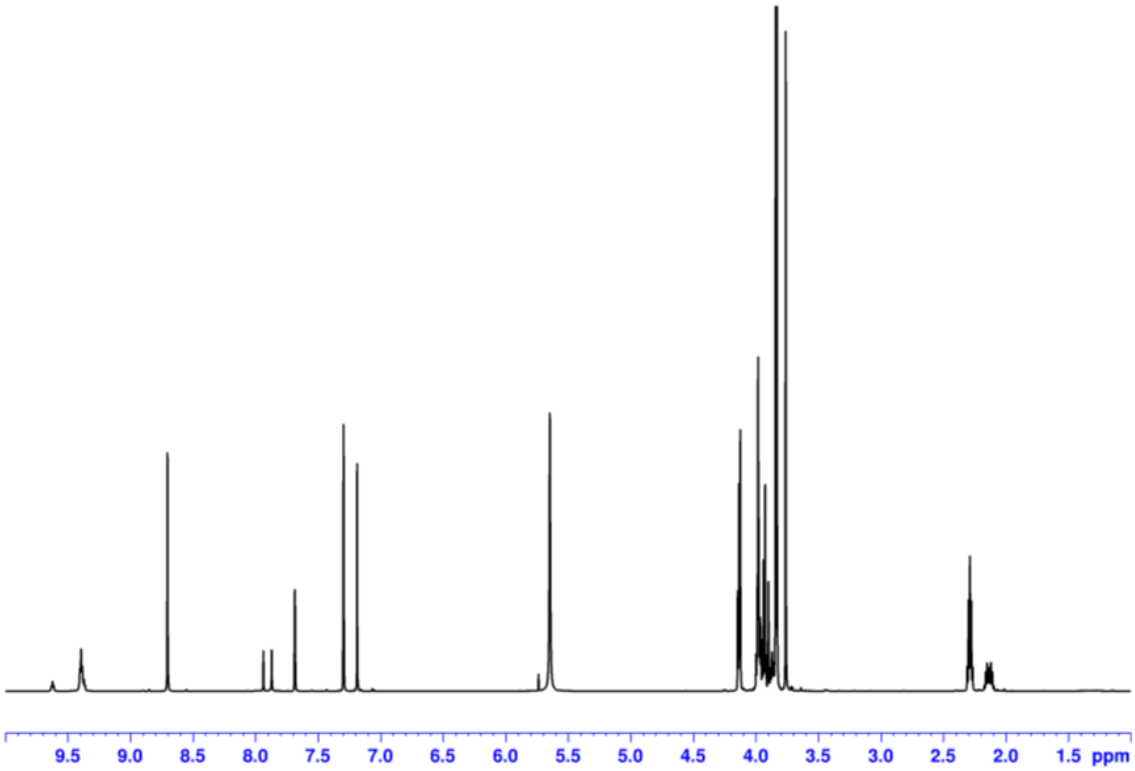

Appendix 6.3

^{1}H NMR spectrum of oxidative test of compound 4 before adding dichloroacetic acid

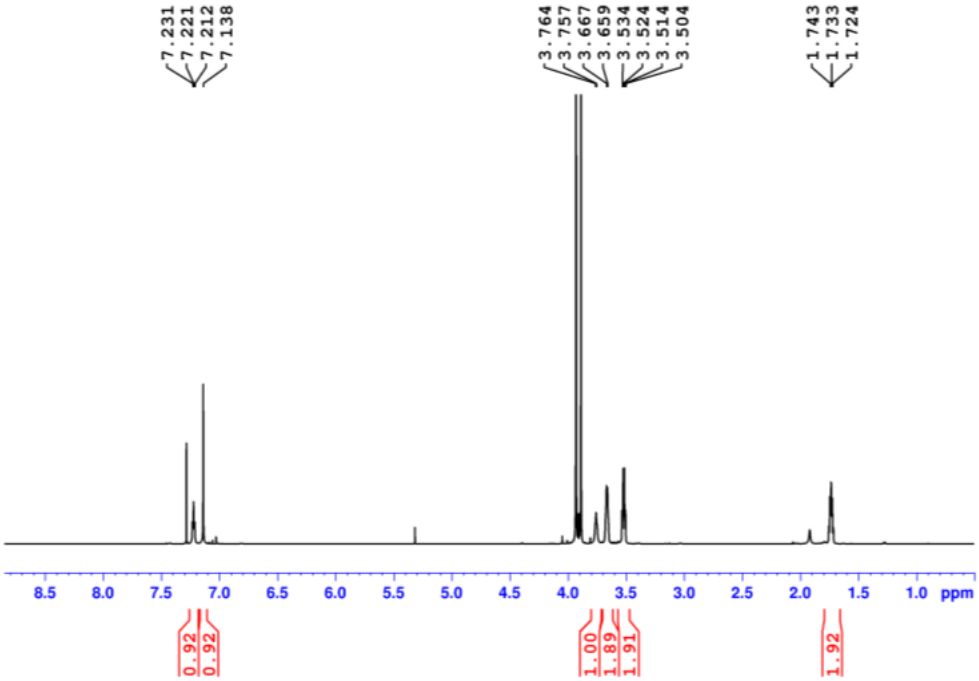

Appendix 6.4

^{1}H NMR spectrum of oxidative test of compound 4 after adding dichloroacetic acid

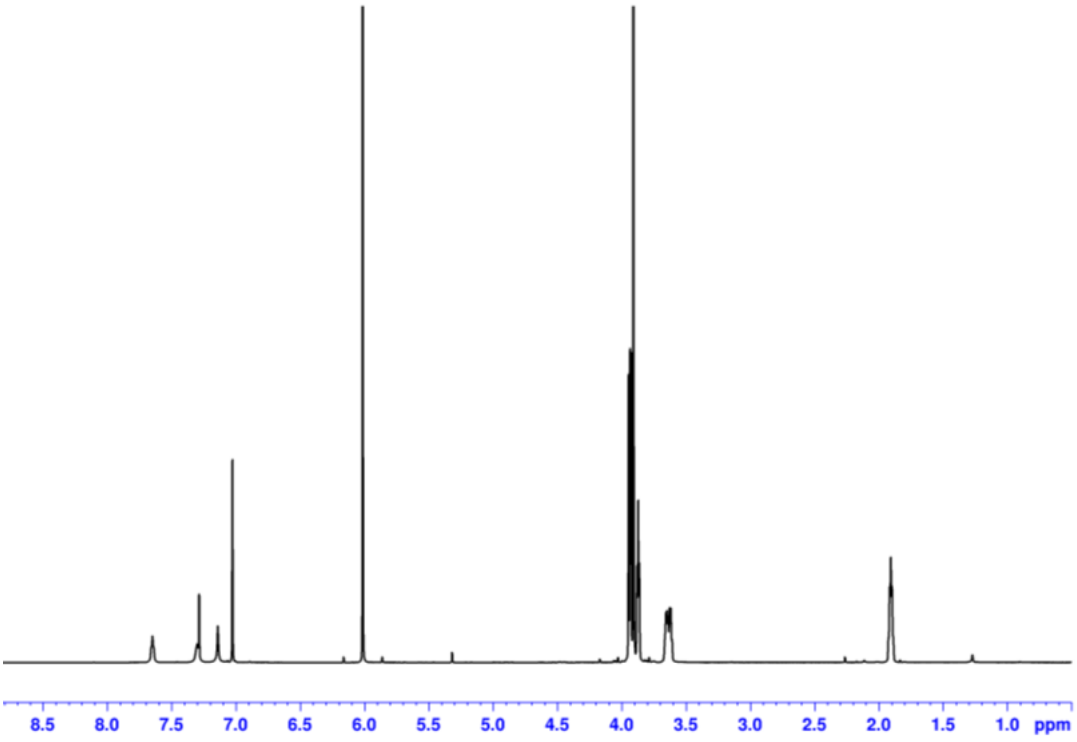

Appendix 7.1

^{1}H NMR spectrum of compound 8

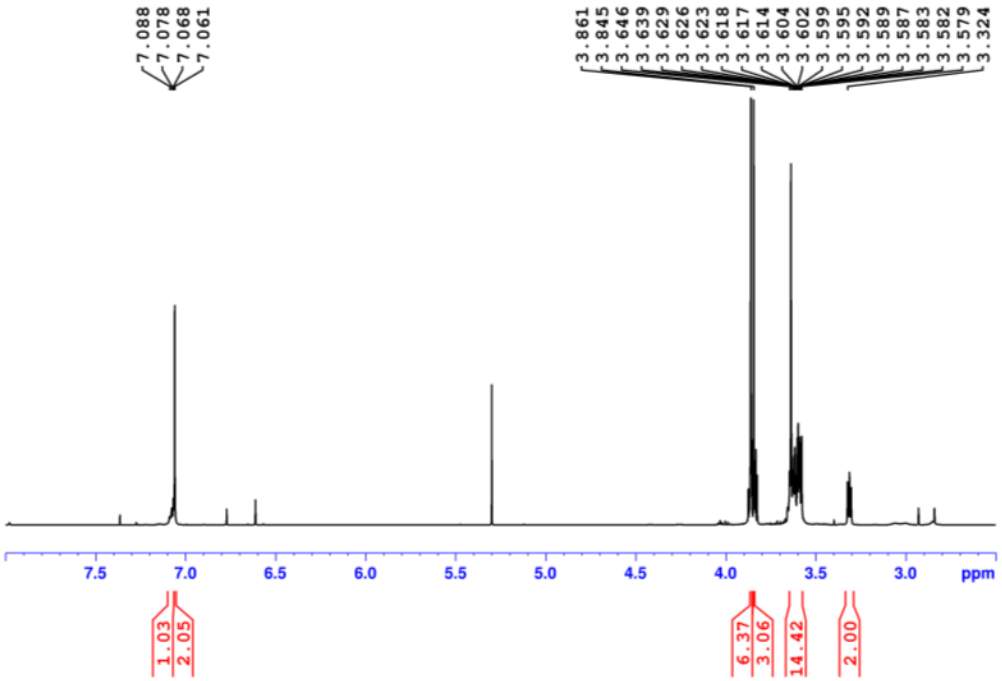

Appendix 7.2

^{1}H NMR spectrum of compound 8

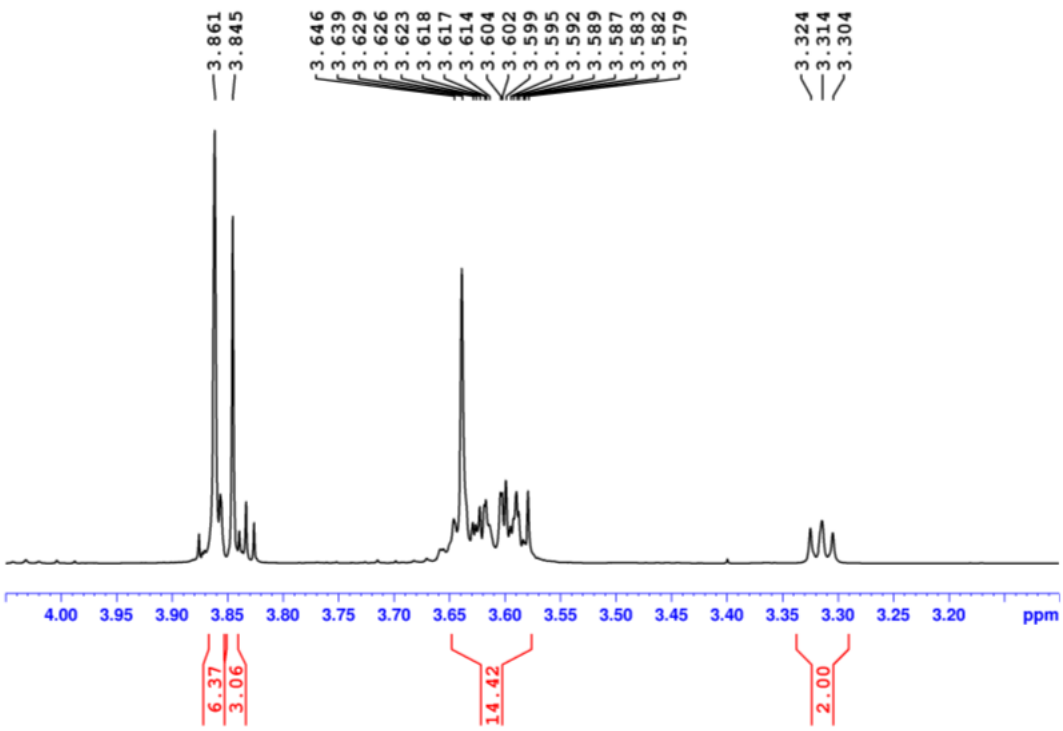

Appendix 7.3

^{1}H NMR spectrum of compound 8

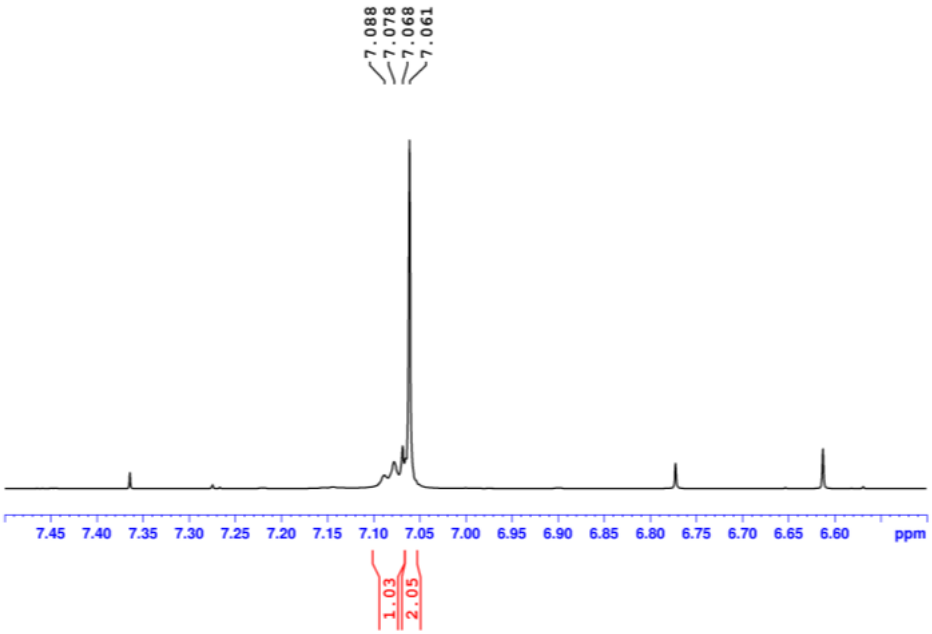

Appendix 7.4

^{13}C NMR spectrum of compound 8

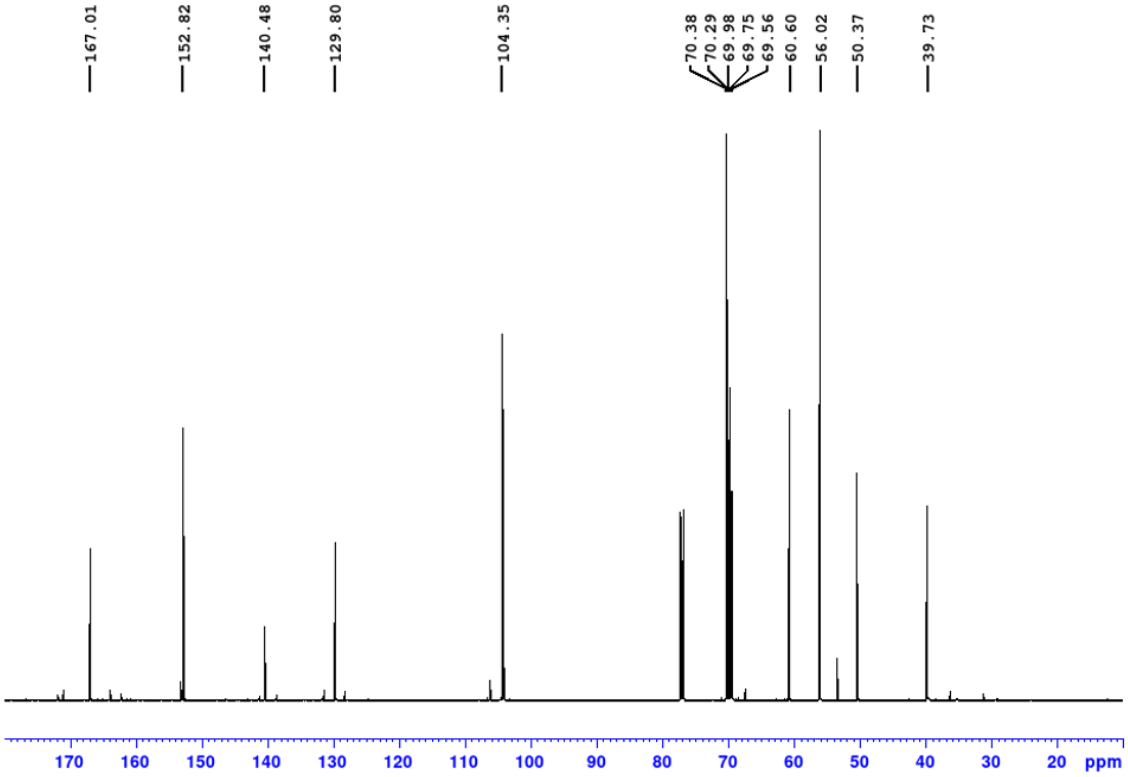

Appendix 7.5

^{13}C NMR spectrum of compound 8

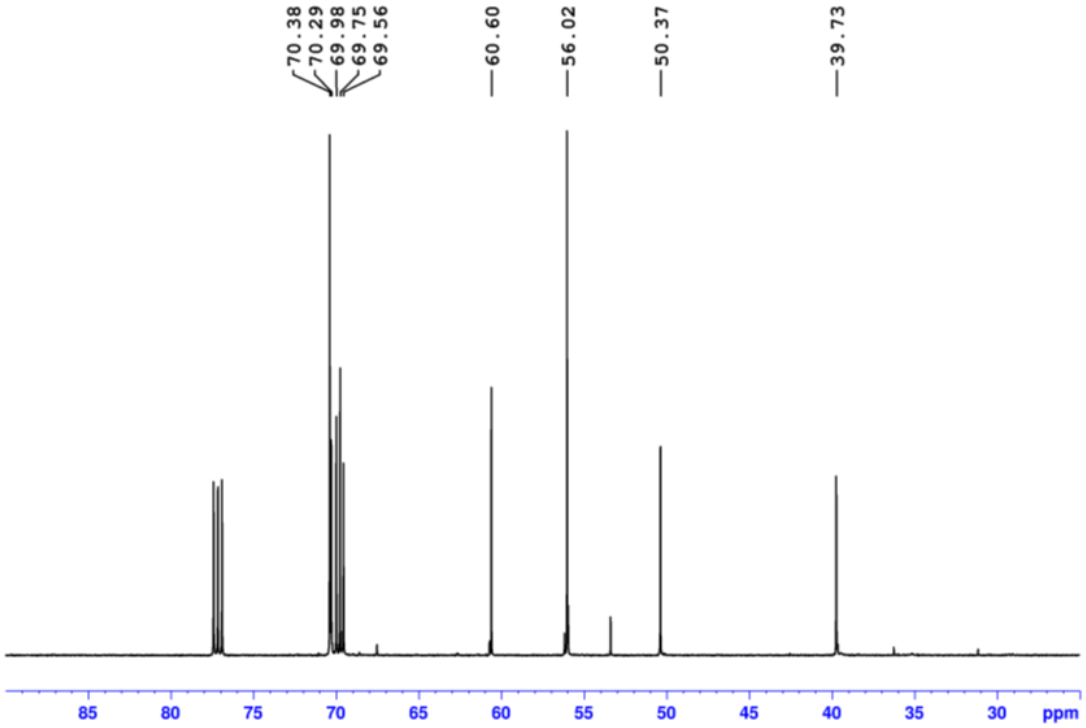

Appendix 8.1

^{1}H NMR spectrum of compound 9

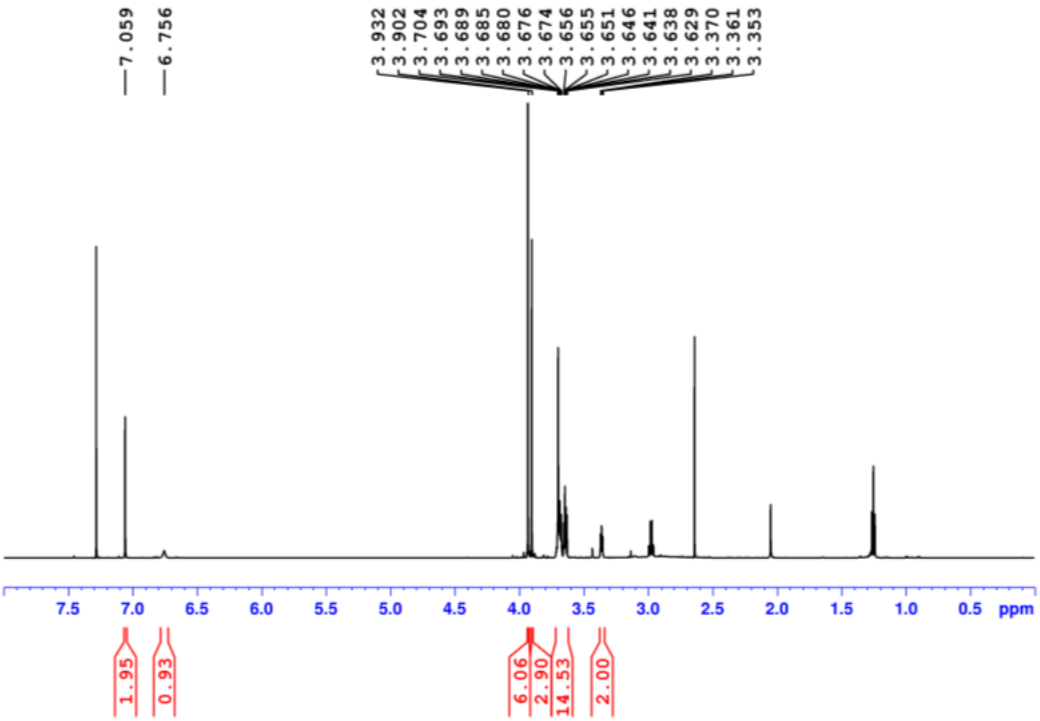

Appendix 8.2

^{1}H NMR spectrum of compound 9

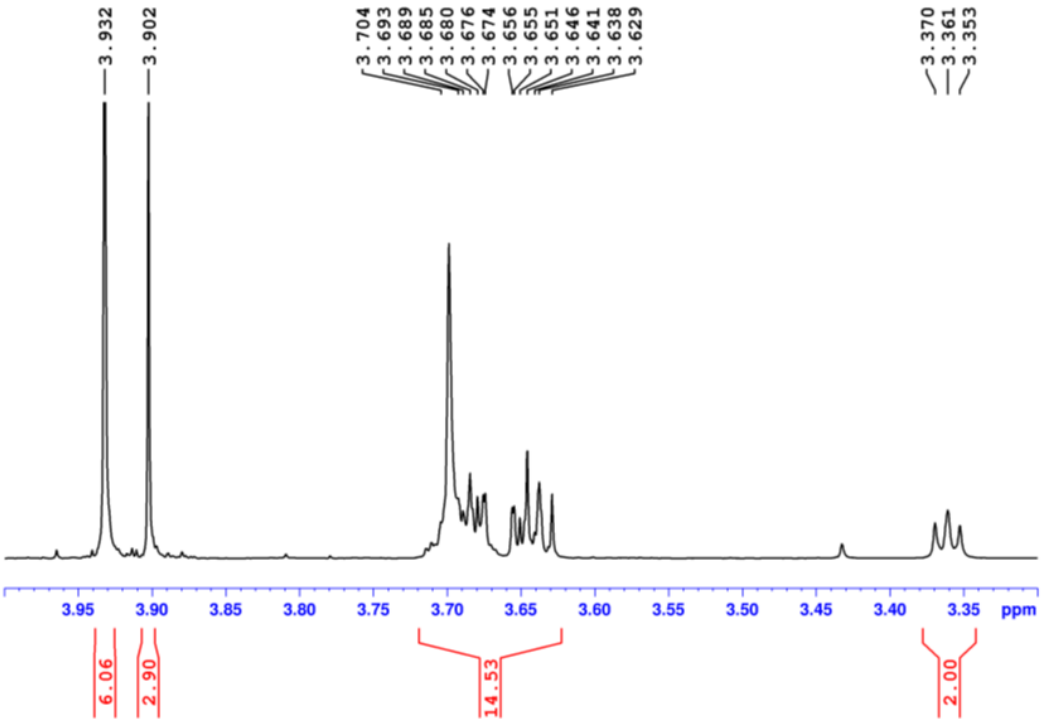

Appendix 8.3

^{1}H NMR spectrum of compound 9

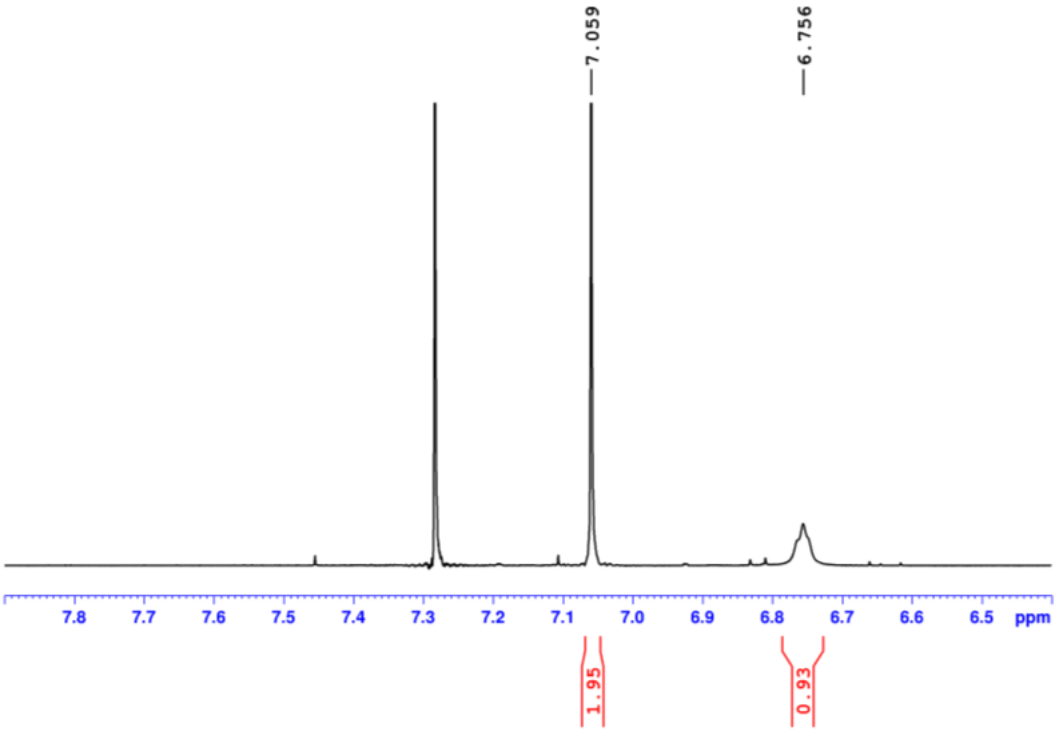

Appendix 9.1

^{1}H NMR spectrum of compound 10

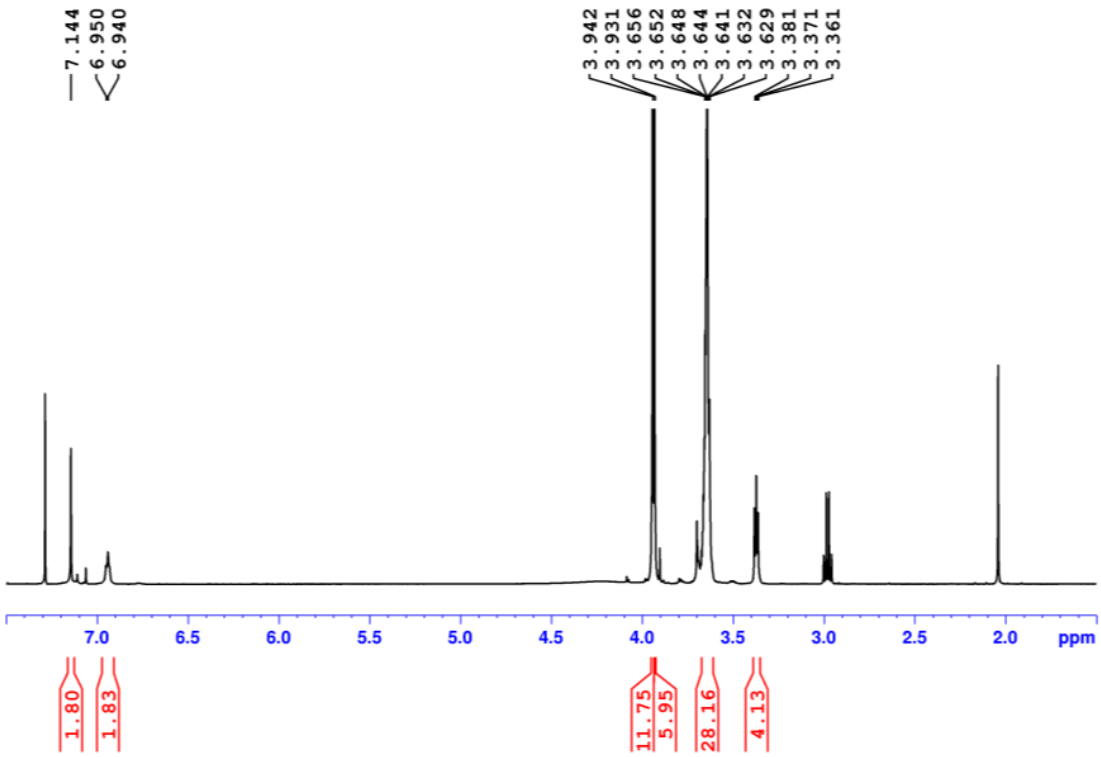

Appendix 9.2

^{1}H NMR spectrum of compound 10

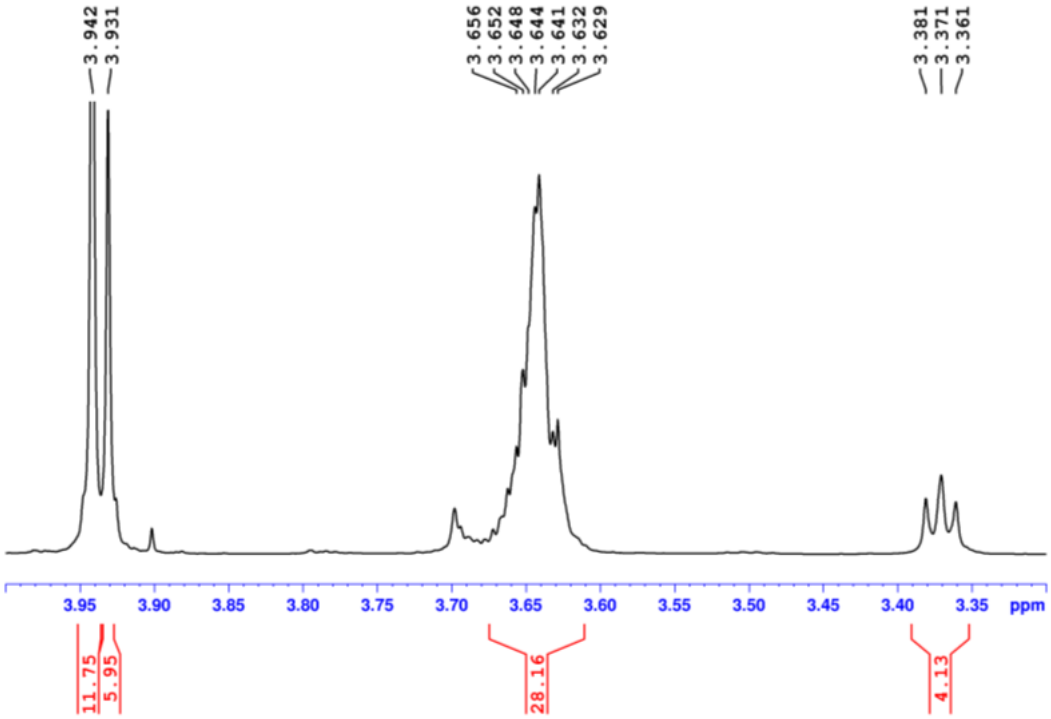

Appendix 9.3

^{1}H NMR spectrum of compound 10

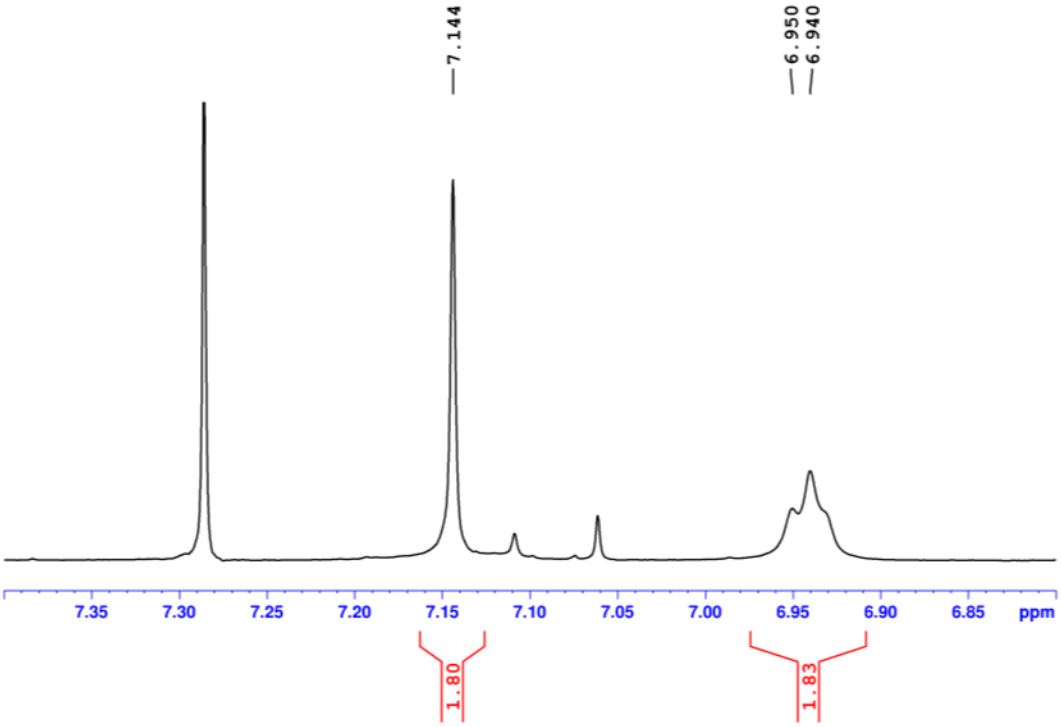

Appendix 9.4

^{13}C NMR spectrum of compound 10

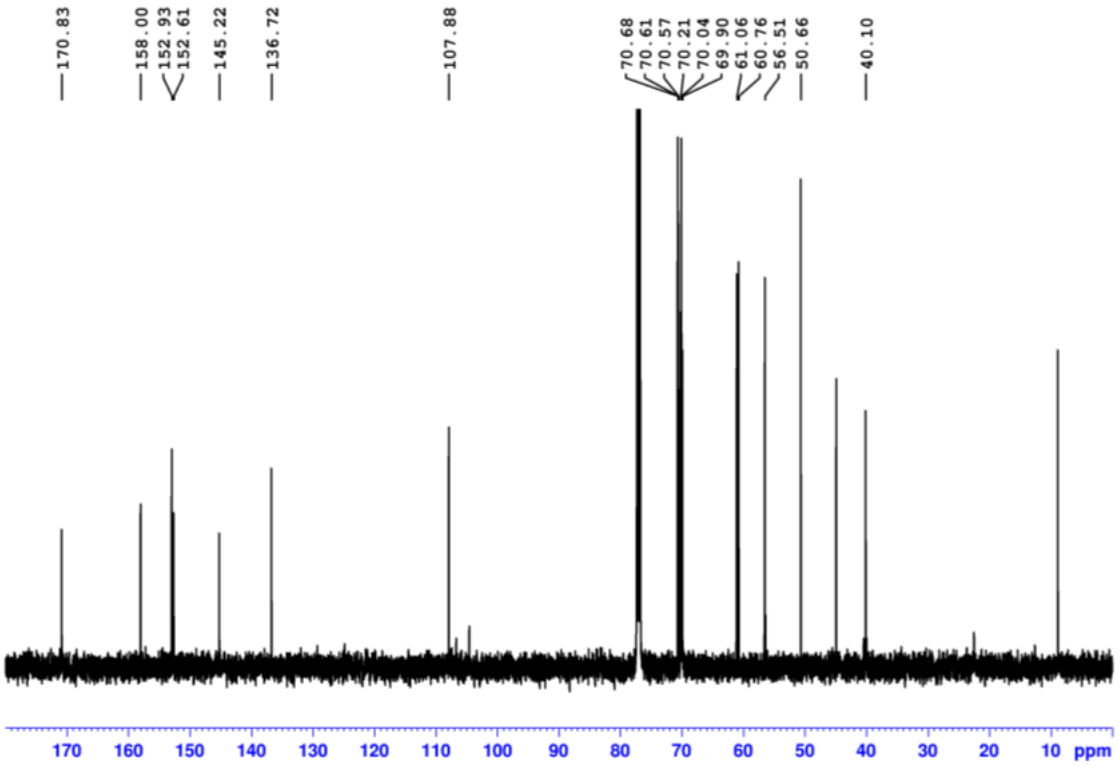

Appendix 9.5

^{13}C NMR spectrum of compound 10

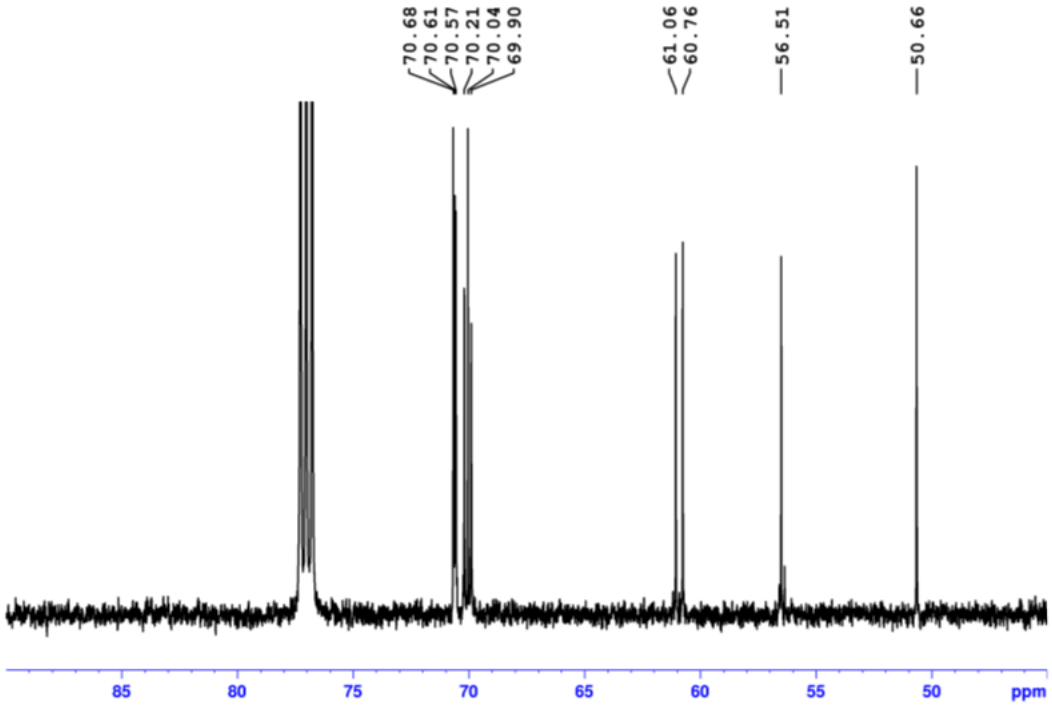

Appendix 9.6

^{13}C NMR spectrum of compound 10

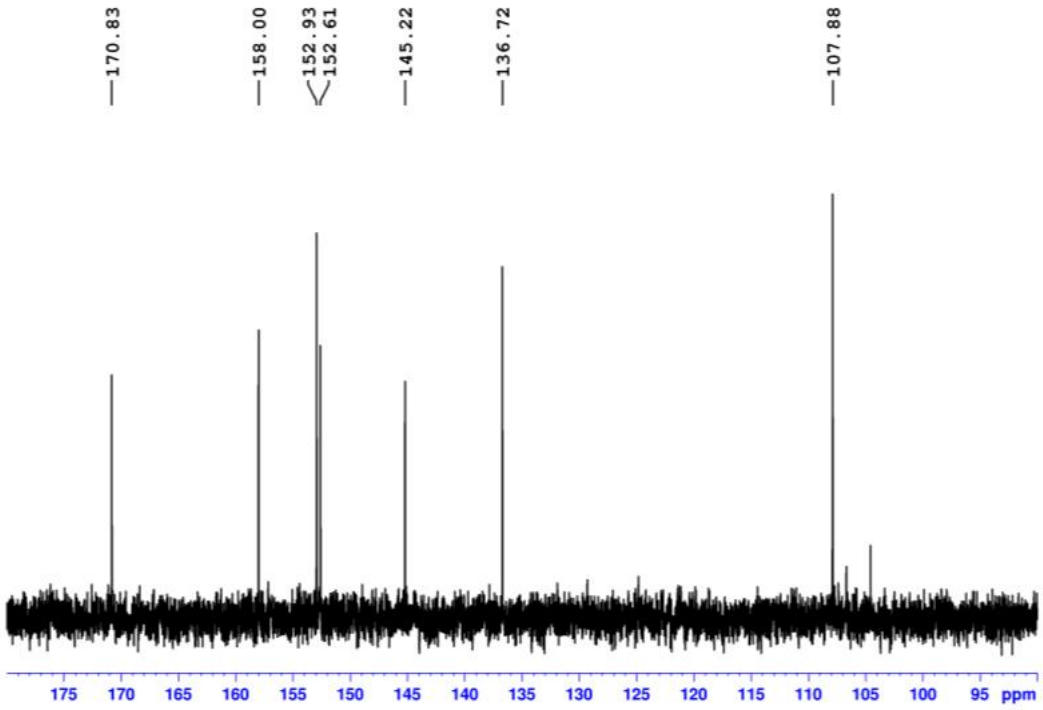

Appendix 10

UPLC-HRMS spectrum of compound 2

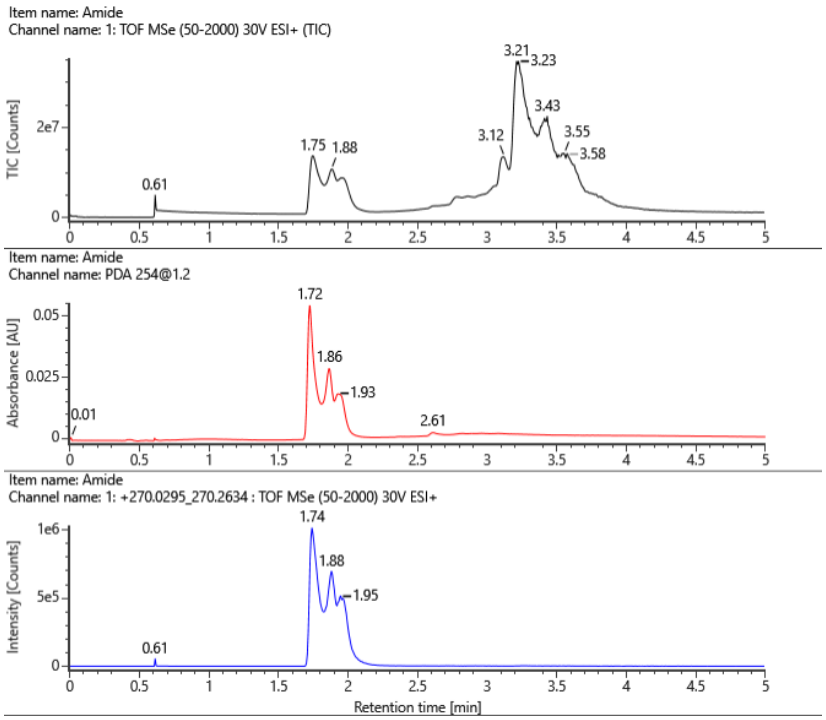

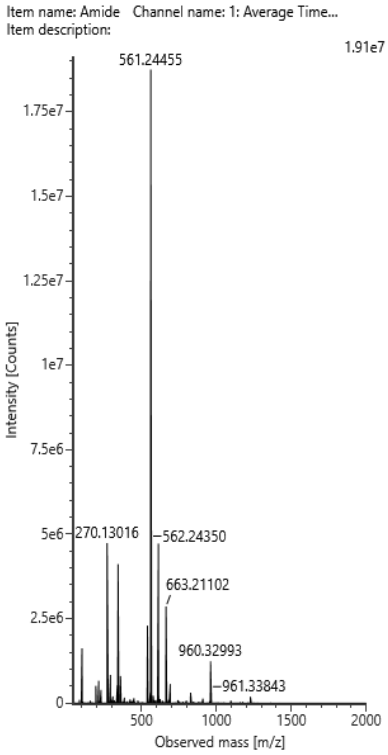

Appendix 11

UPLC-HRMS spectrum of compound 3

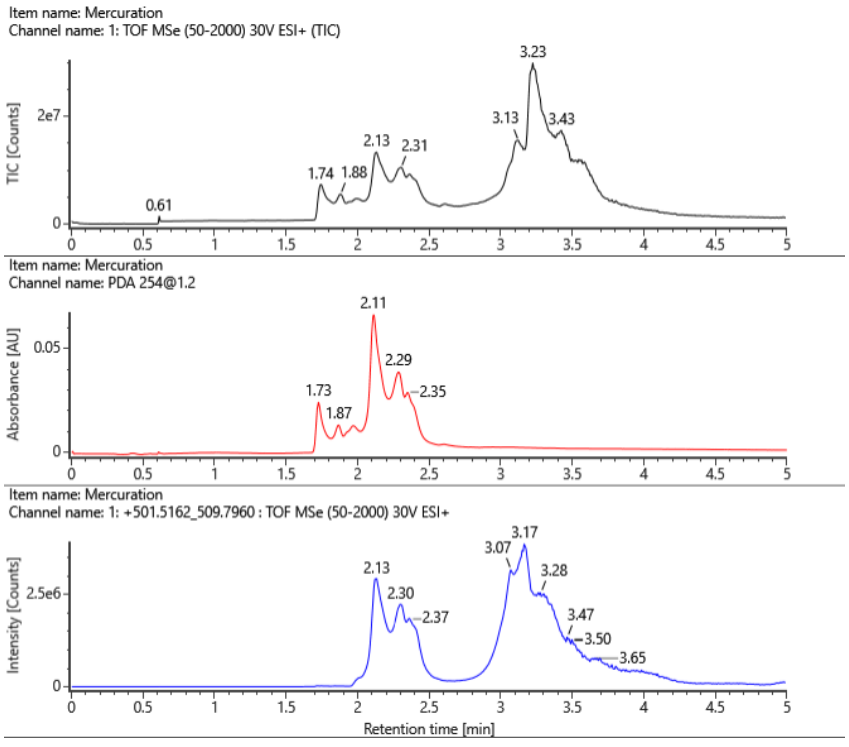

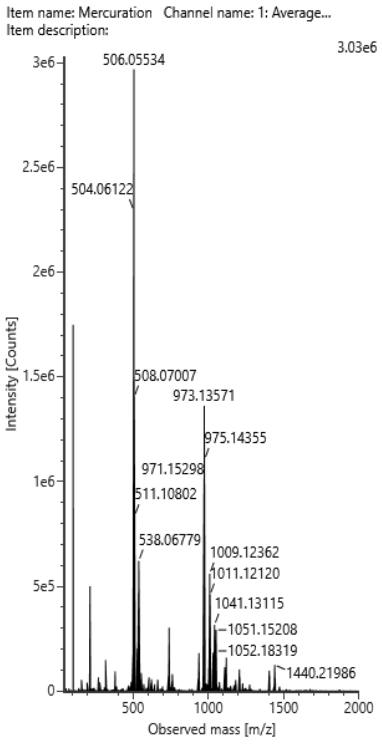

Appendix 12

UPLC-HRMS spectrum of compound 4

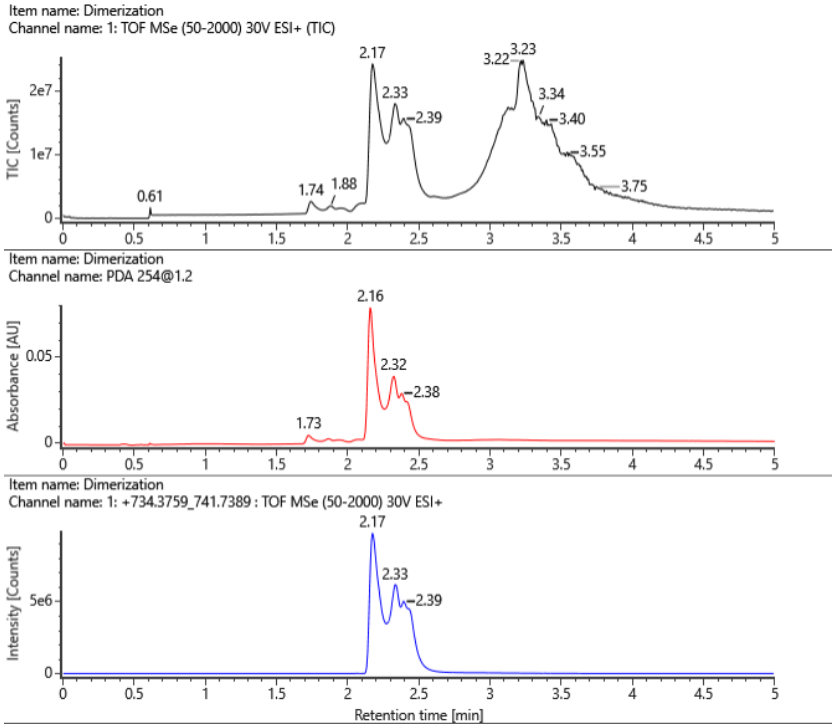

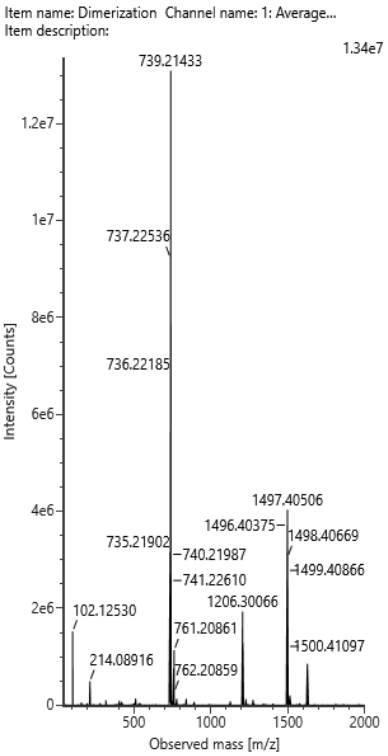

Appendix 13

UPLC-HRMS spectrum of compound 5

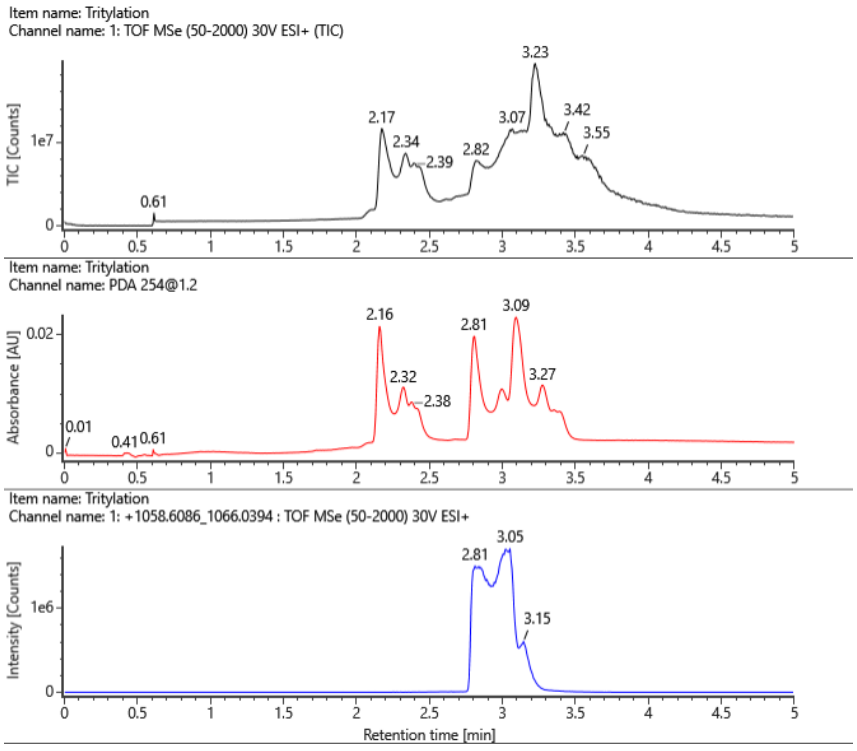

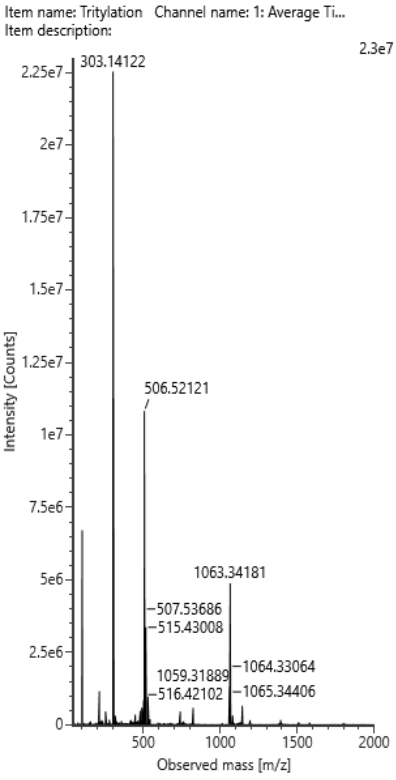

Appendix 14

UPLC-HRMS spectrum of compound 8

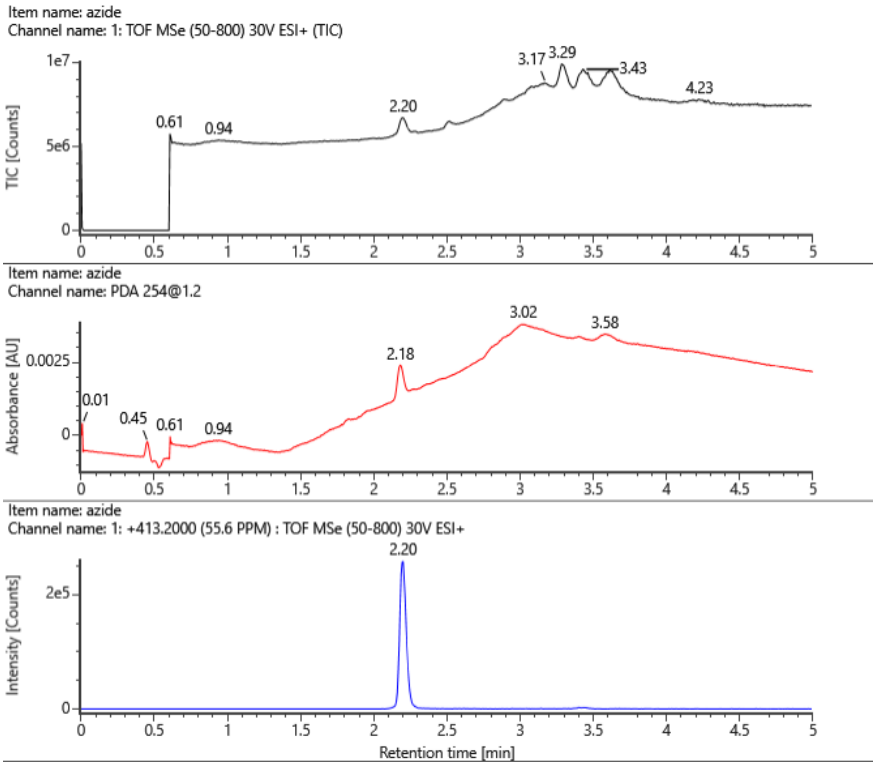

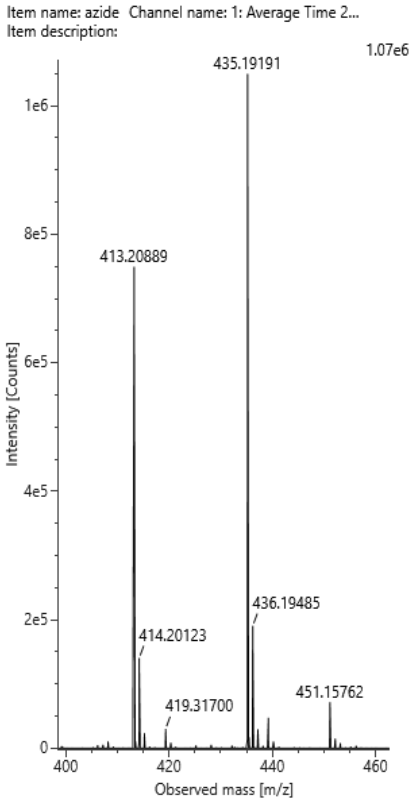

Appendix 15.1

UPLC-HRMS spectrum of compound 10

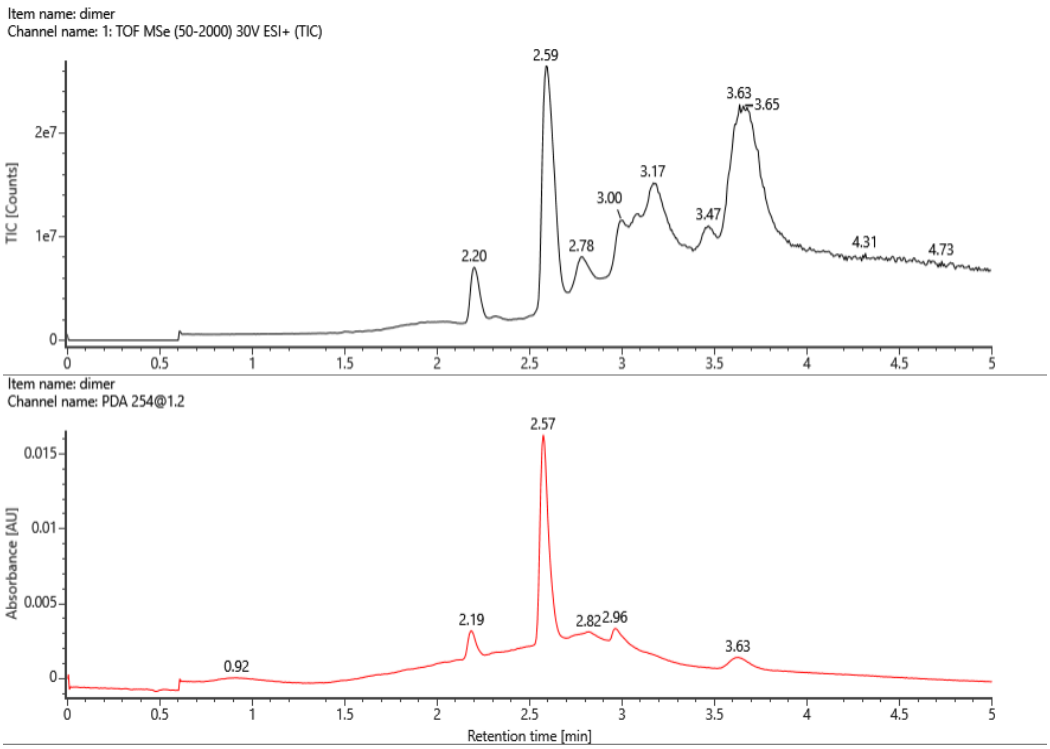

Appendix 15.2

UPLC-HRMS spectrum of compound 10

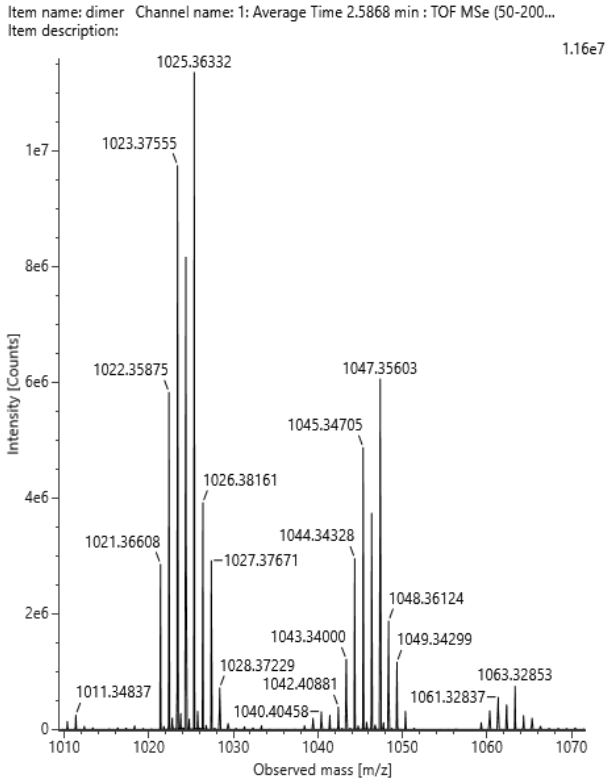

Appendix 16

UPLC-HRMS spectrum of ON1 after RP-HPLC purification

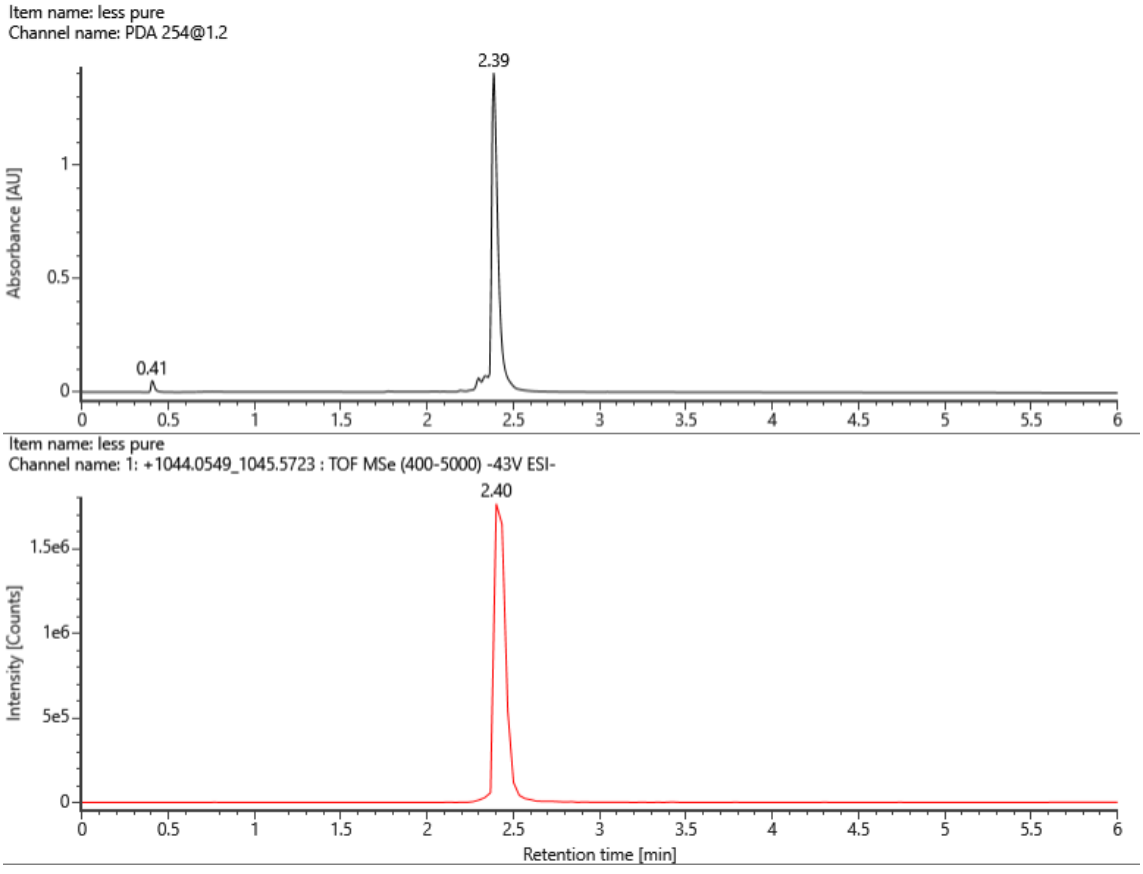

Appendix 17

UPLC-HRMS spectrum of ON1 after RP-HPLC purification

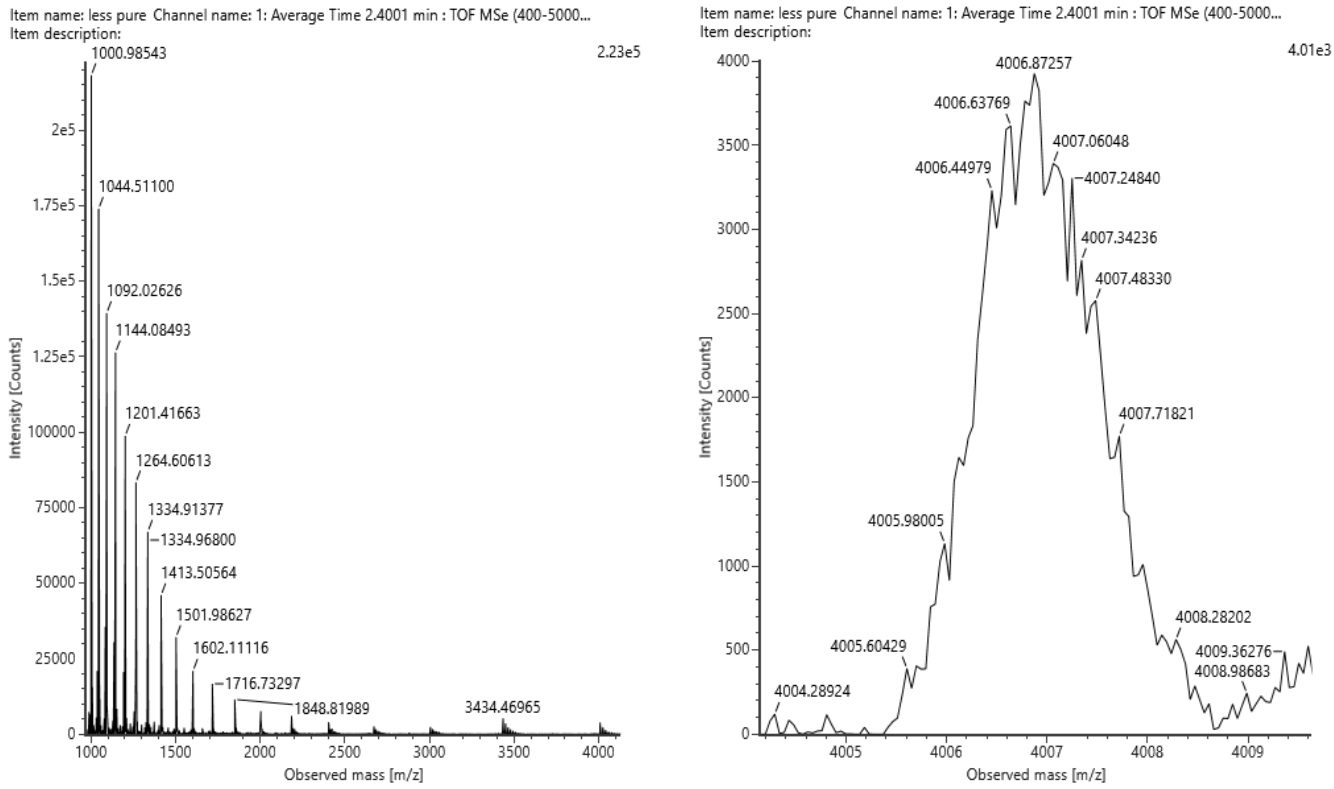

Appendix 18

UV spectrum of ON1

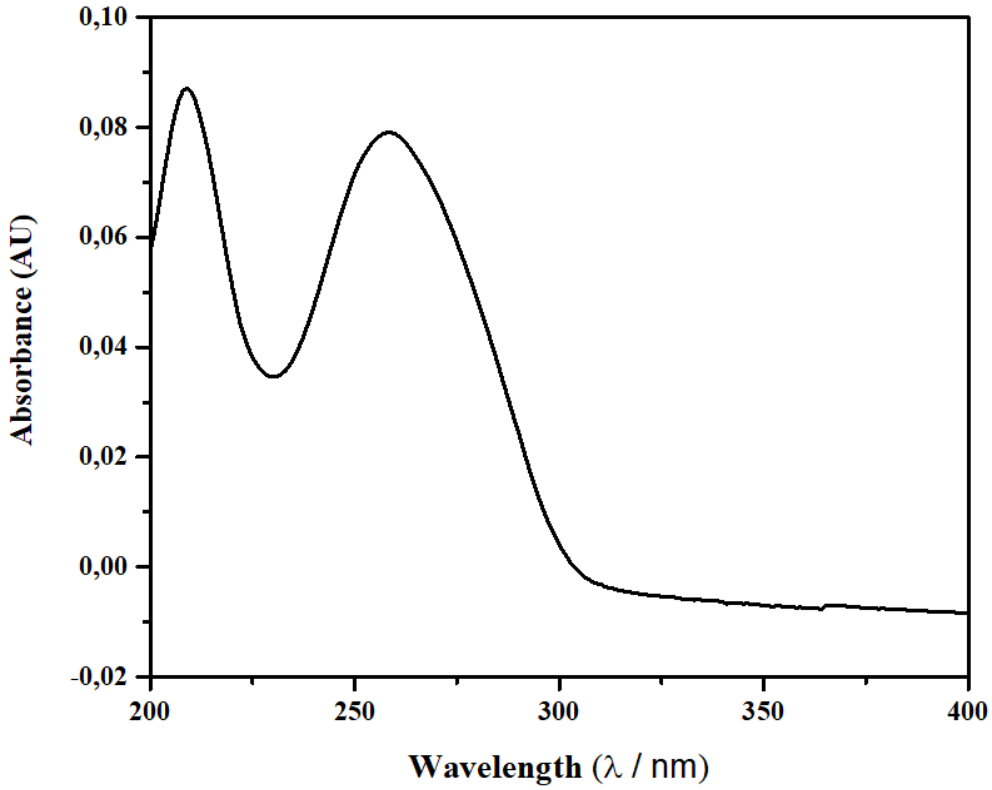

Appendix 19

RP-HPLC trace of crude dimeric diarylmercury-ON1 conjugate.

A BioZenTM oligo 00F-4790-E0-column (150 x 4.6 mm, 2.6 µm) was used in RP-HPLC, eluting with a linear gradient (10 to 60% over 40 min, flow rate 0.6 ml min^{-1}) of ACN in 50 mM aq triethylammonium acetate (pH= 7.0) and UV absorbance at λ = 260 nm.

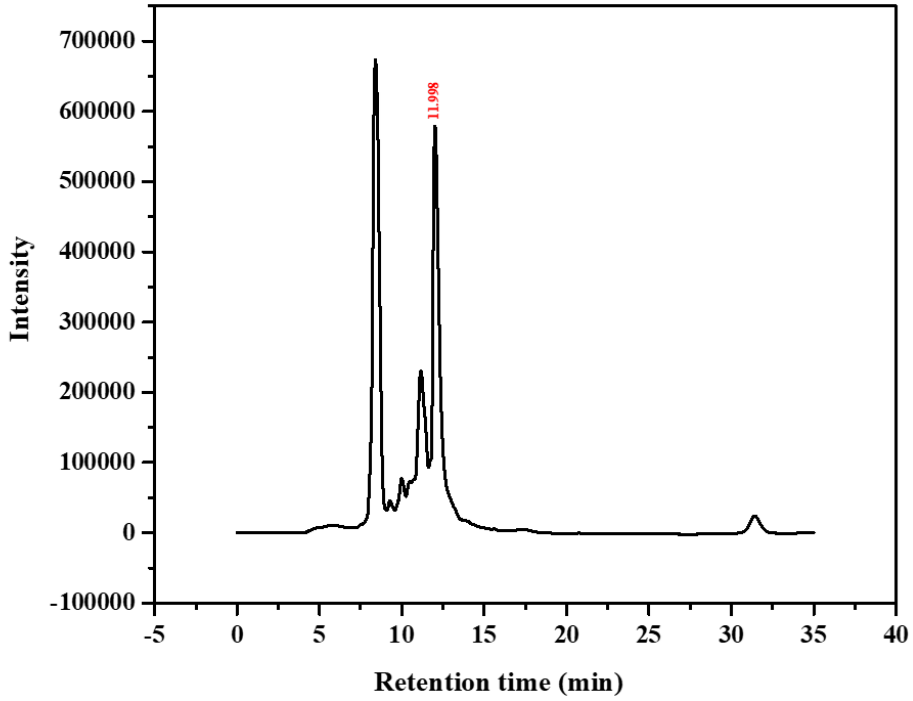

Appendix 20

RP-HPLC trace of crude dimeric diarylmercury-ON2 conjugate.

Same chromatographic condition as dimeric diarylmercury-ON1 was used.

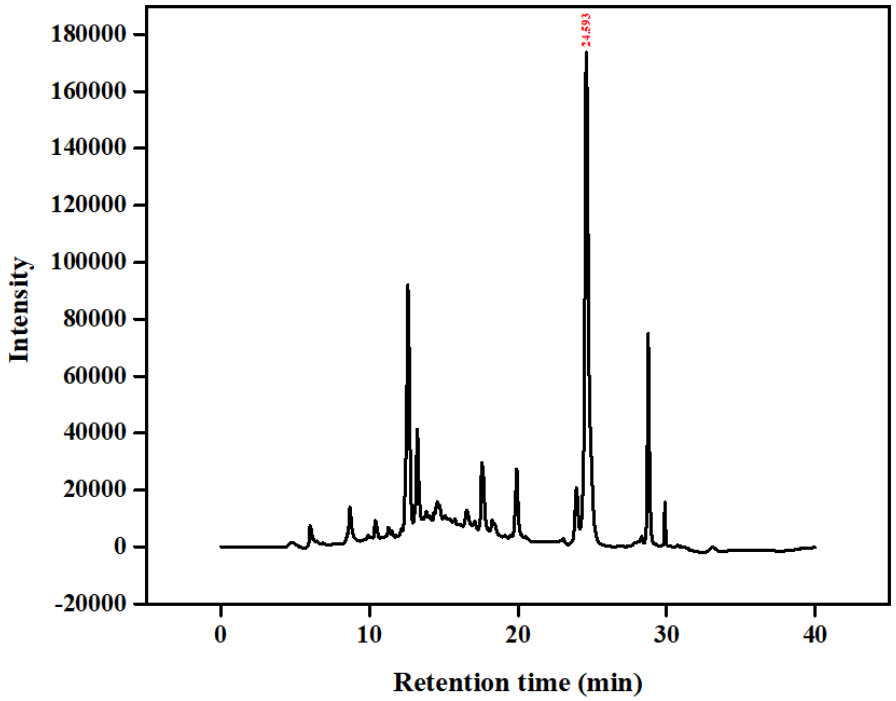

Appendix 21.1

UPLC-HRMS spectrum of the dimeric diarylmercury-ON1 conjugate

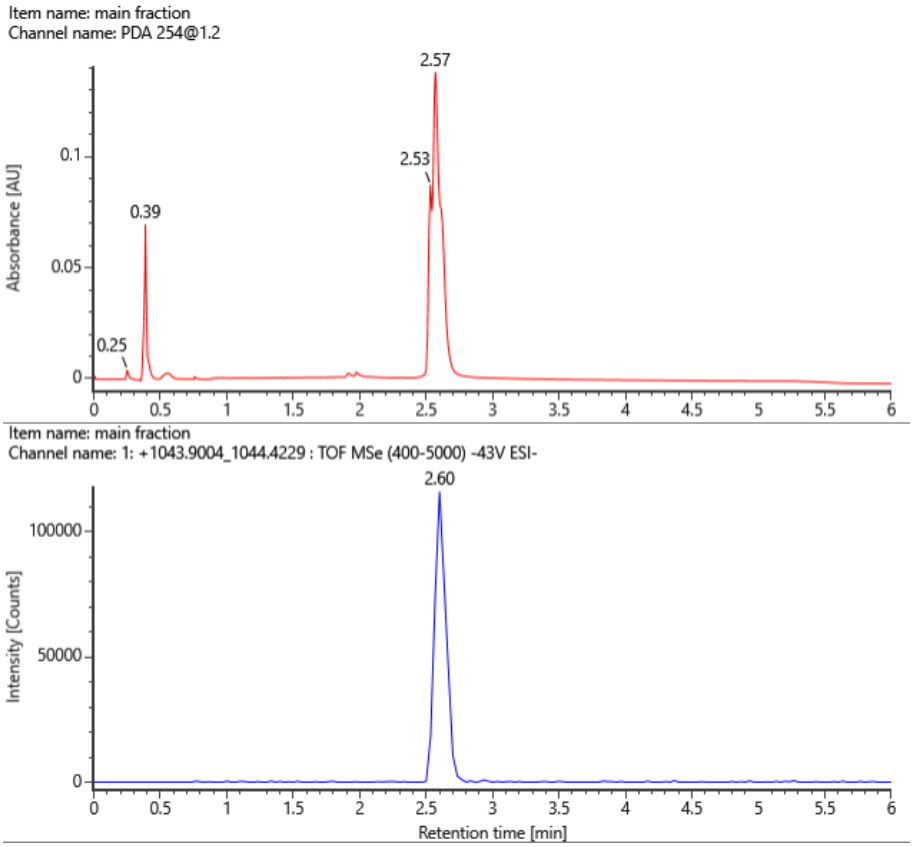

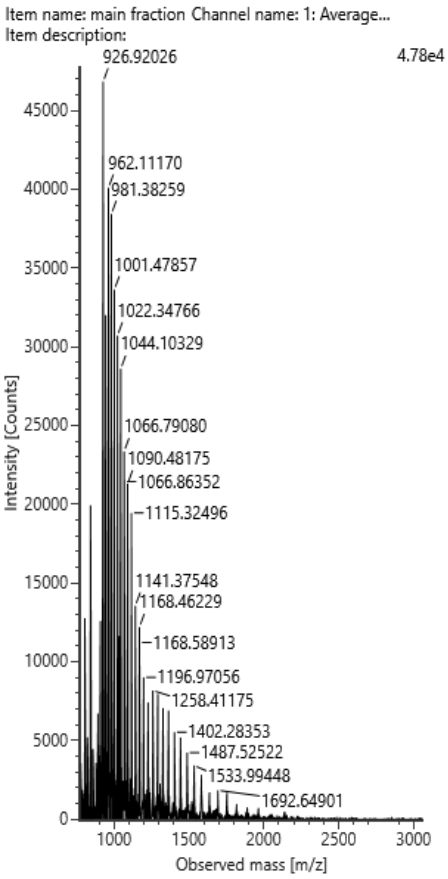

Appendix 21.2

UPLC-HRMS spectrum of the dimeric diarylmercury-ON1 conjugate after 49 h of incubation at rt.